UC Davis
UC Davis Electronic Theses and Dissertations

Title

Establishing Capacity Limit States for Nonductile Bridge Columns through Modeling and Simulation

Permalink

Author

Zhou, Jin

Publication Date

2021

Peer reviewed|Thesis/dissertation

Establishing Capacity Limit States for Nonductile Bridge Columns through
Modeling and Simulation

By

JIN ZHOU
DISSERTATION

Submitted in partial satisfaction of the requirement for the degree of

DOCTOR OF PHILOSOPHY

in

Civil and Environmental Engineering

in the

OFFICE OF GRADUATE STUDIES

of the

UNIVERSITY OF CALIFORNIA

DAVIS

Approved:

_____
Sashi K. Kunnath, Chair

_____
Amit Kanvinde

_____
John E. Bolander

Committee in charge

2021

Abstract

The ShakeCast software platform, utilized by the California Department of Transportation (Caltrans), utilizes near real-time ground shaking maps generated by the US Geological Survey in conjunction with predictive fragility models, encompassing both seismic demand models and component/system capacity models, to evaluate the likely damage to all bridges in the vicinity of an earthquake event. The ability to estimate with reasonable accuracy the likelihood and extent of damage to bridges following an earthquake is crucial to post-earthquake activities such as the mobilization of emergency response. While the development of seismic demand models has seen considerable progress, there is a significant gap in our current ability to correlate demands with capacity limit states, particularly for older California bridges. Whereas modern bridges designed after 1990 are expected to perform well, older bridges, particularly those built before 1971 (and referred to as Era-1 bridges in this dissertation), are vulnerable to damage. It is the goal of this research to address this gap by developing a range of component capacity limit states (CCLS), from minor damage up to collapse, for pre-1971 Caltrans bridge columns through rigorous modeling and comprehensive simulations.

A simulation model is developed for non-ductile bridge columns considering potential failure modes such as flexure, shear and mixed shear-flexure and incorporating critical effects at the material level (such as confinement in concrete, bar buckling in reinforcing steel) and sectional level (such as bond-slip due to strain penetration). Given the prevalence of drift-based measures in seismic design and assessment, the first choice considered in the development of the CCLS models was ductility. A strain-based approach was used to correlate damage with capacity limit states for both circular and wide rectangular sections that typify Era-1 bridge columns.

Findings from this phase of work exposed a major drawback in using ductility-based measures to characterize capacity limit states under random earthquake-induced loading. Hence, a major effort was dedicated to developing a damage-index based approach to classifying limit states. The proposed damage-based approach to developing CCLS models was validated against experimental data and then applied to single, two and three-column bents. Fragility functions were developed wherein exceedance probabilities of damage states are examined as a function of seismic intensity. The new damage-based methodology was successful in predicting a range of capacity limit states associated with visual damage such as cracking of the cover concrete, spalling of concrete, buckling of longitudinal reinforcement, crushing of the core concrete and multi-bar rupture. Findings from the study will not only assist in post-earthquake emergency response efforts but also in prioritizing strengthening of such nonductile bridges.

Acknowledgments

First, I would like to express my deepest thanks to my advisor, Professor Sashi K. Kunnath, whose expertise was invaluable in formulating the research questions and methodology. I am truly thankful for the trust he placed in me from the beginning of my academic life as an MS student at UC Davis and the constant guidance during the past six years.

I am grateful for all the support and advice from Professor John E. Bolander, chairing my qualifying examination committee and serving as a member of my dissertation committee. I would like to offer my thanks to Professor Amit Kanvinde for being on my dissertation committee and reviewing my work.

I also would like to convey my appreciation to the people I worked with these years: Zhelun Zhang, Li Shan, Han Yang, Laura Hernandez-Bassal, and Ahmed Al Jasar – thank you for all the help, and for making my work environment friendly and enjoyable. In particular, I am truly thankful to my friend Xingzhu Wu for his endless support.

Additionally, I would like to thank my parents, Jianjun and Bolin, my fiancé, Weisheng, and my cat, Fifi, for their unconditional love and support. The majority of this dissertation was completed during the COVID-19 pandemic. I have experienced anxiety and sadness in the process. How lucky I am to receive the tremendous love from each of you to reach my milestone.

Table of Contents

List of Figures

List of Tables

CHAPTER 1.0 INTRODUCTION

1.1   Background

The ShakeCast platform, developed by the United States Geological Survey (USGS) and utilized by the California Department of Transportation (Caltrans) since 2008, uses near real-time ground shaking maps generated by USGS in conjunction with predictive fragility models, encompassing both seismic demand models and component/system capacity models, to evaluate the likely damage to all bridges in the vicinity of an earthquake event. While the development of seismic demand models has seen considerable progress, there is a significant gap in our current ability to correlate demands with capacity limit states, particularly for older California bridges.

Internal work at Caltrans has focused on bridge-inventory characterization which involves the development of a new bridge taxonomy to group bridge classes/subclasses according to salient design features relevant to seismic performance. The process of assigning individual bridges to a class enables the assignment of fragility models in ShakeCast. Additionally, the capacity of various bridge-component details is being developed as a set of column capacity limit state (CCLS) models that characterize component damage as a function of earthquake demands. The development of the CCLS and next-generation fragility models, for most concrete bridge classes in California, is ongoing by a team of investigators at Georgia Institute of Technology and Rice University (the GT/R team), referred to henceforth as Project T1780.

Since there are no documented references that systematically captures community perspectives regarding optimal bridge CCLS models or the uncertainty associated with differing perspectives, Caltrans decided to engage the Pacific Earthquake Engineering Research (PEER) center to assist with organizing a workshop wherein a group of experts (with extensive research

experience on bridge column testing and seismic performance assessment) provide input and feedback on the GT/R team's effort to compile and interpret available column-test data from the research literature. In terms of downstream application, there is growing adoption of the ShakeCast platform as a primary means for implementing organization-specific earthquake-damage alerting and loss estimation strategies for both live emergency situations and for pre-event planning. Multiple state Departments of Transportation (DOTs) have already adopted ShakeCast and others have committed to a Transportation Pooled Fund project (http://www.pooledfund.org/Details/Solicitation/1406). Fragility models developed for state DOTs may vary due to differences in the composition of the local bridge inventory, thus affecting the seismic demand models for local classes. However, establishing a benchmark framework for characterizing uncertainty in CCLS models will serve each of these model-development efforts.

The GT/R project investigators have been compiling a database of experimental research findings to facilitate the development of limit state fragilities for performance-critical bridge components. The first phase of the CCLS model development was focused on bridge columns and a draft version of the statistically synthesized capacity models for bridge columns was presented at the workshop. Feedback from workshop participants highlighted many issues that need to be addressed in the CCLS development but a primary consensus was the need to establish a range of capacity limit states (from minor damage up to collapse) particularly for older Caltrans bridge columns so as to enable post-earthquake damage assessment as well as improve emergency response capabilities.

1.2   Previous work

Though there have been extensive studies on damage assessment of building and bridge components and systems, the concept of component limit states to classify bridge damage following an earthquake is more recent. A more extensive review of models and approaches to seismic performance in the context of damage prediction is presented in Chapter 4. In this section, the literature review is limited to the assessment of capacity limit states.

Code-based design is expected to implicitly guarantee Life Safety. However, it is often necessary to quantify lower limit states to assess damage and losses following an earthquake. Considering the state of strain in concrete and steel, Kowalsky (2000) defines two limit states, i.e. 'serviceability', while 'damage control' implies that only repairable damage occurs. The compression strain in concrete at the limit of 'serviceability' was defined as the strain at which crushing is expected to begin, while the same limit state considering tensile strain in the reinforcing steel was defined as the strain at which residual crack widths would exceed 1 mm (based on the work of Priestley et al. 1996), thus affecting serviceability and likely requiring repair. Next, extending earlier research by Priestley et al. (1996), Kowalsky developed dimensionless curvature relationships for these limit states. The resulting expressions are utilized to demonstrate the variations in drift, ductility, and equivalent viscous damping (a concept introduced by Jacobsen, 1930 and advanced by Gulkan and Sozen, 1974 and Shibata and Sozen, 1976) for columns with different aspect ratios.

Mackie and Stojadinovic (2005) develop a methodology using the Pacific Earthquake Engineering Research (PEER) center's performance-based earthquake engineering framework to assess probable highway bridge losses for critical decision making regarding the post-earthquake safety and repair of a highway network. Intensity measures were coupled with engineering

demand parameters to formulate probabilistic demand models to facilitate the development of bridge loss fragilities. They then consider a damage model at the component level (initiation of bar buckling) based on statistical analysis of experimental data and another damage model at the system level based on finite element reliability analysis to predict the loss of lateral and vertical load-carrying capacity. Finally, two loss models were formulated: component damage states that assess repair costs to return bridges to full functionality, and system level losses that consider bridge traffic capacity and collapse prevention.

Vosooghi and Saiidi (2012) analyzed measured data from 32 bridge column models, mostly tested on shake tables, to develop fragility curves for six seismic response parameters at six distinct damage states (DSs). The DSs were categorized as follows: flexural cracking - DS1, minor concrete cover spalling - DS2, extensive spalling of cover concrete - DS3, exposed bars - DS4, initiation of concrete core damage - DS5, and bar fracture - DS6. The six response parameters used in the study were: maximum drift ratio (MDR), residual drift ratio (RDR), frequency ratio (FR), inelasticity index (II), maximum longitudinal steel strain (MLS), and maximum transverse steel strain (MTS). The inelasticity index is conceptually similar to a damage index (DI). A methodology for probabilistic performance-based design (PPBD) and probabilistic performance-based assessment (PPBA) of reinforced concrete bridge columns were developed using the fragility curves. The probabilistic performance objective was defined as a Damage State under a specified earthquake intensity with a given probability of occurrence. Uncertainties associated with earthquake demands were not considered in this study.

Goodnight et. al. (2013, 2016) tested 30 circular, well- confined RC bridge piers under reversed cyclic loadings and realistic seismic load histories and found that the limit state of reinforcement bar buckling was influenced by load history, whereas the relationship between

strain and displacement along the envelope curve was not. The principal impact of load history on bar buckling was its influence on accumulated strains within the longitudinal reinforcement and transverse steel. The standard symmetric three-cycle per successive higher displacement level was shown to be more severe than the displacement history produced by real earthquakes when evaluated at the same peak displacement (Goodnight et. al., 2013). The measured data from the experiments was used to refine strain limit state recommendations. The serviceability limit states used in the experiments were: (1) analytical first yield force, (2) compressive strain at concrete crushing, (3) compressive strain at initial yielding of confinement steel, and (4) peak tensile strain preceding bar buckling. Experimental findings indicated that material strain could be used to as a good proxy to capture serviceability limit states. The author also pointed out that due to the high cost of large-scale experiments, numerical simulation can be an important tool for studying damage limit states in RC bridge piers (Goodnight et. al., 2016).

Like the AASHTO (2017) code in the US, seismic design provisions in the Canadian bridge code (CSA 2013) do not explicitly consider seismic demand versus seismic capacity of bridges at different damage states. Sheikh and Légeron (2013) proposed four different performance levels or limit states (LS) for bridges: LS1A (Fully Operational) where the response is essentially elastic; LS1B (Operational) wherein minor cracking that results from the earthquake has no consequence on serviceability and can be repaired with minor epoxy injection; LS2 (Delayed Operational) implies moderate damage but the bridge remains functional while repair work can progress; and LS3 (Stability) implies major structural damage requiring extensive repair (and bridge closure) or reconstruction. A methodology for nonlinear static pushover analysis of a typical bridge is presented which includes modeling of concrete and reinforcing steel to accurately represent the sectional response, followed by monitoring of

distinct damage/response states such as: initiation of inelastic deformation, onset of concrete

spalling, yielding of longitudinal reinforcement, buckling of main reinforcement, fracture of

transverse hoops, and crushing of core concrete. They introduce the concept of a damage

response factor (DRF) that is defined as the ratio of PGA between the LS under consideration

with the PGA at LS1B (since the response of the bridge is essentially elastic up to LS1B).

Discrete values for each LS is developed using the methodology for different bridge classes

(such as emergency route bridges and lifeline bridges) based on analysis of a typical 3-span

highway bridge.

A long-term effort at the University of Nevada, Reno summarized in Yoon et al. (2019)

describes a methodology, termed Probabilistic Damage Control Application (PDCA), to assess

the probable damage to a bridge column following an earthquake. The goal of the PDCA is to

quantify the exceedance probability of a target damage state when the bridge is subjected to a

seismic event. As pointed out by the authors, current Caltrans seismic design practice for

ordinary standard bridges is based simply on collapse prevention for an event with a 975-year

return period thereby limiting the ability of the designer to achieve a desired target performance

level. The engineering measure in PDCA is a damage index (DI) which quantifies damage as a

function of displacement demand, as follows:

$$DI = \frac{(\Delta_D - \Delta_y)}{(\Delta_{UC} - \Delta_y)} \qquad\qquad 1.1$$

In the above equation, Δ_D is the displacement demand due to the earthquake, Δ_y is the yield

displacement and Δ_{UC} is the ultimate displacement capacity as determined in laboratory testing.

Since the ultimate displacement relies on experimental data, the damage index has an empirical

component that introduces additional uncertainty into the process. Eventually, the paper also

introduces a total probability-based method to estimate the probability of exceeding a damage state within a bridge lifespan.

Among the tools used to develop capacity limit states is Incremental Dynamic Analysis (IDA) which was first proposed by Bertero (1980) and is now widely used in seismic collapse assessment of building structures. For example, Pang et.al. (2019) used IDA to compare the seismic performance of fiber-reinforced concrete (FRC) bridge columns reinforced with different fiber-reinforcement material. They developed 3-D nonlinear fiber-based finite element models to simulate the seismic behavior of different bridge columns, which were first calibrated with available experimental results. The seismic capacity of bridge columns was assessed using four flexural damage states: a) yielding of longitudinal reinforcement, b) crushing of the core concrete, c) bar buckling, and d) fracture of the longitudinal reinforcement. IDA curves were generated for both maximum and residual drift to eventually facilitate the development of seismic fragility curves for the different FRC columns.

1.3   Objectives of Study

The primary goal of the proposed effort is to enhance the capability of Caltrans to rapidly estimate damage to their bridge inventory following an earthquake to facilitate the planning, management, and mobilization of emergency response. Shakecast (used by Caltrans since 2008) uses near real-time ground shaking maps generated by USGS in conjunction with predictive seismic demand models and component/system capacity models to evaluate the likely damage to all bridges in the vicinity of the event. While the development of demand models has seen considerable progress, there is a significant gap in the ability of the Shakecast platform to correlate demands with capacity limit states, particularly for older California bridges. It is the

goal of this research to address this gap by developing a range of capacity limit states (from minor damage up to collapse) for pre-1990 Caltrans bridge columns through rigorous modeling and comprehensive simulations.

The focus of this study is on bridge columns because current design requirements limit inelastic behavior in the columns while ensuring that the girder-deck and foundation systems remain undamaged in an earthquake event. One of the challenges in developing CCLS models is selecting an appropriate response parameter or damage indicator. Drift or ductility based measures are simpler to conceive but are very difficult to calibrate against experimental data because most experiments are comprised of regular quasi-static tests at successively increasing magnitude whereas earthquake load impose fairly complex displacement histories on structural members. Hence, another important objective of the study is to investigate an alternative measure for damage prediction that is applicable to earthquake loading.

1.4   Scope of Work

The available experimental database of bridge column tests that are typical of pre-1971 Caltrans columns is limited and the cost of initiating new experimental projects to test large-scale non-ductile columns can be time-consuming and cost prohibitive. The abilities of modern open-source computational software such as OpenSees provide a unique and cost-effective opportunity to replace experimental testing with comprehensive numerical simulations. The following tasks are planned to achieve the goals of the project:

1) Development of a simulation model for non-ductile bridge columns and validation: Given the overarching objective of the research to develop capacity limit states through nonlinear modeling and simulation, it is imperative that the bridge column bents are

modeled as accurately as possible. This includes consideration of potential failure modes (flexure, shear and mixed flexure-shear), and incorporation of critical effects at the material level (such as confinement in concrete, bar buckling in reinforcing steel) and sectional level (such as bond-slip due to strain penetration). The model to be used in the simulations should be validated against experimentally observed responses.

2) Ductility-Based Calibration of Capacity Limit States: Given the prevalence of drift-based measures in seismic design and assessment, the first choice considered in the development of the CCLS models was ductility. First, damage limit states as a function of component ductility will be developed for a set of non-ductile columns directly from experimental data. Next, a strain-based approach will be used to calibrate the damage states and correlated with ductility. The new approach will be validated using a set of experimentally observed responses.

3) Application to Generic Era-1 Bridge Columns: Following the development of ductility-based CCLS models using experimental data, the strain-based approach developed in the previous task will be extend to a large set of hypothetical columns, considering both circular and wide rectangular sections, who cross-sectional properties are derived to represent typical Era-1 Caltrans columns. The loading protocol for the simulations will include both cyclic loading and earthquake time histories.

4) Development of Damage-Based Capacity Limit States: Findings from the previous task highlight the drawback of using ductility-based measures to characterize capacity limit states under random earthquake-induced loading histories. Hence, a major effort was dedicated to developing a damage-index based approach to classifying limit states. The proposed approach is validated with observed experimental responses and then applied to single-column bents subjected to both cyclic and earthquake loading.

5) Application to Single and Multi-Column Bents: In the final phase of the study, the proposed damage-based approach to developing CCLS models are applied to two and three-column bents. The objective of considering multi-column bents is to assess the benefits of redundancy in limiting the damage experienced by non-ductile bridge columns.

Relevant findings are summarized in the final chapter of this dissertation followed by recommendations for future work.

CHAPTER 2.0   BRIDGE COLUMN SIMULATION MODEL

The process of modeling a bridge structure is as important as the analysis methodology since the accuracy of the resulting numerical simulation depends largely on the simplifications and/or approximations introduced in the modeling process. The basic objective in modeling is not only to represent the structural configuration as reasonably as possible but also account for expected material and geometric nonlinearities. While 3D finite element analysis is acknowledged as the most sophisticated approach to nonlinear analysis of RC structures, the required computational effort can become prohibitive and it is not certain that a corresponding improvement in reliability of the analysis is guaranteed.

Bridge structures have been analyzed using coarse macromodels, concentrated plasticity models as well as more refined techniques involving distributed plasticity. The goal in macromodeling is to capture overall member behavior using "reduced" elements and "composite" action. The constitutive models in these idealizations are moment-rotation or moment-curvature relationships at locations of inelastic behavior and need to be specified a priori. A further refinement in member-by-member discretization that relies on material stress-strain relationships is the so-called fiber-section model where the beam-column element is still idealized as a line element but sectional behavior is monitored at selected integration points along the length assuming Bernoulli beam hypothesis. In the present study, bridge columns are modeled using fiber-sections and distributed plasticity as well as enhanced features to incorporate shear failure and bond-slip at the column-foundation interface. More importantly, fiber-based analysis can provide the magnitude of strain at locations within the concrete section as well in individual reinforcing bars, which is essential to develop damage states in the section.

11

One issue in the use of fiber-based models is the possibility of localization. This can result from two primary effects: the post-peak softening of concrete in compression and the post-peak response of steel following buckling in compression. As indicated in Kashani et al. (2016) the stress–strain behavior of reinforcing steel in a discretized fiber-section is averaged over the buckling length, hence, the element mesh size that influences the integration scheme must be carefully selected to account for localization at the critical section.

2.1   Element modeling

Three options were considered in modeling a bridge column element: (a) force-based beam-column element with four integration points (IPs); (b) force-based beam-column element with five integration points; (c) two force-based elements with one element corresponding to the potential plastic hinge length of the element – in this case, two integration points were used in the shorter segment and three integration points were used for the longer segment. The three schemes are illustrated in Fig. 2.1 (a). To assess the performance of each model, a static pushover analysis is carried out on a typical Caltrans bridge column with the following details: column height = 20 ft. (6.1 m), column diameter = 66 inch (1.68 m), longitudinal reinforcement ratio = 2.0% (44 # 11 bars), transverse reinforcement ratio = 0.8% (#8 @ 6"). The concrete strength was assumed to be 4,5 ksi (31 MPa) and the yield strength of both the longitudinal and transverse reinforcement was 69 ksi (4755 MPa).

The results of the pushover analysis for the various modeling choices are shown in **Figure 2.1**(b). Also included in the figure is a simulation of the same column using a non-local formulation proposed by Kenawy et. al. (2018). Since the goal of the study is to examine the behavior of bridge columns up to collapse, it is expected that the inelastic response will extend to

the post-peak softening range. The non-local approach by Kenawy and co-workers avoids localization, however, a version of the program for analysis of multi-column bents is not presently available. Hence, in the present study, the number of integration points in a single force-based element was selected based on the model that came closest to the non-local prediction. As is evident from **Figure 2.1**(b), a single force-based element with four integration points produced the best result.

Model 1: One force-based element with four integration points
Model 2: One force-based element with five integration points
Model 3: Two force-based elements with two and three integration points

(a)   (b)
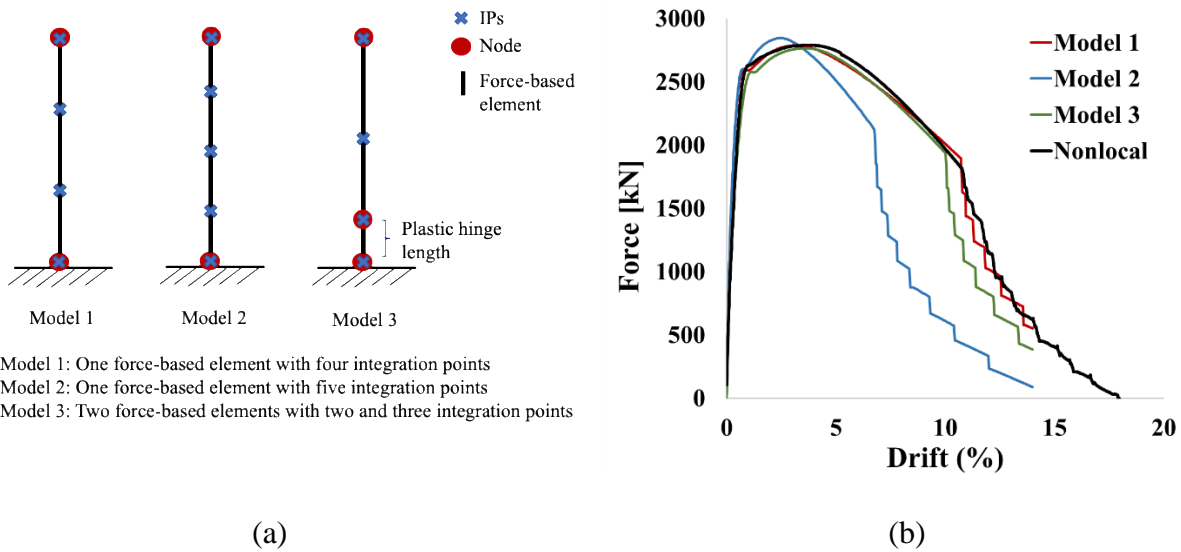
Figure 2.1 (a) Column modeling options (b) Pushover response

The simulation just described considered on flexural failure since the objective was to calibrate an appropriate element model for the bridge bents to be analyzed in the study. The complete column model to be used in the simulations of the different limit states includes a zero-length shear spring connected in series to the force-based beam column element and a zero-length section to account for bond-slip due primarily to strain penetration (as recommended in Feng et. al. 2014). Details of the constitutive stress–strain relationships of concrete and reinforcing steel, the displacement-based shear capacity model, and the strain penetration based bond-slip model are discussed in the following sections. The proposed modeling approach for

cyclic and seismic analysis of single and multi-column bents using the aforementioned

techniques are validated by comparing the numerically predicted responses to experimental

observations. The columns selected for the validation study cover both flexure and shear-flexure

failure modes and represent typical Era-1 Caltrans bridge columns.
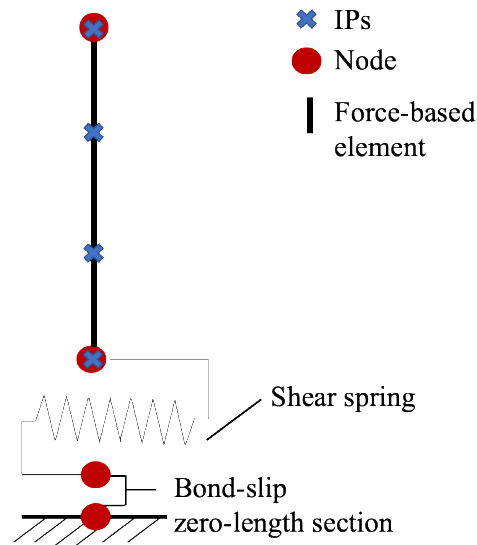
Figure 2.2 Column element model used in simulations

2.2 Material modeling

2.2.1 Concrete

Though numerous material models are available in OpenSees for simulating the cyclic

response of plain concrete, it was found that it was more important to accurately determine the

properties of confined concrete than use a sophisticated material model that captured the nuances

of cyclic response. As discussed herein, it was necessary to use different confinement models for

circular and rectangular sections. The material model in OpenSees used to define concrete fibers

is the "Concrete02" material which is based on the model developed by Yassin (1994) and

consists of a nonlinear curve in compression and linear elastic behavior in tension up to cracking followed by linear softening. The general monotonic and cyclic behavior of unconfined and confined concrete is shown in **Figure 2.3**.
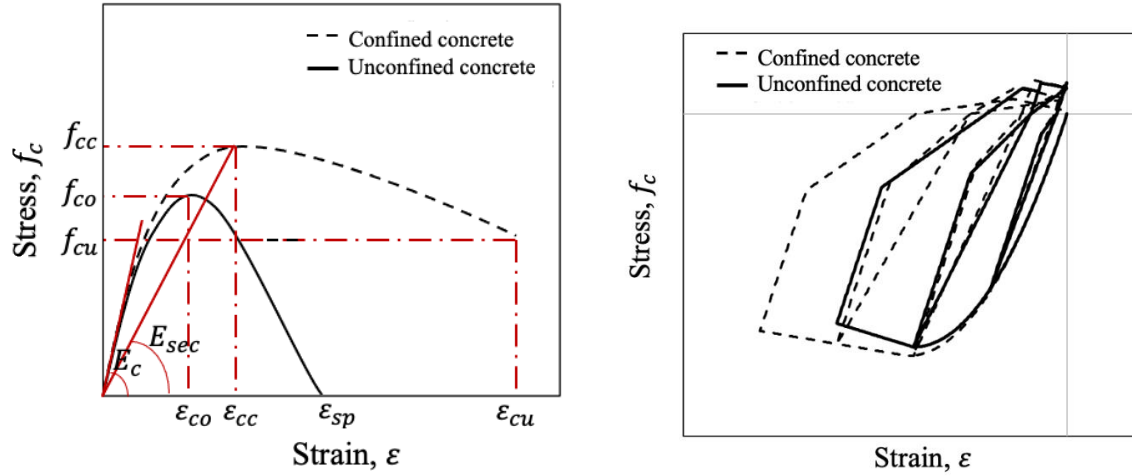
Figure 2.3 Monotonic and cyclic strain-stress relationship for concrete

Cover concrete is modeled using material properties based on cylinder tests of plain concrete whereas the confined core is modeled using properties derived from available models of confined concrete. The confinement model proposed by Mander et al. (1984) was used to determine the properties of the confined concrete for circular sections only. The stress-strain relationship for concrete was calculated using equations (2.1) – (2.10).

$$f_c = \frac{f_{cc}xr}{r - 1 + x^r} \qquad\qquad 2.1$$

$$x = \frac{\varepsilon_c}{\varepsilon_{cc}} \qquad\qquad 2.2$$

$$\varepsilon_{cc} = \varepsilon_{co}\left[1 + 5\left(\frac{f_{cc}}{f_{co}} - 1\right)\right] \qquad\qquad 2.3$$

$$r = \frac{E_c}{E_c - E_{\text{sec}}} \qquad\qquad 2.4$$

15

$$E_c = 5000\sqrt{f_{co}}, E_{sec} = {f_{cc}}/{\varepsilon_{cc}} \tag{2.5}$$

$$f_{cc} = f_{co}\left(-1.254 + 2.254\sqrt{\left(1 + \frac{7.94f_l'}{f_{co}}\right)} - 2\frac{f_l'}{f_{co}}\right) \tag{2.6}$$

$$f_l' = k_e f_l \tag{2.7}$$

$$f_l = \frac{1}{2}\rho_s f_{yh} \tag{2.8}$$

$$k_e = \begin{cases} \dfrac{\left(1 - \dfrac{s'}{2d_s}\right)^2}{1 - \rho_{cc}} & for \quad circular\ hoops \\[3mm] \dfrac{1 - \dfrac{s'}{2d_s}}{1 - \rho_{cc}} & for \quad circular\ spirals \\[3mm] \dfrac{\left(1 - \sum_{i=1}^{n}\dfrac{(w_i')^2}{6b_c d_c}\right)\left(1 - \dfrac{s'}{2b_c}\right)\left(1 - \dfrac{s'}{2d_c}\right)}{(1 - \rho_{cc})} & for \quad rectangular\ hoops \end{cases} \tag{2.9}$$

$$\varepsilon_{cu} = \varepsilon_{sp} + 1.4\rho_s \frac{f_{yh}}{f_{cc}}\varepsilon_{sm} \tag{2.10}$$

In the above expressions, f_{cc} = confined concrete peak compressive strength (MPa),

f_{co} =unconfined concrete compressive strength (MPa), ρ_{cc} = ratio of area of longitudinal

reinforcement to area of core of section, ρ_s = transverse reinforcement volumetric ratio,

f_{yh} =transverse reinforcement yield strength (MPa), ε_{cc} =confined concrete strain at peak

compressive strain, f_{cu} = confined concrete ultimate compressive strength (MPa), s' = clear

spacing between spiral or hoop bars (mm), d_s = diameter of spiral between bar centers (mm),

b_c , d_c = concrete core dimension (in mm) to center line of perimeter hoop in two directions, see

Figure 2.4, $w_i' = i_{th}$ clear transverse spacing (in mm) between adjacent longitudinal bars, as

shown in **Figure 2.4**, ε_{cu} = ultimate concrete compressive strain, ε_{sm} = strain at ultimate stress

of longitudinal steel

16
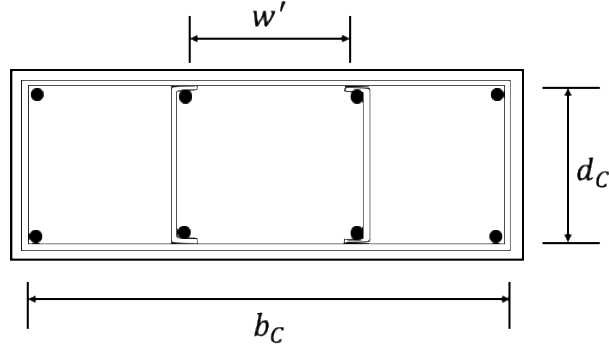
Figure 2.4 Definition of w_i', b_c and d_c

The Mander model was found to overestimate the ultimate strain for rectangular sections, hence, the confinement model proposed by Saatcioglu and Razvi (1992) was used for bridge bents with rectangular columns. The following equations were used to generate the stress-strain curve, and the model parameters are illustrated in **Figure 2.5**.

$$f_{cc} = f_{co} + k_1 f_{le} \tag{2.11}$$

$$k_1 = 6.7(f_{le})^{-0.17} \tag{2.12}$$

$$f_{le} = \frac{f_{lex} b_c + f_{ley} d_c}{b_c + d_c} \tag{2.13}$$

$$f_{lex} = k_e \rho_x f_{yh}, \ f_{ley} = k_e \rho_y f_{yh} \tag{2.14}$$

$$\rho_x = \frac{A_{sx}}{s' d_c}, \rho_y = \frac{A_{sy}}{s' b_c} \tag{2.15}$$

$$\varepsilon_{cc} = \varepsilon_{co} \left(1 + \frac{5 k_1 f_{le}}{f_{co}} \right) \tag{2.16}$$

$$\varepsilon_{85} = 260 \rho \varepsilon_{cc} + \varepsilon_{o85} \tag{2.17}$$
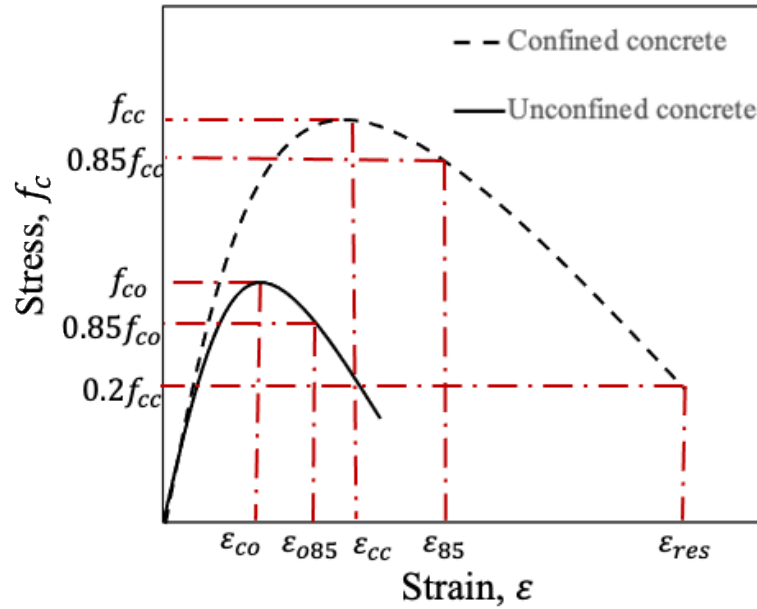
Figure 2.5 Strain-stress relationship of concrete for rectangular sections

Notations for the symbols appearing in the above equations are as follows: f_{cc} = peak confined concrete compressive strength (MPa), f_{co} =unconfined concrete compressive strength (MPa), ρ_x, ρ_y = transverse reinforcement volumetric ratio in x or y direction, f_{yh} = transverse reinforcement yield strength (MPa), ε_{cc} =confined concrete strain at peak compressive strain, ε_{co} =unconfined concrete strain at peak compressive strain, ε_{o85} = the strain at 85% strength level beyond the peak stress of unconfined concrete, where a value of 0.0038 may be appropriate under low rate of loading (Saatcioglu and Razvi, 1992), s' = clear spacing (in mm) between spiral or hoop bars, b_c , d_c = concrete core dimensions (in mm) to center line of perimeter hoop in two directions, see **Figure 2.4**, w_i' = i_{th} clear transverse spacing (in mm) between adjacent longitudinal bars, as shown in **Figure 2.4**.

2.2.2　Reinforcing steel

Several options are possible for modeling the inelastic behavior of steel reinforcement. In their study to simulate the response of bridge columns up to collapse, Kashani et al. (2016) investigated different uniaxial material models for reinforcing steel and proposed a new model that considers both inelastic buckling and low-cycle fatigue fracture of the reinforcing bar. They conclude that the buckling length of vertical reinforcement has a significant influence on the pinching response of RC columns and also reduces the low-cycle fatigue life of buckled bars. In this study, the "Steel02" and "ReinforcingSteel" models were first investigated and found to either not reproduce post-peak degrading behavior of the column or fail to converge at large deformations. Eventually, the "Hysteretic" material in OpenSees is used to model the behavior of reinforcing steel so that softening behavior can be specified beyond the ultimate stress since the post-peak response of structural components has been shown to significantly affect the predicted collapse capacity of structures. The "Hysteretic" material in OpenSees uses three control points on both the compression and tension side to represent the stress-strain response of the reinforcing steel bars. The multi-linear strain-stress response in tension of steel is shown in **Figure 2.6**. Equations 2.18 - 2.23 listed below provide the complete monotonic strain-stress relations for the reinforcing steel bars in tension:
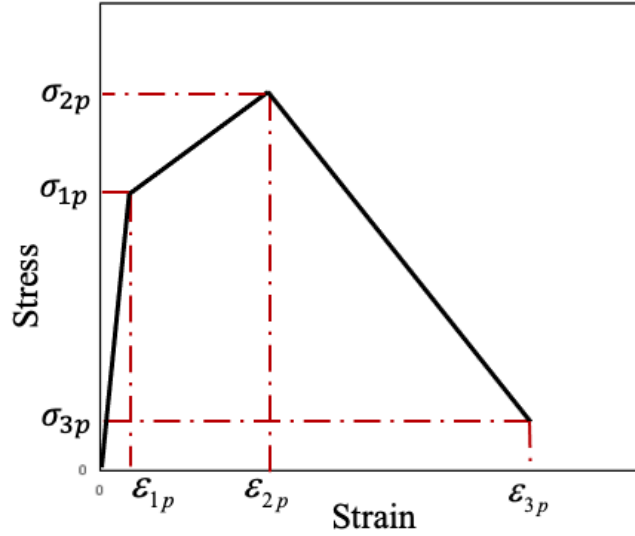
Figure 2.6 Strain-stress response of reinforcing bars in tension

$$\sigma_{1p} = f_y \tag{2.18}$$

$$\sigma_{2p} = 1.4f_y \tag{2.19}$$

$$\sigma_{3p} = 0.1f_y \tag{2.20}$$

$$\varepsilon_{1p} = \varepsilon_y = {f_y}/{E_s} \tag{2.21}$$

$$\varepsilon_{2p} = 20\varepsilon_y \tag{2.22}$$

$$\varepsilon_{3p} = 50\varepsilon_y \tag{2.23}$$

where f_y is the yield strength of the longitudinal reinforcement and E_s is the Young's Modulus.

To capture the effects of bar buckling in compression, the model developed by Zong et. al. (2014) is used. The model is derived by assuming the longitudinal bars and transverse reinforcement in a column to behave as a bar with springs (simulating the resistance by the confining bars) and is able to predict the post-yield softening response due to buckling. The overall compression response of a longitudinal bar is shown in **Figure 2.7**.
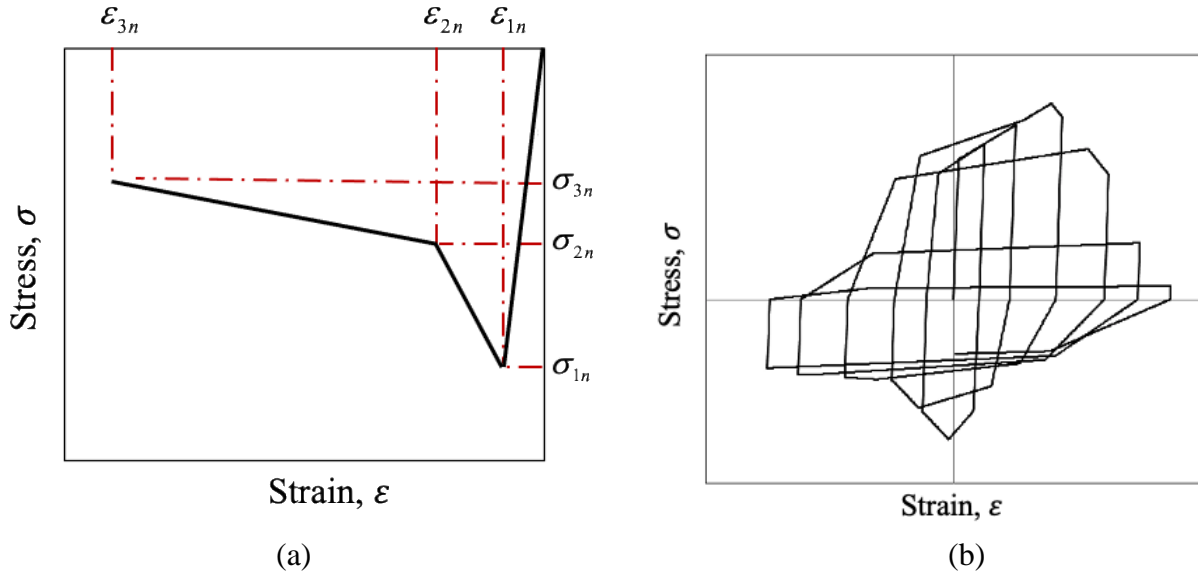
Figure 2.7 (a) Strain-stress curve of bar in compression; (b) Cyclic response

The three points to be defined in the "Hysteretic" material model is summarized in Equations 2.24 – 2.32. The first point is similar to the yield point in tension:

$$\sigma_{1n} = -f_y \qquad\qquad 2.24$$

$$\varepsilon_{1n} = -\varepsilon_y = -{f_y}/{E_s} \qquad\qquad 2.25$$

To determine the second point, a stiffness reduction coefficient C_s which varies as a function of the relative stiffness K/K_0 (where K is the effective stiffness of the spring and K_0 is a critical stiffness value of the spring that defines a limit for the minimum buckling length) and a normalized material strength parameter $\sqrt{f_y/420}\, s/d_b$ is established using the following expressions:

$$\sigma_{2n} = C_s\big((L_1 + 1)(\alpha/100) - 1\big) * f_y \qquad\qquad 2.26$$

$$\varepsilon_{2n} = C_s L_1 * \varepsilon_y \qquad\qquad 2.27$$

$$L_1 = -800 \left(\sqrt{f_y/420}\, s/d_b \right)^{-2.5} - 2.5 \tag{2.28}$$

$$\alpha = 3.0 - 0.2 \left(\sqrt{f_y/420}\, s/d_b \right)^2 \tag{2.29}$$

$$C_s = \begin{cases} (1 - (1 - K/K_0)^2)^{1/\beta} & 0 < K/K_0 < 1 \\ 1.0 & K/K_0 \geq 1 \end{cases}, \tag{2.30}$$

$$\beta = 4.5 - 0.25 \sqrt{f_y/420}\, s/d_b$$

$$K_0 = 0.02\pi^4 E I_b s^3 \tag{2.31}$$

K represents equivalent stiffness of the spring and can be estimated using:

$$K = \frac{F_y}{\Delta_y} \tag{2.32}$$

In the above equation, Δ_y can be solved iteratively using Equation 2.33 corresponding to the yield point of the material.

$$\frac{R(\tan\theta - \theta)}{\pi R} = \varepsilon_y \quad where \quad \theta = \arccos\left(R/(R + \Delta)\right) \tag{2.33}$$

$$F_y = 2\left(\frac{R(\tan\theta - \theta)}{\pi R}\right) E A_h \sin\left(\arccos\left(\frac{R}{R + \Delta_y}\right)\right) \tag{2.34}$$

Finally, the end point is obtained using the equations below:

$$\sigma_{3n} = 0.8\sigma_{2n} \tag{2.35}$$

$$\varepsilon_{3n} = (\min(C_s L_1 - 40, 1.5 C_s L_1) + C_s L_1)\varepsilon_y \tag{2.36}$$

Where f_y = yield strength of the longitudinal reinforcement, E = initial stiffness of the longitudinal bar, d_b = diameter (in mm) of the longitudinal reinforcement, I_b = moment of inertia of longitudinal bar section, R = radius of column core (mm), A_h = area of transverse bar section, s = center to center spacing (in mm) between transverse reinforcement. Complete

details are provided in Zong et al. (2014). Since the model was developed for bars that experience buckling due to inadequate confinement, it is less applicable for highly confined columns where buckling is restrained until core crushing occurs.

2.2.3   Bond-slip due to strain penetration

In order to construct a uniaxial material object for capturing strain penetration effects at the column-foundation interface of a bridge bent, a zero-length section element is introduced at the base of the bridge columns. The "Bond-SP01" material (Zhao and Sritharan 2007) in OpenSees is used to construct the zero-length section to represent strain penetration effects while the unmodified properties of concrete are used in this zero-length section. The bar stress versus slip response using the material Bond_SP01 is shown in **Figure 2.8**. The expressions to estimate the slip parameters are based on the recommendation in Zhao and Sritharan (2007) and are listed in Equations 2.37 - 2.38. An initial hardening ratio in the range $b = 0.3 - 0.5$ is suggested, hence a value of 0.4 is used in this study.
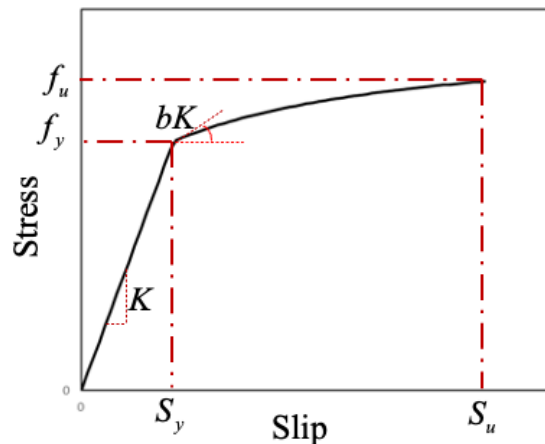
Figure 2.8 Bar stress vs. slip response

$$S_y = 2.54 \left(\frac{d_b}{8437} \frac{f_y}{\sqrt{f_{co}}} (2\alpha + 1) \right)^{(1/\alpha)} + 0.34 \qquad\qquad 2.37$$

$$S_u = 35 S_y \qquad\qquad 2.38$$

Here, S_y = rebar slip (in mm) at member interface at yield stress, f_{co} = unconfined concrete compressive strength (MPa), f_y = yield strength (MPa) of the longitudinal reinforcement, d_b = diameter of longitudinal reinforcement(mm), α = parameter used in the local bond-slip relation and was set to 0.4 as recommended by the authors of the model.

2.3 Shear modeling

One approach to consider shear deformations in OpenSees is to use the "Shear Aggregator" option that groups previous defined section objects (such as the fiber section that is used to model flexural behavior). This does not consider shear-flexure interaction in the nonlinear range but can capture shear failure if it occurs before flexural failure. In the case that flexural yielding occurs prior to shear failure, it is necessary to consider an alternative approach. Elwood and Moehle (2003) proposed a shear spring in conjunction with a shear limit curve. Whereas elastic shear deformations are included in the initial phase of the response, inelastic shear behavior is triggered when the shear demand exceeds the shear capacity limit curve. The idealized shear trigger response in OpenSees is shown conceptually in **Figure 2.9**. The deterioration of the force-deformation response is based on an empirical drift capacity model. The command "limitCurve Shear" in OpenSees is used to construct a shear limit curve object. A shear spring element was incorporated in the model to represent shear deformations as well as simulate potential shear-failure of the RC bridge pier. This spring element will be used to model bridge columns that experienced both flexure-shear failure and pure shear failure.
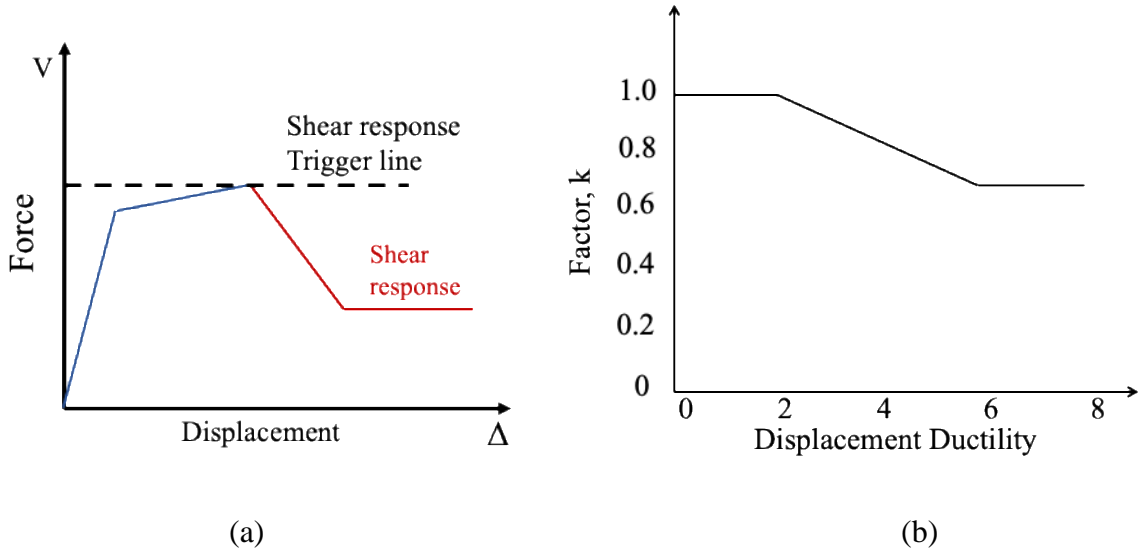
Figure 2.9 (a) Shear spring trigger line; (b) Modification factor

Sezen's shear capacity model is chosen to calculate the column shear capacity in this study due to its relatively high accuracy and easy implementation.

$$V = k(V_c + V_s) \tag{2.39}$$

$$V_c = 0.8A_g \left(\frac{0.5\sqrt{f_c'}}{a/d} \sqrt{1 + \frac{P}{0.5\sqrt{f_c'}A_g}} \right) \tag{2.40}$$

$$V_s = \frac{A_v f_y d}{s} \tag{2.41}$$

Where $f_c' =$ confined concrete peak compressive strength (Mpa), $f_y =$ longitudinal reinforcement yield strength, $a/d =$ aspect ratio, $A_v =$ transverse reinforcement area, $A_g =$ gross area of the section, $P =$ axial load, $s =$ transverse reinforcement spacing, $d =$ distance from the extreme compression fiber to centroid of tension reinforcement (section depth). In Eq. 2.39, k is a ductility-based factor as shown in Figure 2.9 – which is defined to be equal to 1.0 for displacement ductility less than 2 and set to 0.7 for ductility equal to or exceeding 6.0. At intermediate ductilities, the k factor is obtained by linear interpolation.

2.4 Validation of proposed modeling scheme

To validate the reliability of modeling methodology proposed in the previous sections, comparisons of observed experimental and numerically simulated response of selected columns from the literature were made. In all, four columns were considered in the validation study: two columns represent typical Era-1 Caltrans circular columns and are taken from the research carried out by Chai et al. (1991) and Ranf et al. (2006); the third column (tested by Soesianawati et. al. 1986) represents a typical rectangular column; and the final simulation represents an Era-1 column (Sun et al. 1993) that exhibits a mixed (flexure-shear) failure.

2.4.1 Circular columns failing in flexure

The cross-sectional details as well as material properties of concrete and reinforcing steel of the two Era-1 circular columns (Chai et. al. 1991; Ranf et al. 2006) are shown in Table 2.1.

Table 2.1 Circular columns considered in validation study

(a) Cross-section and reinforcement details

Property	Chai et. al. (1991)	Ranf et. al. (2006)
Diameter (cm)	61	51
Height (cm)	366	152
Cover (cm)	2	1.5
Diameter of trans. bar (mm)	6.4	4.6
Spacing (cm)	13	10
Trans. Steel ratio	0.17%	0.15%
Long. Reinforcement (mm)	26 Ø 19	10 Ø 16
Long. steel ratio	2.5%	1.0%

(b) Material properties

		Specimen	
		Chai et al.	*Ranf et al.*
Concrete properties	f_{cc} (MPa)	-33.2	-37.5
	ε_{cc}	-0.0025	-0.0026
	f_{cu} (Mpa)	-3.3	-3.8
	ε_{cu}	-0.026	-0.023
Steel properties	σ_{1p} (MPa)	314.8	455
	ε_{1p}	0.0016	0.0023
	σ_{2p} (MPa)	441	637
	ε_{2p}	0.0315	0.0455
	σ_{3p} (MPa)	31.5	45.5
	ε_{3p}	0.079	0.114
	σ_{1n} (MPa)	-314.8	-455
	ε_{1n}	-0.0016	-0.0023
	σ_{2n} (MPa)	-182	-192
	ε_{2n}	-0.0197	-0.0219
	σ_{3n} (MPa)	-146	-154
	ε_{3n}	-0.1024	-0.1349

As outlined in Chapter 2.2, parameters for the confined concrete were estimated using the model proposed by Mander whereas the properties of the reinforcing steel were specified to fit the parameters of the uniaxial Hysteretic material model in OpenSees. The main parameter controlling the cyclic response of concrete is the unloading stiffness in compression – in Concrete02 this is specified as the ratio of the unloading to the initial stiffness and was set to 0.1. The cyclic response of steel is defined by two parameters to control strength degradation and an additional two parameters to control pinching behavior. These four parameters were calibrated to

match the overall observed response of the columns considered in the validation study. The factor to control pinching along the deformation (or strain) axis (referred to as PinchX in OpenSees) was set to 0.8 and the factor to control pinching along the force (or stress) axis (referred to as PinchY in OpenSees) was set to 0.2. The factors to control degradation due to ductility and energy were assigned values of 0.01 and 0.02, respectively.

The results of the numerical simulations are compared with the experimental responses in **Figure 2.10**. The overall response is reasonably predicted in both cases. For the column tested by Chai et al., the peak lateral force in the experiment was approximately 237 kN whereas the numerical prediction is slightly higher (at 255 kN). Notable degradation in the response is seen after the deformation exceeds 110 mm in both the experiment and the simulation. In the case of the column tested by Ranf et. al. the experimentally recorded peak force is 214 kN while the numerical simulation slightly under-predicts this peak value as 196 kN. In general, the shape of the hysteretic loops, the unloading and reloading stiffness and the strength deterioration are captured quite effectively.
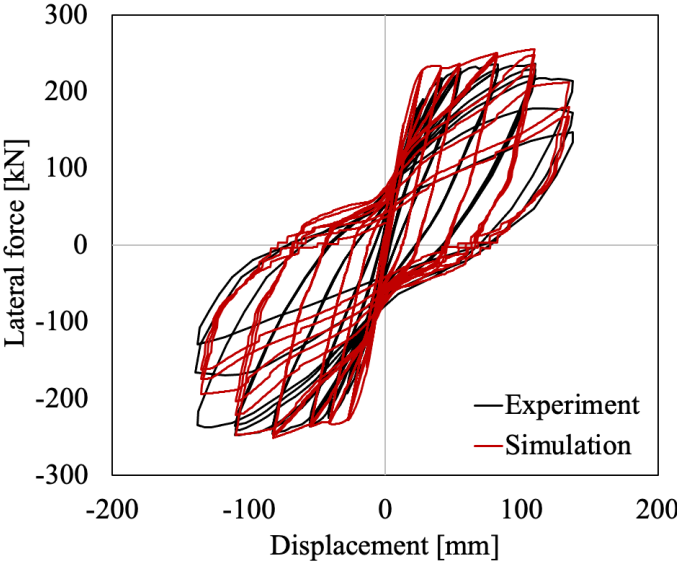
(a)
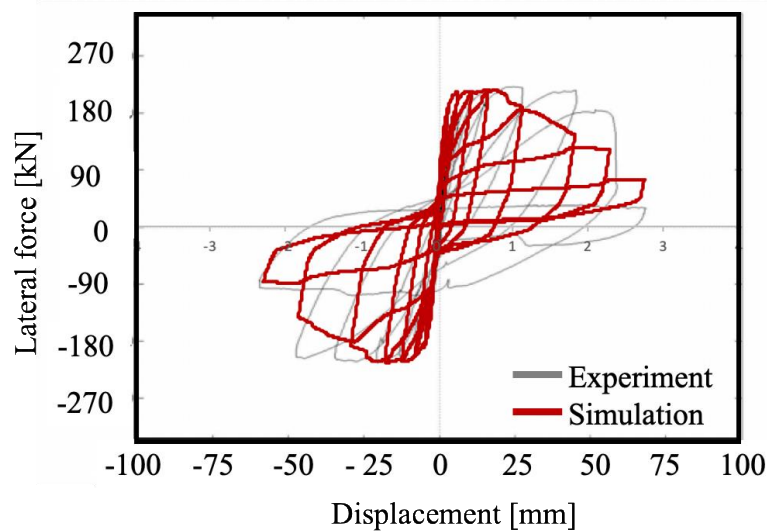
(b)

Figure 2.10 Comparison between simulated and experimental response of selected columns: (a) Chai et al. (1991) (b) Ranf et al. (2006)

2.4.2   Square column failing in flexure

A square column denoted as "Unit 1" from Soesianawati et. al. (1986) is selected to validate the reliability of the modeling approach for a non-circular column. While the goal of the selection was to find a non-ductile column with a larger depth-to-width ratio, this column was the closest to an Era-1 rectangular column in terms of reinforcement detailing. Details of the column cross-section and the material properties of concrete and reinforcing steel are presented in **Table 2.2**. The cyclic degrading parameters used in this simulation is identical to those used for the circular columns. The results of the simulation using OpenSees is compared with the experimentally observed behavior in **Figure 2.11.** The predicted maximum lateral resistance is about 3% lower than the experimental value. Overall, the cyclic response and cyclic degradation is simulated reasonably.

Table 2.2 Details of tested column (Soesianawati et. al. 1986)

(a) Cross-section information

H (cm)	40
D (cm)	40
Height (cm)	160
Trans. bar dia. (mm)	6.4
Spacing (cm)	8.5
Trans. steel ratio	0.41%
Long. reinforcement	12 Ø 16 mm
Long. Steel Ratio	1.51%

(b) Material properties

Concrete properties	f_{cc} (MPa)	-52.7	f_{cu}(Mpa)	-5.27
	ε_{cc}	-0.0033	ε_{cu}	-0.30
Steel properties	σ_{1p} (MPa)	445.8	σ_{1n}(MPa)	-445.8
	ε_{1p}	0.0023	ε_{1n}	-0.0023
	σ_{2p}(MPa)	624.2	σ_{2n}(MPa)	-273.5
	ε_{2p}	0.0455	ε_{2n}	-0.031
	σ_{3p}(MPa)	44.6	σ_{3n}(MPa)	-218
	ε_{3p}	0.115	ε_{3n}	-0.1513

Figure 2.11 Numerically simulated versus experimental response (Soesianawati et. al. 1986)

2.4.3   Column exhibiting mixed failure mode

Sun et al (1993) tested several rectangular bridge columns with inadequate transverse reinforcement. Among the tested columns, Specimen R5 exhibited a mixed failure model and was chosen as part of the validation study. The cross-sectional details of the column is displayed in **Figure 2.12** and the material parameters used in the simulation are presented in **Table 2.3**.
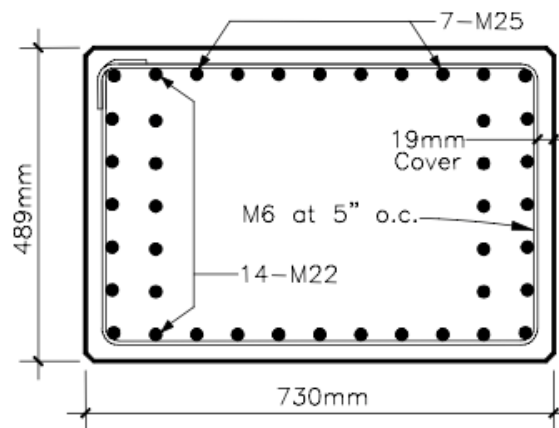
Figure 2.12 Reinforcement details of specimen R5 (Sun et al. 1993)

Table 2.3 Column material properties

Concrete properties	f_{cc} (MPa)	-36	f_{cu} (Mpa)	-3.6
	ε_{cc}	-0.0026	ε_{cu}	-0.047
Steel properties	σ_{1p} (MPa)	317	σ_{1n} (MPa)	-317
	ε_{1p}	0.0016	ε_{1n}	-0.0016
	σ_{2p} (MPa)	443	σ_{2n} (MPa)	-218.7
	ε_{2p}	0.032	ε_{2n}	-0.0271
	σ_{3p} (MPa)	31.7	σ_{3n} (MPa)	-175
	ε_{3p}	0.08	ε_{3n}	-0.1176

The column response was simulated using the "limiting shear curve" and the column shear capacity was estimated using the model discussed in Section 2.3. All other cyclic and degrading parameters were identical to those used in the previous three simulations. The comparison between the experimental and simulated results is shown in **Figure 2.13**. The peak lateral force in the test was 580 kN and the simulated value is 591 kN, a difference of less than 2%. The shear degradation was initiated at a displacement of approximately 60 mm (corresponding to a ductility of 2.0). As evident from the figure, the overall cyclic response and degradation compares well with the experiment.
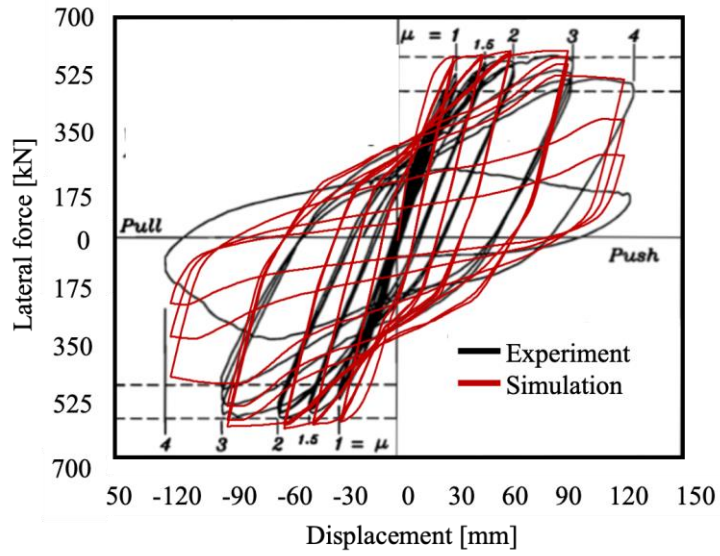
Figure 2.13 Comparison between simulated and experimental response of column with mixed flexure-shear failure (Sun et al., 1993)

CHAPTER 3.0   DUCTILITY-BASED CAPACITY LIMIT STATES FOR NON-DUCTILE BRIDGE COLUMNS

3.1   Background: Caltrans-PEER Center Workshop

As mentioned in the introduction of this dissertation, an ongoing effort at Georgia Tech and Rice University has examined nearly 200 columns that have been tested in laboratories in the US and New Zealand and classified them into three eras and three potential failure modes (flexure, shear and mixed modes). The eras represent pre-ductile (< 1971), early ductile (1971 – 1991) and modern ductile (>1991) columns. Part of the problem with the database is that many of the columns are not typical of Caltrans bridge column configurations and a significant number of them are building columns, some with high axial load ratios. Nevertheless, a set of CCLS models were developed from the data using ductility as the primary demand measure.

The Caltrans-PEER workshop, also discussed in the introduction, was held October 26-27, 2017. The focus of the workshop was on the synthesis of expert opinions to characterize the uncertainty in the full distribution of Engineering Demand Parameter (EDP) values (e.g., 10th , 50th and 90th percentile) which may be assigned to CCLS models. Using experimental data compiled by researchers at the Georgia Institute of Technology, Caltrans developed a preliminary set of CCLS models for bridge columns which was provided to the panelists as reference material for the survey. The workshop discussion focused on issues related to quantifying CCLS uncertainty for a range of component designs (e.g., brittle, strength-degrading, and ductile columns having both regular and wide sections) over a range of damage states. Additional factors (e.g., scale and shape effects) which may influence CCLS-value selections were also discussed. The workshop provided significant input into the refinement of the draft

CCLS models developed by Caltrans. It also provided an opportunity to extend the findings (based on limited experimental data) by investigating the response of a broader subset of column configurations through modeling and simulation.

3.2   Direct Ductility-Based Calibration of Capacity Limit States

Two sets of column configurations were considered in this phase of the study: the first set was comprised of data from cyclic tests of columns that could be classified as Era-1 Caltrans columns, and the second set comprised hypothetically constructed single-column bent configurations that met the basic section criteria for Era-1 columns. While ductility values are readily available for a range of limit states in the reported experimental results, each researcher used a slightly different definition of the yield displacement. The development of the CCLS models required a uniform definition of the yield displacement so that the limit states were calibrated consistently across the database of experimental observations.

3.2.1   Defining component ductility

An important decision that was made in the development of the CCLS models by the GT/R team was the choice of displacement ductility as the demand measure on which the damage limit states were classified. This decision was predicated on the fact that force-displacement data was available for all tests in the database whereas curvature data was not available in many of the reported tests. Converting displacement ductility into curvature ductility would require an assumption of the plastic hinge length – a quantity that was not readily discernable from the reported experimental observations. The choice of displacement ductility as the primary Engineering Demand Parameter (EDP) required a definition of the yield displacement. After

reviewing numerous approaches to establish the yield point on the force-displacement curves, the methodology proposed by researchers in New Zealand (Park 1989) was selected. Consequently, all the experimental data were uniformly processed to generate displacement ductility values based on the definition shown schematically in **Figure 3.1**.
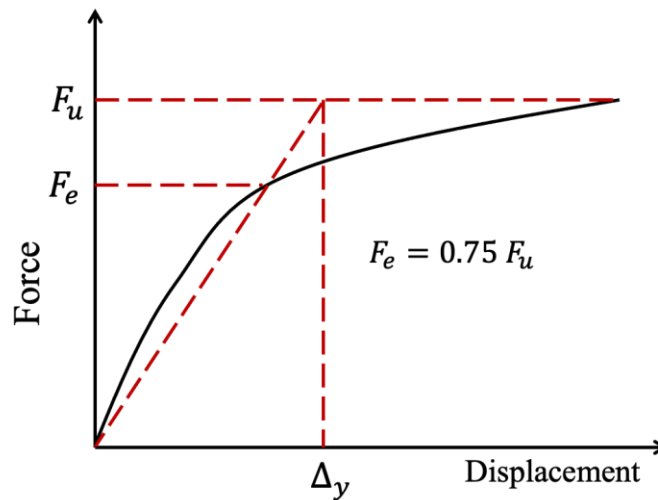
Figure 3.1 Definition of yield displacement

Based on the above definition of ductility, the GT/R team synthesized data from the experimental database to enable the development of fragility models that incorporated uncertainty in the full distribution of EDP values (e.g., 10th, 50th, 90th percentile) assigned to different damage states. The primary work carried out by the GT/R team was to assign ductility values observed in the testing to the different component capacity limit states. The notation and description used to classify the damage states are listed in **Table 3.1**. To fit all anticipated uses of the CCLS models within Caltrans, eight damage Component Damage States (CDS) are defined (CDS_0 to CDS_7, with CDS_0 corresponding to an essentially elastic response resulting in 'no observable earthquake damage').

Table 3.1 Column Damage States and Consequences

Limit State	Likely Damage	Likely Consequence
DS_0	None	None or Scheduled Maintenance
DS_01		
DS_1	Cracking of concrete cover	Patch and paint
DS_12		
DS_2	Minor spalling of concrete cover	Concrete removal, minor epoxy injection, patch and paint
DS_23		
DS_3	Major spalling of concrete cover (exterior to confined zone)	Concrete removal, major epoxy injection, patch and paint
DS_34		
DS_4	Exposed concrete core (damage extends into confined zone)	Strengthening through column jacketing (steel or FRP)
DS_45		
DS_5	Bar buckling, loss of confinement (or core shedding)	Column replacement
DS_56		
DS_6	Multi bar rupture, core crushing, large residual drift	Column replacement and/or bridge replacement (superstructure and column)
DS_67		
DS_7	Column collapse or near total loss of vertical carrying capacity	Bridge replacement

The seven thresholds between adjacent states are labeled CDST_01 to CDST_67 and are associated with the 'initiation' of a specified level of column damage as a function of displacement ductility (DD). The efforts by the GT/R team were successful in capturing DD values for five of the seven 'observable' damage states (not considering CDST_0 which is a non-damaged state) corresponding to all but CDST_23 and CDST_67 as well as a quantitative metric herein labeled 'Failure_080' which is the DD value corresponding to 80% remaining lateral capacity. This specific metric was selected because a majority of the reported experiments ceased testing when the lateral resistance of the tested column lost 20% of its peak resistance. It is critical to note that DD values are NOT reported at all states for most specimens. An individual test may provide DD values for only a few states, and those reported vary by specimen. Therefore, the compilation of DD data at each state represents different combinations of specimens. Further, there is substantial dropout (dearth of data) of observations at the highest state (CDST_56) which complicates interpretation.

3.2.2   Database of bridge column experiments

As previously indicated, the columns in the database were classified into three broad design eras, based primarily on typical ranges of the transverse reinforcement ratio and other reinforcing details as follows:

- Era-1: pre-1971 pre-ductile design, transverse reinforcement ratio 0.1% – 0.25%, perimeter reinforcement with optional cross-ties on rectangular sections, weak closure details include 18-in lapped-hoop (circular) and 90-degree corner hooks (rectangular), longitudinal steel lap slices with foundation starter bars common, column confinement ends at top of cap/footing

- Era-2: 1971 – 1990 early ductile design, transverse reinforcement ratio 0.3% – 1.0%, continuous spiral reinforcement with range of stronger closure details (135-degree hooks, mechanical couplers, welded), overlapping circular cores for wide sections, variable depth of column confinement into cap/footing

- Era-3: post 1990 modern ductile design, transverse reinforcement ratio 0.55% – 1.35%, larger confinement bar sizes, machine-welded closure detail, column confinement extends fully into cap/footing

The focus of this study is on Era-1 columns that may generally be classified as non-ductile components with failure resulting from three modes: flexure, shear and mixed flexure-shear. A first step in classifying capacity limit states was to examine Era-1 columns in the database as discussed in the next section.

3.2.3   Ductility-based limit states

The current version of the database compiled by the Caltrans-GT/R team is available for download from DesignSafe (http://doi.org/10.17603/ds2-0nr1-8571). The data is organized in a spreadsheet and contains a compilation of uniformly processed displacement-ductility values organized by damage state along with associated column-specimen details and test metadata as well as citations with links for a set of 191 column capacity tests from the research literature. In the present study, ductility data corresponding to all limit states were extracted for all columns classified as Era-1 columns. The columns were then further classified into three groups: flexural failure modes only, shear failure modes and mixed modes of failure as shown in **Table 3.2**. Many of the reported tests do not contain adequate information to classify all seven damage states – for example damage states DS_23 and DS_56 are available for only a single experiment

39

under flexural failure modes. Likewise, when considering shear failure modes, data on several damage states (DS_34, DS_56 and DS_67) are limited or unavailable. Eventually, the distribution of damage states were evaluated for three subsets: all columns in the database irrespective of failure mode, flexural modes only (if sufficient damage data was available) and non-flexural modes (shear or mixed flexure-shear).

Table 3.2 Number of specimens in database with identified damage states

Damage State	Failure Mode			
	Flexure	Shear	Mixed	
All columns in database				*Total*
DS_01	8	3	13	*24*
DS_12	10	9	8	*27*
DS_23	1	8	1	*10*
DS_34	6	1	10	*17*
DS_45	14	13	15	*42*
DS_56	1	0	4	*5*
DS_67	5	0	1	*6*
RemCap_80	15	13	17	*45*
Columns with axial stress ratio <= 15%				
DS_01	6	3	5	*14*
DS_12	3	6	5	*14*
DS_23	1	6	1	*8*
DS_34	4	1	5	*9*
DS_45	7	10	8	*25*
DS_56	1	0	0	*1*
DS_67	5	0	1	*6*
RemCap_80	8	10	9	*27*

Figure 3.2 summarizes the probability of exceeding a given damage state for all Era-1 columns from the database. While early damage states through DS_34 show correlation with ductility demands, the fragilities for higher damage states exhibit erratic trends – this is a consequence of limited data for extreme damage states beyond DS_45. In particular, the fragility for damage states in the proximity of collapse (DS_56 and DS_67) is based on only 5 and 6 data points, respectively. When examining damage states for columns failing only in flexure (**Figure 3.3**), the correlation with ductility demands is once again imprecise for damage state DS_45 and data for states DS_23 and DS_56 are extremely limited to facilitate any statistical assessment. Interestingly, when non-flexural failure modes are considered, the fragility curves for the different damage states up to DS_56 (**Figure 3.4**) exhibit the most reasonable correlation with ductility demands. Note that non-flexural failure also includes columns that may yield in flexure prior to deterioration due to shear.
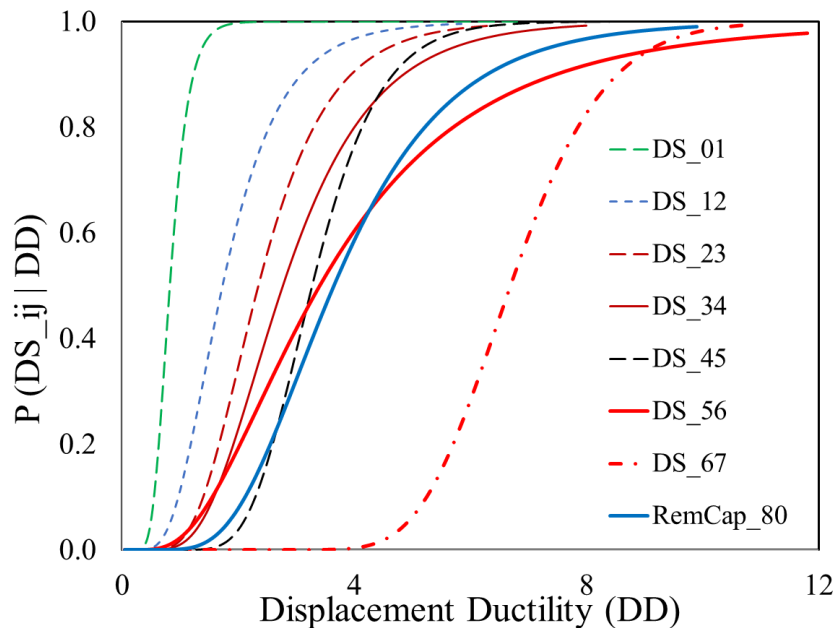
Figure 3.2 Exceedance probability of different damage states for ERA-1 columns
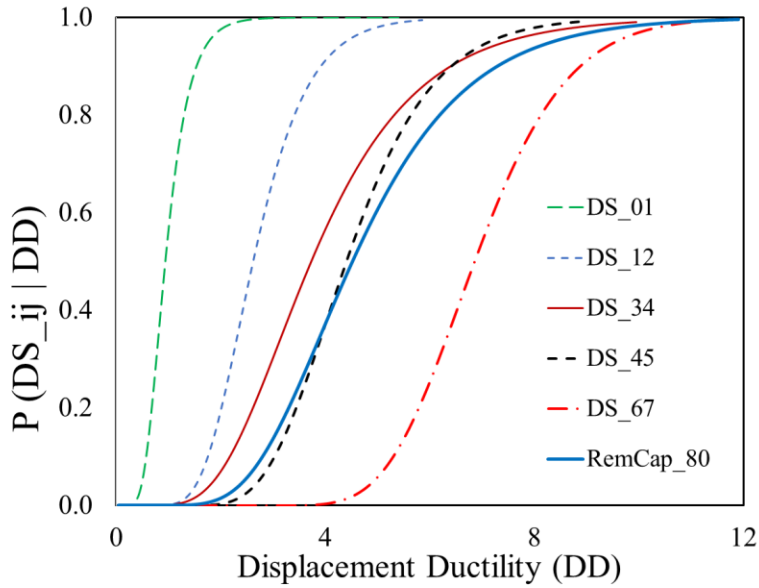
Figure 3.3 Fragility curves for Era-1 columns failing in flexure
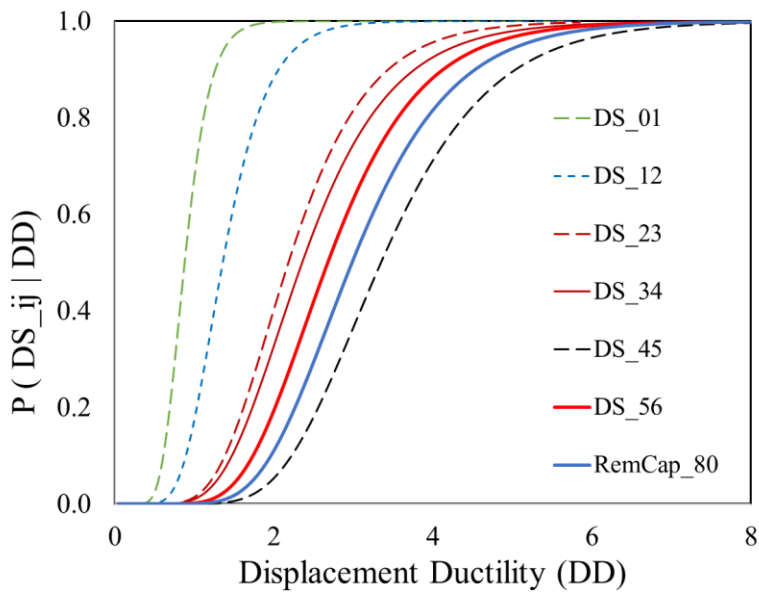
Figure 3.4 Fragility curves for ERA-1 columns failing in non-flexural modes

Next, the fragilities are compared for two specific damage states (for which adequate data is available) for the three groups: all columns (irrespective of failure mode), columns failing in flexure only and failure resulting from shear or mixed failure modes. Results are presented in **Figure 3.5** for damage states corresponding to DS_12 and DS_34. As expected, it is evident that

ductility demands for columns failing in flexure are much higher than non-flexural failure modes. The estimated damage probabilities using the entire database without classifying failure modes represents a reasonable average of the two groups (flexure vs. non-flexural failure modes).
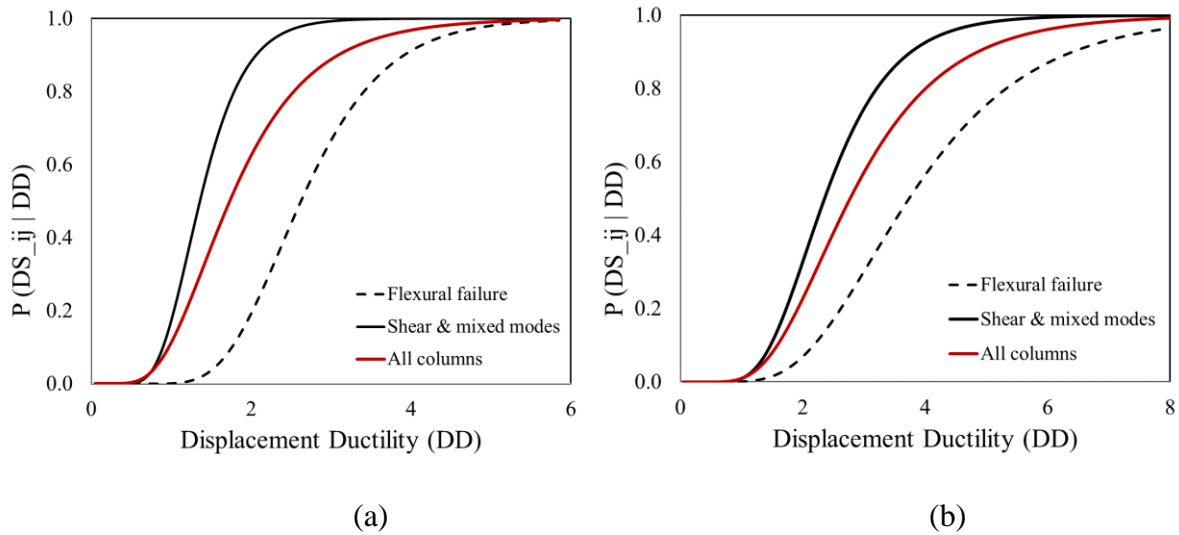
Figure 3.5 Comparison of fragility curves based on group classification: (a) Damage state DS_12; (b) Damage state DS_34

Finally, the database was sorted based on the axial stress imposed on the columns. Bridge columns typically experience normalized axial stress ratios $(P/f_c' A_g)$ less than 0.15. If the experimental data is reclassified such that only columns with axial stress less than 15% are considered and denoted as "typical bridge columns", the computed fragilities are compared in Figure 3.6 for two damage states: DS_45 and RemCap_80. While the damage state corresponding to RemCap_80 is similar for both groups (this limit state is contentious since it does not represent a well-defined damage state), it is evident that using data from columns with higher axial loads is more conservative when applied to typical bridge columns that are subjected to lower axial loads.
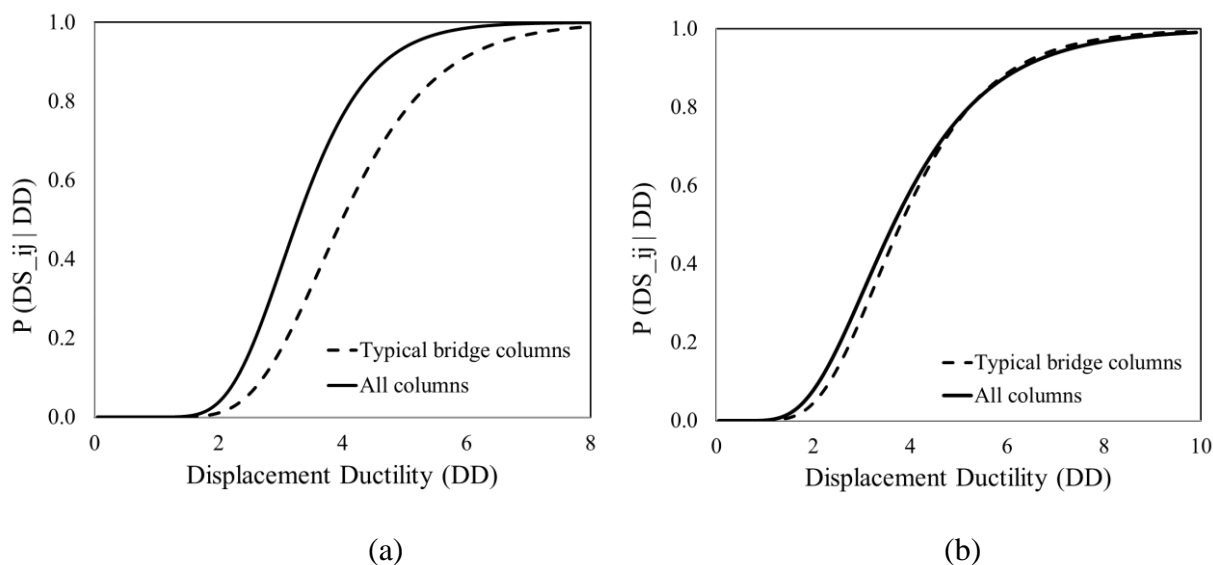
Figure 3.6 Fragility curves considering typical bridge columns:
(a) Damage state DS_45; (b) Damage state RemCap_80

3.3 Strain-Based Calibration of Capacity Limit States

The ductility-based capacity limit states for non-ductile bridge columns presented in the previous section were developed exclusively from experimental data available in the literature. As already noted, approximately half the tested columns had imposed axial loads that are much higher than typical bridge columns. In order to develop CCLS models using a much larger dataset, it was decided to numerically simulate the response of typical bridge columns with cross-sectional details that are similar to Era-1 Caltrans columns.

The CCLS models summarized in Section 3.2 were based on the uniform definition of yield displacement illustrated in **Figure 3.1**. While this appears to be a reasonable approach to defining ductility-based limit states, it was concluded that a more consistent basis to associating sectional behavior to element response was necessary to calibrate damage limit states in the context of numerical simulations. Since a fiber-based model is used in OpenSees, utilizing

material strains in the core, cover concrete and reinforcing steel will provide a more rational means to assess the state of damage in the cross-section. Consequently, damage states are better defined using material strains and then correlated with global response measures such as drift and ductility. For example, the initiation of cracking, spalling of concrete, bar buckling, etc. can be associated with well-defined strain states in the material. The calibration of capacity limit states can then be corroborated with observed experimental data.

3.3.1   Monitored sections

For each column during a particular analysis, axial strains are monitored at several sections. In the cover region, the fiber just outside the core concrete (fiber C1) is monitored; in the core, three fibers located at layers CR1, CR2 and CR3 are monitored. The strain in the reinforcing steel is recorded at different locations and the locations of each layer for a typical circular section are shown in **Figure 3.7**.
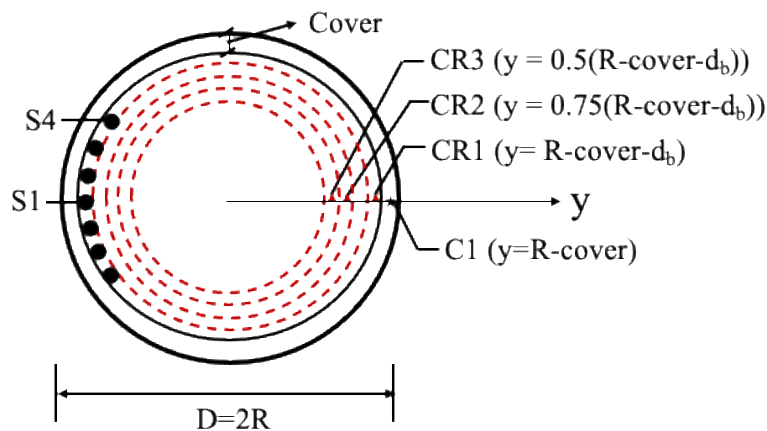
Figure 3.7 Fibers where strains are monitored in circular section

Likewise, for rectangular sections, a section just outside the core concrete (fiber C1) and three fibers (CR1, CR2 and CR3) in the confined core are monitored, as shown in **Figure 3.8**.

The strain in the reinforcing steel is recorded at locations corresponding to S1 and S2. The monitored concrete fibers and reinforcing bars are displayed in in **Figure 3.8**. These locations are selected based on damage states reported in experimental testing.

Figure 3.8 of fibers/section showing labels:
CR1 (y = R-cover-d_b)
C1 (y = R-cover)
y
CR2 (y = 0.8(R-cover-d_b))
CR3 (y = 0.65(R-cover-d_b))
S1, S2
D =2R
*fiber thickness = $2d_b$
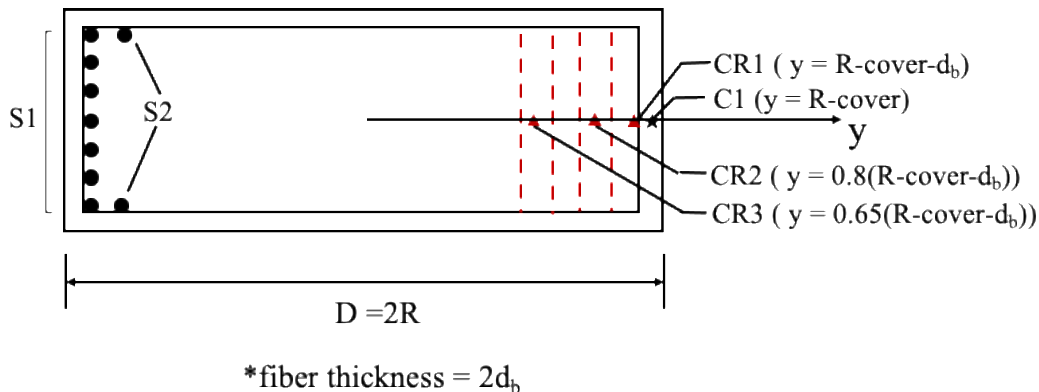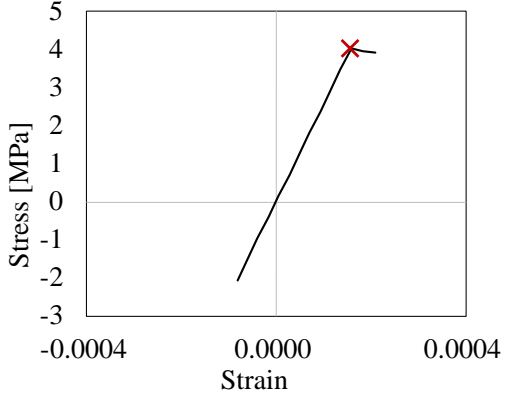
Figure 3.8 Fibers where strains are monitored in wide rectangular sections
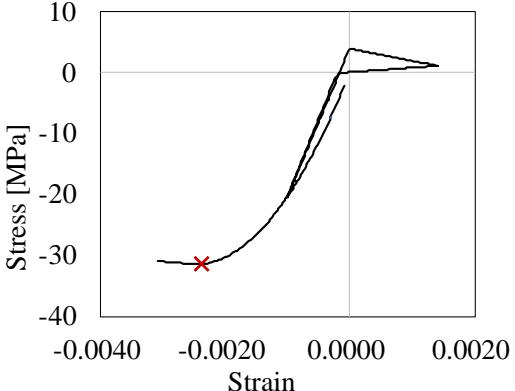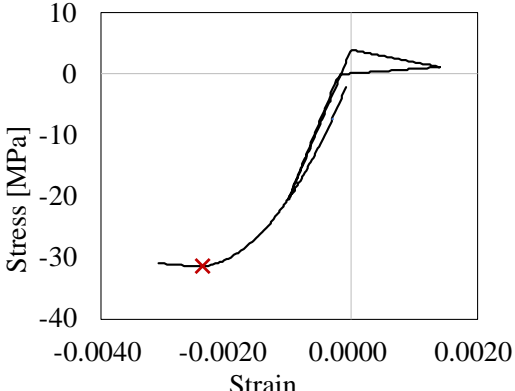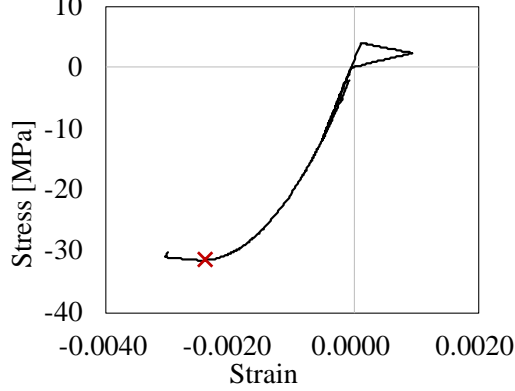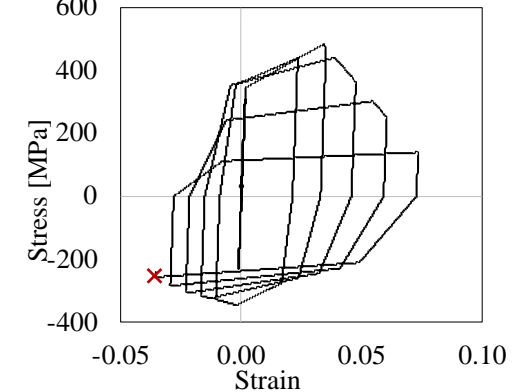
3.3.2   Ductility-Based damage states and correlation with material strains
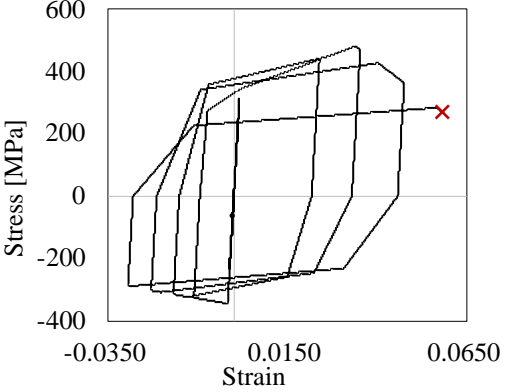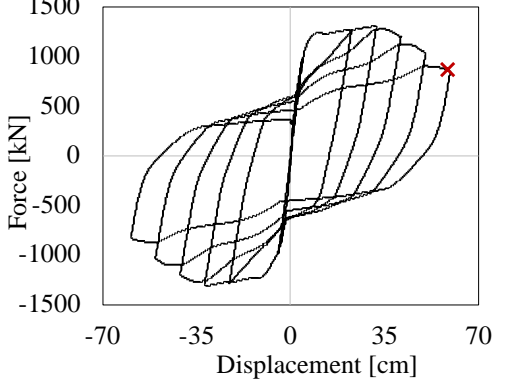
The performance of a bridge column is classified into seven damage states with notation and description as specified Table 3.3. Section C1 corresponds to the layer just outside the core and damage state DS_1 requires the crack to propagate up to but not inside the core. In damage state DS_2, the first layer inside the core reaches its compressive strength. Both these damage states are relatively minor and will not require structural repairs. In the next state, DS_3, the crushing progresses through several layers inside the core resulting in major spalling that will require chipping/removal of damaged sections and concrete replacement. Some of the longitudinal steel will have exceeded their yield strength. Damage state DS_4 is an advanced damage state where the exposed core indicates the need for seismic strengthening. Steel yielding

in circular sections will have progressed to multiple bars but there should be no evidence of bar

buckling. The buckling of longitudinal bars (DS_5) is usually considered an irreparable damage

state. Beyond this state, excessive buckling and possible rupture of bars is likely and the stability

of the bridge column (and the entire bridge depending on the redundancy of the system) is

compromised. The current material model used in the simulation is incapable of capturing low-

cycle fatigue effects and rupture of bars due to highly localized strains in the buckled profile,

hence only the initiation of buckling in multiple bars is monitored. Finally, collapse states are

defined as DS_7 when the lateral strength reduces to less than 50% of the peak strength. This

assumption is reasonable for the considered loading protocol. It is acknowledged that other

measures need to be considered to identify a potential collapse state that more accurately

represents seismic loading. **Table 3.3** displays the stress-strain responses in critical fibers for

different damage states.

Table 3.3 Classification of damage states

Notation	Damage state (Consequence)	Damage description	Stress-strain responses in critical fibers
DS-1	Negligible (patch and paint)	Cracking of cover: Tension cracking at fiber C1	

DS-2	Minor (epoxy if needed, patch and paint)	Minor spalling: Confined concrete in fiber CR1 exceeds compressive strength	
DS-3	Minor to moderate (remove damaged concrete, patch & paint)	Major spalling: Confined concrete in fiber CR2 exceeds compressive strength and longitudinal steel in fiber S1 yields	
DS-4	Moderate to severe (restore strength through added confinement such as jacketing)	Exposed core: Confined concrete in fiber CR3 exceeds compressive strength and no buckling in longitudinal steel	
DS-5	Severe (replace column)	Buckling of outermost longitudinal bar S1	

DS-6	Extremely severe with likely instability of system (replace damaged column)	Rupture of multiple longitudinal bars	
DS-7	Collapse (bridge replacement)	50% loss in lateral strength observed in load-displacement response following damage state DS-6	

3.3.3   Validation of strain-based limit states

The four Era-1 columns that were previously considered in the validation study (Chapter 2) are utilized here to calibrate observed capacity limit states with simulated strains in the selected fiber sections of the numerical model. Results are summarized in **Table 3.4** – **Table 3.7**.

Table 3.4 Simulated damage limit states (Chai et al. 1991)

Column damage state	DS-1	DS-2	DS-3	DS-4	DS-5	DS-6	DS-7
Definition	*Cracking of cover*	*Minor Spalling*	*Major Spalling*	*Exposed core*	*Bar buckling*	*Multi-bar rupture*	*Column collapse*
Drift (in)	0.22	1.32	1.47	2.22	4.32	5.31	5.31
Ductility	0.25	1.52	1.69	2.55	4.97	6.10	6.10
Notes from experiment	1. Spalling of cover concrete developed at ductility = 3 2. Failure did not occur until ductility = 5, when the compression buckling of longitudinal reinforcement destroyed the integrity of the concrete compression zone.						

Table 3.5 Simulated damage limit states (Ranf et al. 2006)

Column damage state	DS-1	DS-2	DS-3	DS-4	DS-5	DS-6	DS-7
Definition	*Cracking of cover*	*Minor Spalling*	*Major Spalling*	*Exposed core*	*Bar buckling*	*multi-bar rupture*	*Column collapse*
Drift (in)	0.05	0.41	0.50	0.86	1.10	1.44	2.34
Ductility	0.24	2.07	2.52	4.32	5.50	7.20	11.70
Ductility reported in experiment	< 1.5	< 6	≤ 6		6.27-8.27		10.63

Table 3.6 Simulated damage states (Soesianawati 1986)

Column damage state	DS-1	DS-2	DS-3	DS-4	DS-5	DS-6	DS-7
Definition	Cracking of cover	Minor Spalling	Major Spalling	Exposed core	Bar buckling	multi-bar rupture	Column collapse
Drift (in)	0.10	0.49	0.66	0.93	2.24	3.78	3.84
Ductility	0.27	1.32	1.78	2.51	6.05	10.22	10.38
Notes from experiment	1. Extensive cracking at the second cycle of ductility = 2. 2. Severe cover concrete spalling at the first cycle of ductility =6; transverse hoop and the corner longitudinal bar became visible. 3. Buckling of longitudinal bars visible at ductility = 8 4. Significant buckling at ductility = 10; opening of anchorage bends at hoop ends						

Table 3.7 Simulated damage limit states (Sun et al. 1993)

Column damage state	DS-1	DS-2	DS-3	DS-4	DS-5	DS-6	DS-7
Definition	Cracking of cover	Minor Spalling	Major Spalling	Exposed core	Bar buckling	multi-bar rupture	Column collapse
Drift (in)	0.17	1.17	1.40	1.59	4.84	4.84	4.84
Ductility	0.19	1.25	1.50	1.70	5.19	5.19	5.19
Notes from experiment	1. Significant cracking at ductility = 2 2. Major spalling of the cover concrete occurred at ductility = 3 3. Buckling of longitudinal reinforcement at ductility = 4						

It is observed that spalling occurs in the ductility range 1.0 – 2.0 though the distinction between minor and major spalling is difficult to establish. An extreme limit state where bar buckling is visible happens at ductilities near 5.0. With the exception of the test by Ranf et al., bar rupture was typically equated with a near-collapse condition.

3.4   Selection of Bridge Columns for Numerical Study

There are over 24,000 bridges in the Caltrans inventory with varying column sizes and detailing configurations. After identifying bridge columns that belong to Era-1, it is essential to further classify these columns into suitable subsets based on cross-section shape, transverse and longitudinal reinforcement detailing. It was also necessary to associate the columns with bridge types (single or multi-column bent, girder type and support conditions) since the response and failure mode may vary depending on the bent layout, foundation, and superstructure.

3.4.1   Circular columns

A survey of the salient features of existing circular pre-1971 Caltrans columns shown in **Figure 3.9** indicates that most Era-1 columns had a height to diameter (H/D) ratio of 4.0 or higher, longitudinal steel ratio varying from 1% to 3% and transverse steel ratio in the range of 0.1% to 0.3%. The goal of the simulation was to generate a reasonable number of column configurations representative of Era-1 columns, vary a modeling parameter to alter the rate of degradation, and finally consider different loading protocols.

(a)   (b)
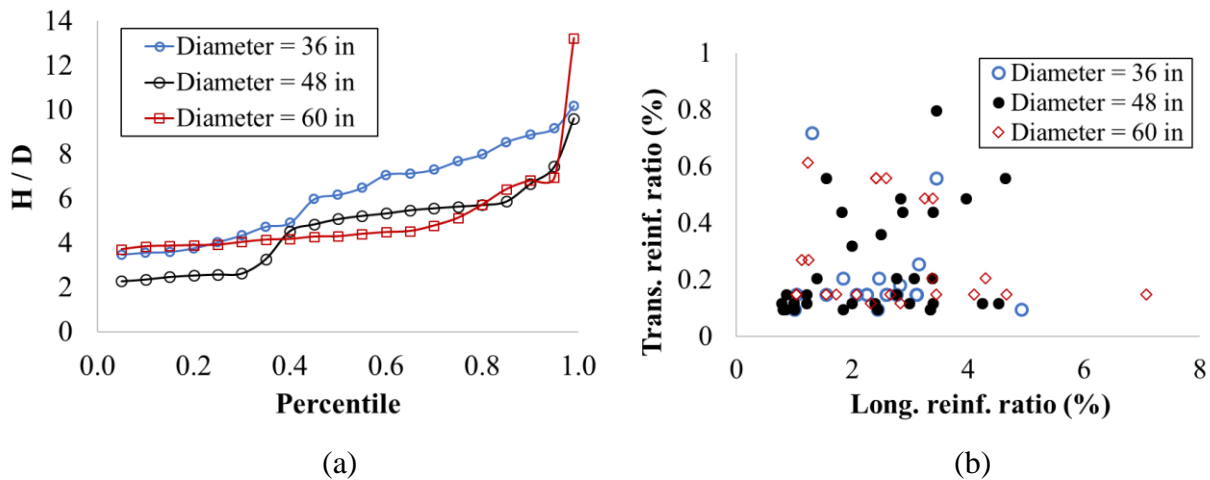
Figure 3.9 Typical characteristics of Era-1 circular columns

Consequently, the hypothetical columns selected for the numerical simulations had longitudinal steel reinforcement of 1%, 2% and 3% and transverse reinforcement of 0.12%, 0.18% and 0.24%. A few outliers were also added to the simulation study wherein one column was provided 5% longitudinal steel and two columns had higher transverse reinforcement. The column diameters were selected to be 60 in (152 cm). for all columns. An H/D ratio of 6.0 was assumed resulting in column heights of 30 ft (9.14m). Specific reinforcing details for each of the seven columns is provided in **Table 3.8**.

Table 3.8 Details of circular columns selected for numerical simulation

Column #	1	2	3	4	5	6	7
Trans. reinf.	#4	#4	#4	#4	#4	#7	#8
Spacing (in)	6	12	12	12	8	8	12
Trans. steel ratio	0.24%	0.12%	0.12%	0.12%	0.18%	0.55%	0.48%
Long. reinf.	32 # 14	11 # 14	32 # 14	21 # 14	30 # 18	19 # 10	45 # 14
Long. steel ratio	3.0%	1.0%	3.0%	2.0%	5.0%	1.0%	4.3%

3.4.2   Wide rectangular sections

Many of the pre-1971 Caltrans bridges contain fairly wide rectangular sections. Salient features of the rectangular columns are shown in Figure 3.10. The height to depth ratios for most columns exceed 3.0 suggesting a primarily flexural response. The cross-sectional aspect ratio (B/D) varies from 2.0 to 3.0 with some depths exceeding 96". Similar to circular columns, most wide-section Era-1 columns were designed with longitudinal steel ratio ranging from 1% to 3%

and transverse steel ratio between 0.1% and 0.3%. In the present study, five configurations were

considered, as shown in **Figure 3.11** and **Table 3.9**.
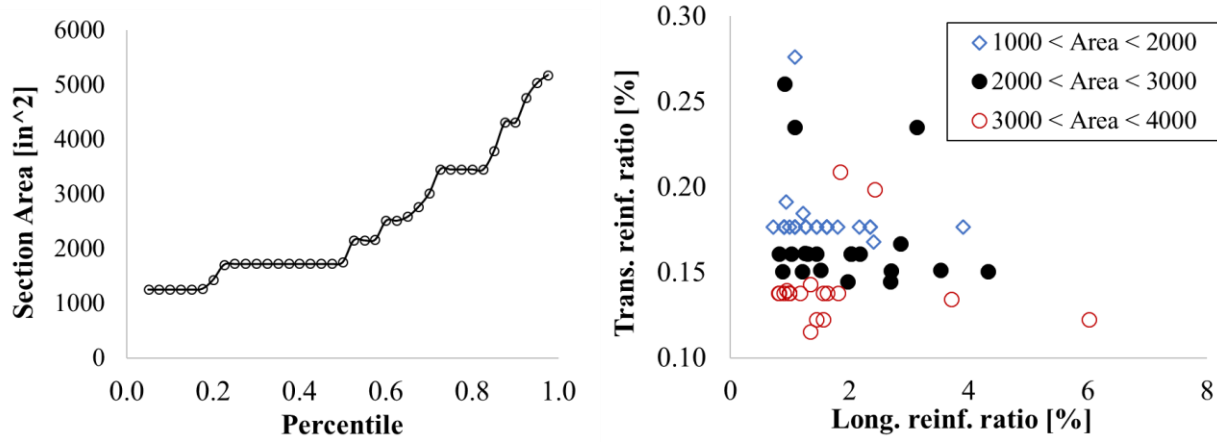
Figure 3.10 Basic characteristics of Era-1 wide rectangular sections
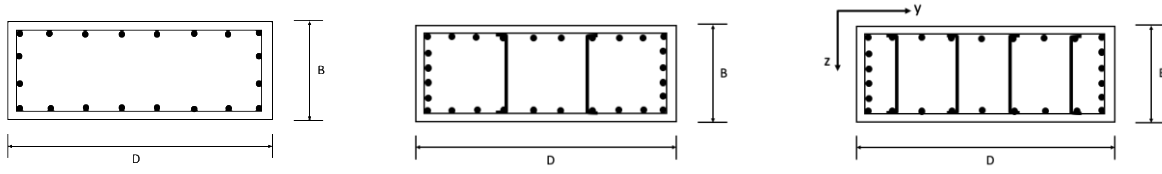
Figure 3.11 Configurations of selected wide section columns

Table 3.9 Cross-section and reinforcement details of selected wide section columns

Column #	1	2	3	4	5
B (in)	36	36	36	36	36
D (in)	72	96	96	72	72
Height (ft)	36	48	48	36	36
Trans. reinf	# 4	# 4	# 4	# 4	# 4
Spacing (in)	12	12	12	15	15
Trans. Steel Ratio	0.23%	0.23%	0.15%	0.12%	0.12%
Long. Reinf	28 #14	26 # 11	20 # 11	28#14	40#14
Long. Steel Ratio	3.0%	1.4%	1.0%	3.0%	4.2%

3.5   Loading protocols

Several loading protocols were considered ranging from quasi-static cyclic loads to random seismic inputs. In the case of cyclic loading, both circular and wide-section columns were subjected to single cycles at increasing amplitudes and multiple cycles at increasing amplitudes. Three cyclic loading protocols as shown in **Figure 3.12** were imposed.
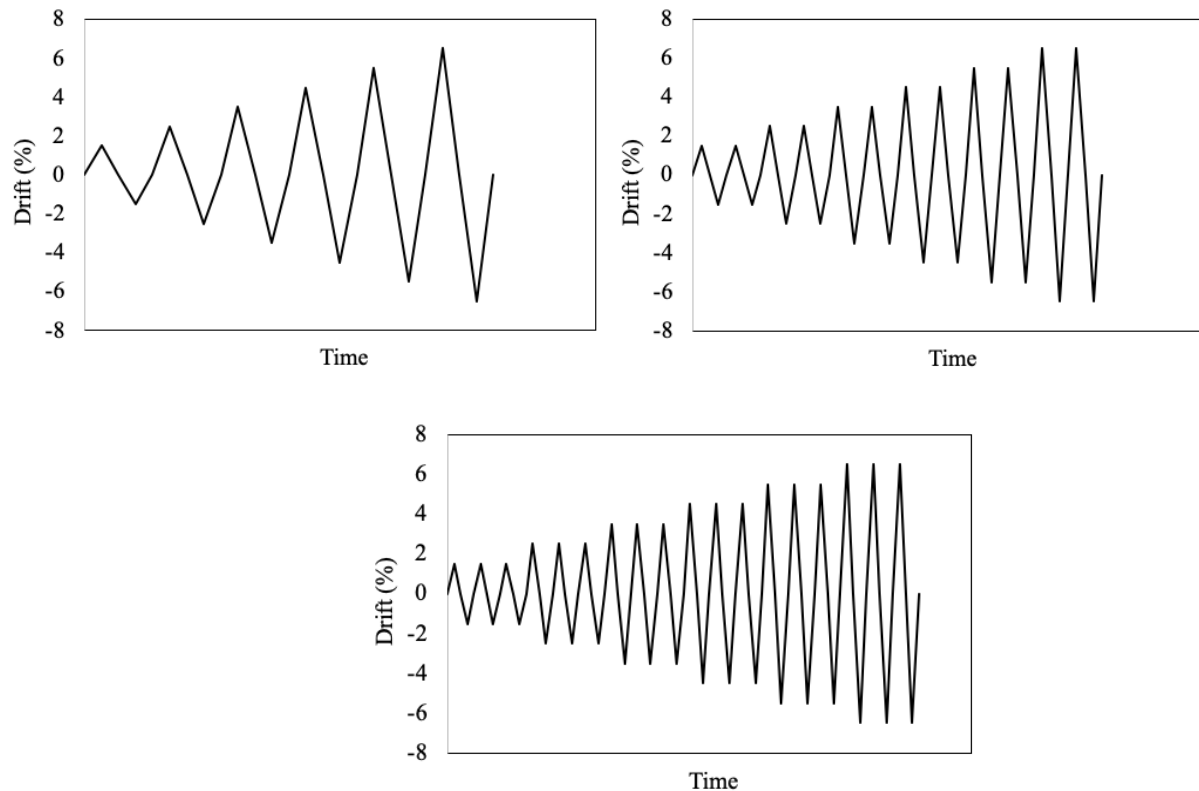
Figure 3.12 Loading protocols used in present study: single cycle, two cycles and three cycles at increasing amplitudes

3.6   Capacity Limit States for Circular Columns

The seven selected columns (**Table 3.8**) were subjected to reversed cyclic loads using the three loading protocols shown in **Figure 3.12**. In addition, to introduce modeling uncertainty into the simulations, three different values of the ductility-based damage parameter were specified in

characterizing the cyclic response of reinforcing steel modeling (Note that the damage due to ductility is denoted as $damage1 in the Hysteretic material in OpenSees and were assigned values of 0.01, 0.02 and 0.03 in this study). Hence each of the seven columns was subjected to three cyclic histories and three different damage parameters for a total of 9 simulations per column. The stress-strain responses of the various concrete and reinforcing steel fibers were analyzed for the resulting 63 responses to estimate the maximum ductility demands at each damage limit state (in accordance with the criteria identified in **Table 3.1**). **Figure 3.13** summarizes the median, 10 and 90 percentile ductility demands for various damage states. The median demand for states DS-2 and DS-3 are almost identical indicating challenges in distinguishing these limit states.
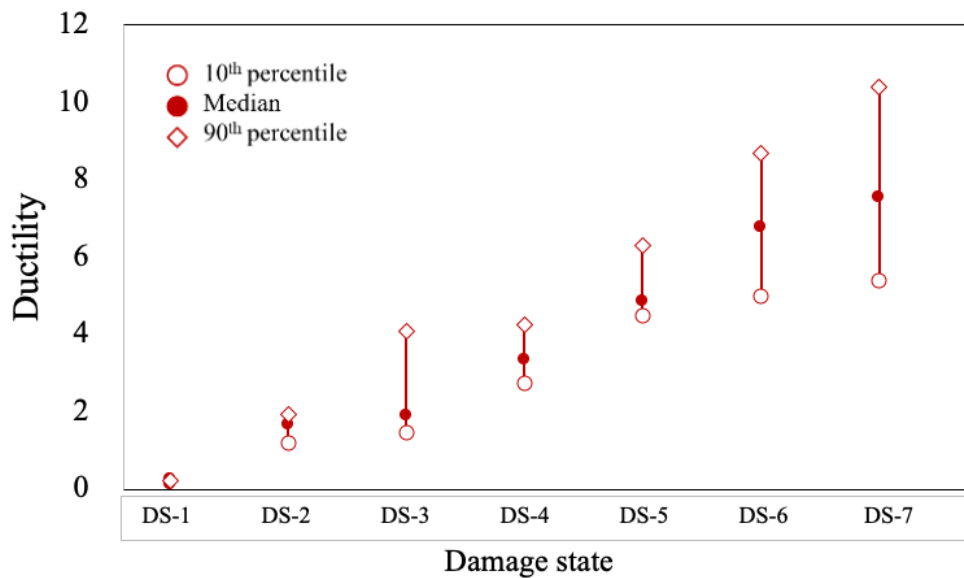
Figure 3.13 Distribution of ductility demands for various damage states

In **Figure 3.14**, the ductility demands estimated through numerical simulations is compared to the experimentally observed demands for two typical limit states. The median and dispersion for an extreme damage state (DS_67 according to the Caltrans classification described

56

in **Table 3.1** and DS-7 in the classification used in the present study as presented in **Table 3.3**) are similar suggesting that numerical predictions of a higher damage state can be comparable to an experimental observation. However, the distribution for a lower damage state (DS_34 or DS-4) indicates that the dispersion in experimental observations is notably higher than numerical predictions. It was previously noted that calibrating a ductility demand to major spalling was challenging since experimental reporting of this damage state varied between researchers. Yet, the median ductility demand for this damage state did not differ significantly (~3.5 in the numerical study versus ~3.75 in the experiments).
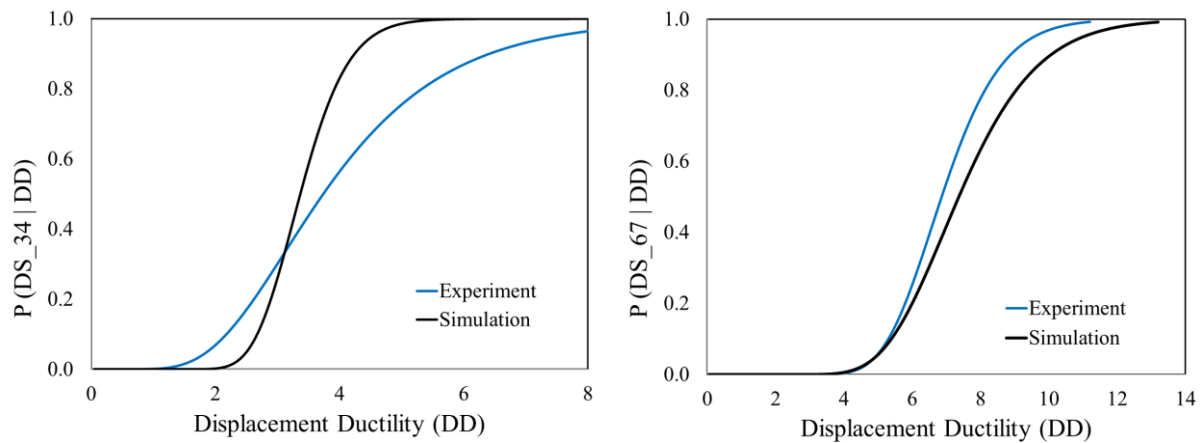
Figure 3.14 Comparing numerically simulated median and dispersion with experimental data for two damage states

Figure 3.15 presents the effect of loading history on the ductility demands. It was found that the ductility demands do not vary considerably for the cyclic loading protocols up to damage state DS-5. For each column under the three different loading protocols, the ductility attained at damage states DS-1 through DS-5 is similar. However, as expected, the dispersion of ductility becomes larger as the damage state moves to DS-6 and DS-7 and the ductility limits drop with increasing number of cycles at each displacement level.
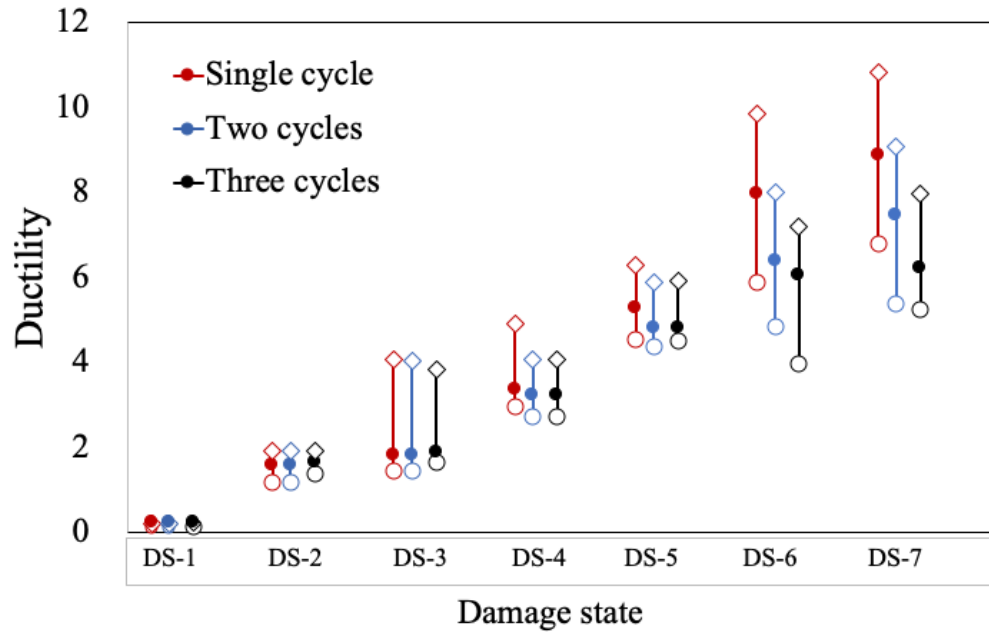
Figure 3.15 Effect of loading protocols for circular columns

3.7   Capacity Limit States for Wide Cross-Sections

The five wide rectangular section columns were subjected to reversed cyclic loads using the

three loading protocols shown in **Figure 3.12**. Additionally, as was done with circular columns,

three values (0.01, 0.02 and 0.03) of the ductility-based damage parameter were specified to

introduce additional degradation in the reinforcing steel. Hence, each column configuration is

subjected to nine simulations resulting in a total of 45 simulations for the entire subset of wide-

section columns. The ductility demands corresponding to the seven capacity limit states are

shown in **Figure 3.16**. Similar to the observation for circular sections, the median demands for

DS-2 and DS-3 are similar though the dispersion is higher for DS-3. **Figure 3.17** presents the

effect of loading history on the ductility demands where it is seen, similar to finding for circular

columns, that the ductility demands do not vary significantly for the cyclic loading protocols up

to damage state DS-5. In general, the dispersion in the median estimates increases with increasing limit states. Increasing the number of imposed cycles at a displacement level results in lower ductility limits for damage states DS-6 and DS-7.
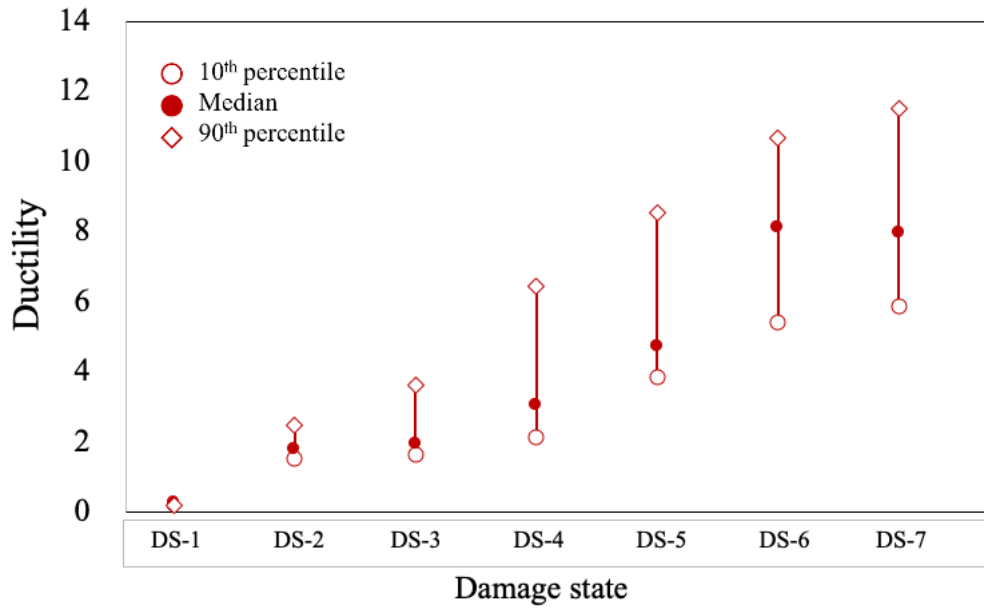
Figure 3.16 Ductility demands for all damage states for wide rectangular sections
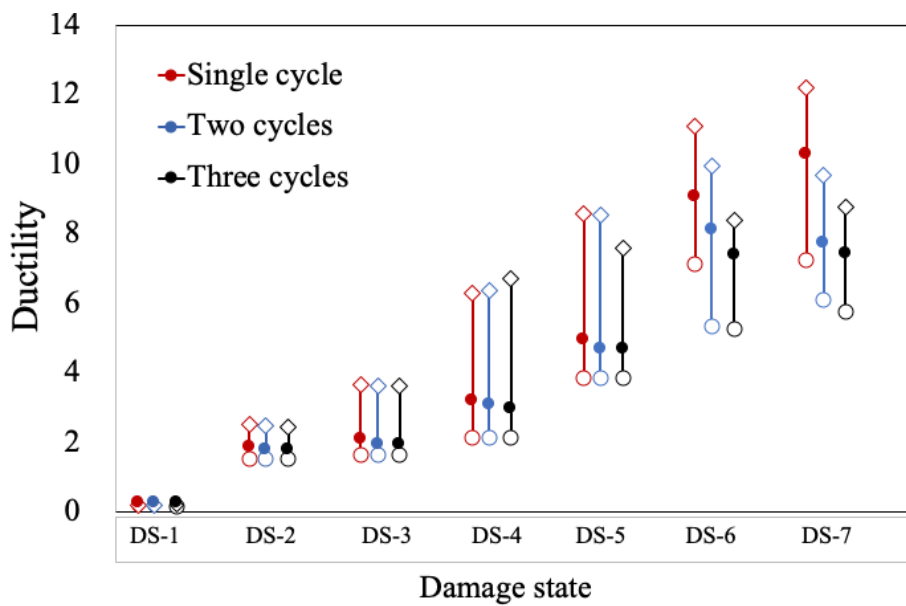
Figure 3.17 Effect of loading protocols for columns with wide sections

Next, the effectiveness of the numerical simulations is assessed by comparing the median and dispersion for two damage states (**Figure 3.18**). Previously, for circular sections, it was found that the numerical simulations compared better with experimental findings for a severe damage state. Here, the median and dispersion for the numerical simulations is in good agreement for a moderate damage state and somewhat less conservative for a more extreme damage state.
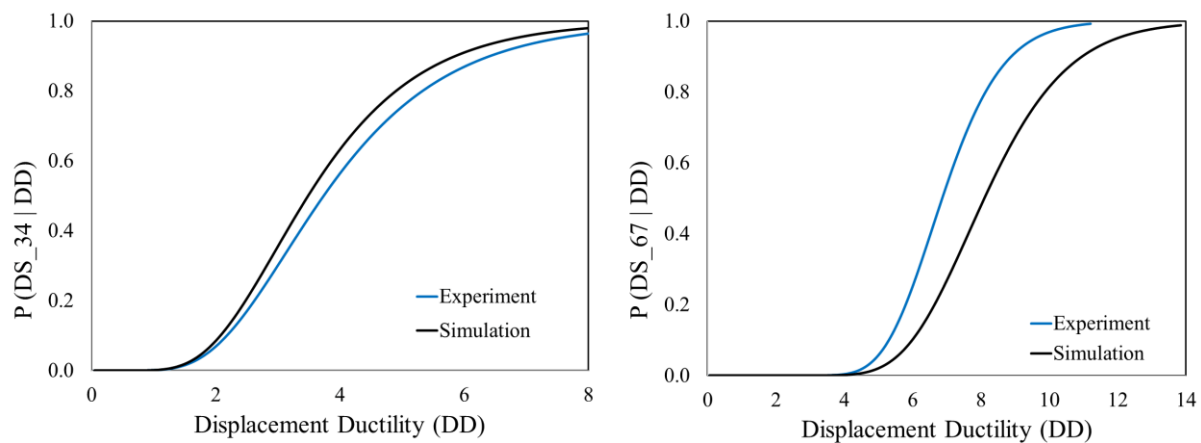
Figure 3.18 Numerically simulated median and dispersion versus experimental data for two damage states

Finally, the expected behavior of circular columns is compared to the wide section columns in **Figure 3.19**. It is evident that wide-section columns perform better than circular columns sustaining higher ductility demands for the same damage limit state. Additionally, the dispersion in the distribution is compared for two damage states in **Figure 3.19**. For a moderate damage state such as concrete spalling, the distribution for wide-section columns exhibits a much greater dispersion than circular columns. At the extreme limit state (DS-7), the median ductility is slightly higher for the wide-section columns and the dispersions for both column sections are more or less similar.
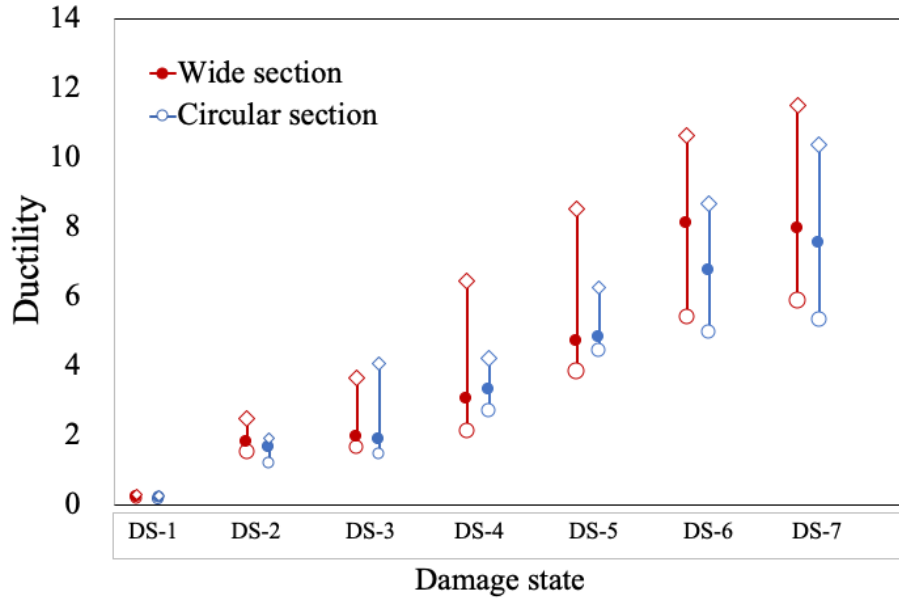
Figure 3.19 Comparison of performance of circular vs. wide-section columns
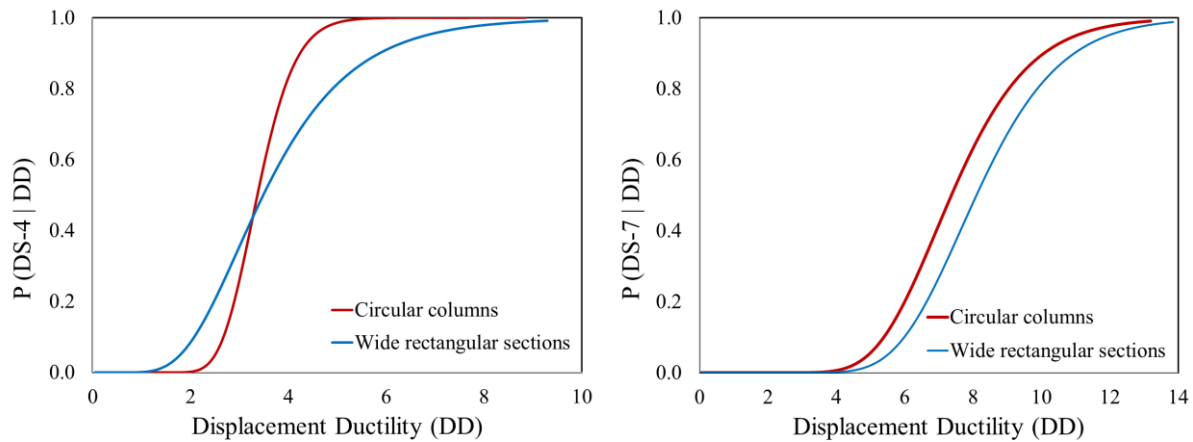
Figure 3.20 Dispersion in ductility demands for two damage states

3.8   Application to Earthquake Loading

The feasibility of using a ductility-based definition of column damage limit states is examined in this section. While drift and displacement-based measures are easily understood by engineers and researchers, it may not always be the most appropriate parameter to predict cyclic damage resulting from earthquake-induced loading. To illustrate this deficiency, one of the

columns used in the numerical simulation (Column #3 in **Table 3.8**) is subjected to seismic

loading. The 5 ft. diameter candidate column has a longitudinal reinforcement ratio of 3% and a

transverse reinforcement ratio of 0.12%. Results from the numerical simulation using the three

cyclic loading protocols is synthesized in **Figure 3.12**. Shown in **Figure 3.21** is the average

ductility demand of the three loading histories as a function of damage limit state. Since the

imposed displacement history consists of a fixed number of cycles at increasing amplitude, the

ductility demands show an increasing trend for higher damage states.
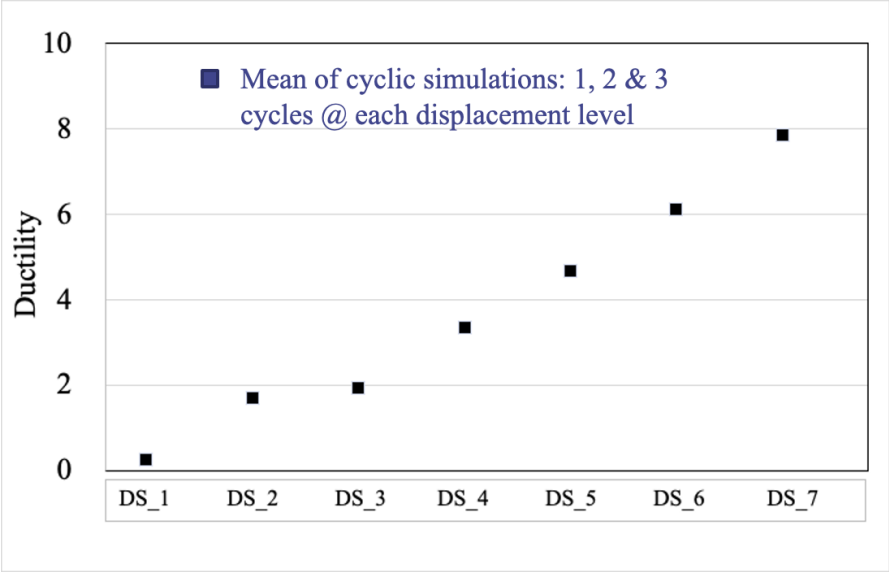
Figure 3.21 Ductility demand versus damage limit state of candidate column

The same column was then subjected to the acceleration history recorded at Parkfield

station during the 1983 Coalinga earthquake (RSN 334 in the PEER earthquake database

https://ngawest2.berkeley.edu/). Since the original record did not cause major damage to the

column, the time series was scaled successively until the final damage state (DS-7) was attained.

The peak ductility attained by the column was recorded at each damage state (Note that all

damage states are correlated to material strain states except for the collapse state which is

defined by a 50% loss of lateral capacity). The ductility demands at each damage state resulting

from the earthquake loading is compared in **Table 3.10** with the corresponding damage state

resulting from the cyclic loading (the mean of the three loading protocols is used for the

comparison). **Figure 3.22** shows the force-deformation response of the column under the

earthquake loading as well as locations at the initiation of each of the seven damage states.

Table 3.10 Comparison of ductility demands for cyclic and earthquake loading

Column damage state		DS-1	DS-2	DS-3	DS-4	DS-5	DS-6	DS-7
Definition		Cracking of cover	Minor Spalling	Major Spalling	Exposed core	Bar buckling	multi-bar rupture	Column collapse
Ductility Demand	Mean of cyclic loading	0.23	1.67	1.90	3.32	4.80	6.10	7.82
	Seismic loading	0.22	1.70	1.95	3.32	4.15	4.15	4.15
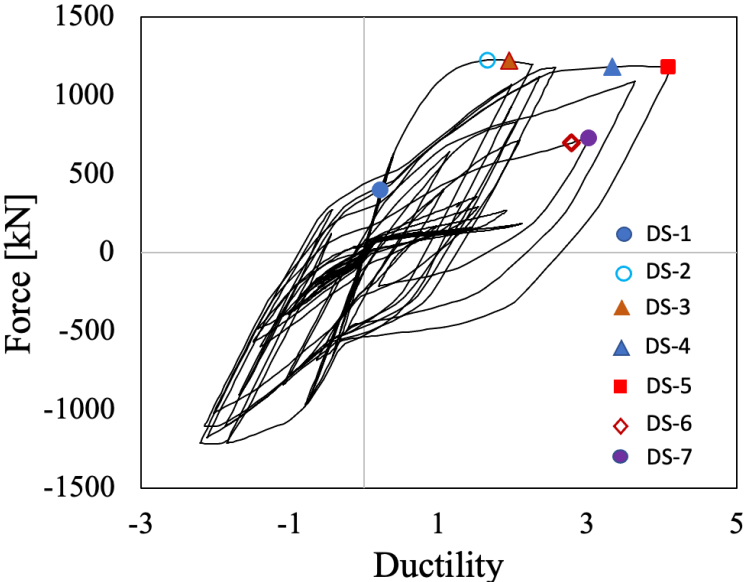
Figure 3.22 Force-displacement response of the column and identified damage states

Reasonable agreement between the two different loading schemes is observed in minor to moderate damage states (DS-1, DS-2, DS-3 and DS-4). However, at higher damage limit states, the ductility-based measure produces inconsistent results since the peak ductility is achieved at an earlier limit state whereas extreme damage states such as bar buckling and severe strength deterioration occurs later at lower ductility demands. As shown in **Table 3.10** and further verified from the force-deformation response shown in **Figure 3.22**, the peak ductility remains constant for the final three damage limit states. A ductility-based damage limit state is thus shown to be incapable of accounting for effects such as delayed bar buckling (when tension yielding causes the bar to buckle at lower strains in compression) and low-cycle fatigue effects.

3.9   Summary

The results from this phase of the study show that ductility can be a reasonable indicator for each damage limit states under cyclic loads. Since ductility requires the estimation of a yield displacement, it is essential to use a uniform definition of the yield point so as to be consistent in adopting a ductility-based limit state classification. However, a ductility-based limit-state definition can run into problems when applied to earthquake loading. As demonstrated in the example in Section 3.8, the peak ductility may have occurred at an earlier limit state whereas material degradation continues at lower ductility levels due to factors such as loss of confinement, low-cycle fatigue, bar buckling and bar rupture. Material limit states such as bar buckling and fracture is influenced by load history and a simple measure such as column ductility is inadequate to predict extreme limit states. Hence it is concluded that a more advanced methodology is needed to capture all capacity limit states when the column is subjected to non-symmetric loading. In the next chapter, a damage-based approach is proposed to establishing capacity limit states that can be applied in post-earthquake damage assessment.

CHAPTER 4.0   DEVELOPMENT OF DAMAGE-BASED CAPACITY LIMIT STATES

4.1   Previous work on damage modeling

A review of the state-of-the-art on damage modeling reveals that, until more recently when material-based damage models began to appear in the literature, there were essentially five approaches to damage modeling of concrete structures: (1) estimates based on measures of deformation and/or ductility; (2) models based on the degradation of a selected structural parameter (typically stiffness); (3) models developed from considerations of energy-dissipation demand and capacity; (4) hybrid formulations combining aspects of deformation and energy; and (5) more complex theories based on concepts derived from fatigue models. Damage models can also be grouped into categories depending on whether the damage index considers cumulative effects. Comprehensive reviews of damage models for seismic assessment of structures can be found in Powell and Allahabadi (1988) and Williams and Sexsmith (1994).

The damage index proposed by Powell and Allahabadi (1988) is an example of a deformation or ductility-based damage index:

$$DI_{PA} = \frac{\delta_{\max} - \delta_y}{\delta_u - \delta_y} \leq 1.0 \text{ and } \delta_{\max} > \delta_y \qquad\qquad 4.1$$

where $\delta_{\max}$ is the maximum lateral displacement of the structure during earthquake, δ_y is the yield displacement and δ_u is the maximum lateral displacement capacity of the structure under monotonic loading. Since the displacement capacity under monotonic loading will be larger than under cyclic loading, this damage index will not reach 1.0 unless collapse/failure is the result of a single large pulse. Recently, as discussed in Chapter 1, Yoon et al. (2019) also used a

displacement-based definition of damage with the main difference being the definition of the

ultimate displacement which is taken from experiments where the column is subjected to cyclic

loading. Another non-cumulative damage index, proposed by DiPasquale and Cakmak (1988),

examines the change in the fundamental period of the system:

$$DI_{DC} = 1 - \frac{T_0}{T_{max}}$$ 4.2

In the above expression, T_0 is the initial period of the system and T_{max} is maximum elongated

first mode period in the inelastic range. This model attempts to formulate damage as a function

of the overall stiffness degradation of the system. A variation of this approach was proposed by

Kunnath et al. (1997) wherein damage is defined by the change in structural stiffness, as follows:

$$D_{KE} = \frac{k_m - k_0}{k_f - k_0}$$ 4.3

With reference to **Figure 4.1 (a)**, k_m is the secant stiffness of the structure at the maximum

induced displacement, k_f is the pre-established stiffness at failure of the system (typically under

monotonic loads), and k_0 is the initial stiffness prior to loading.

(a)   (b)
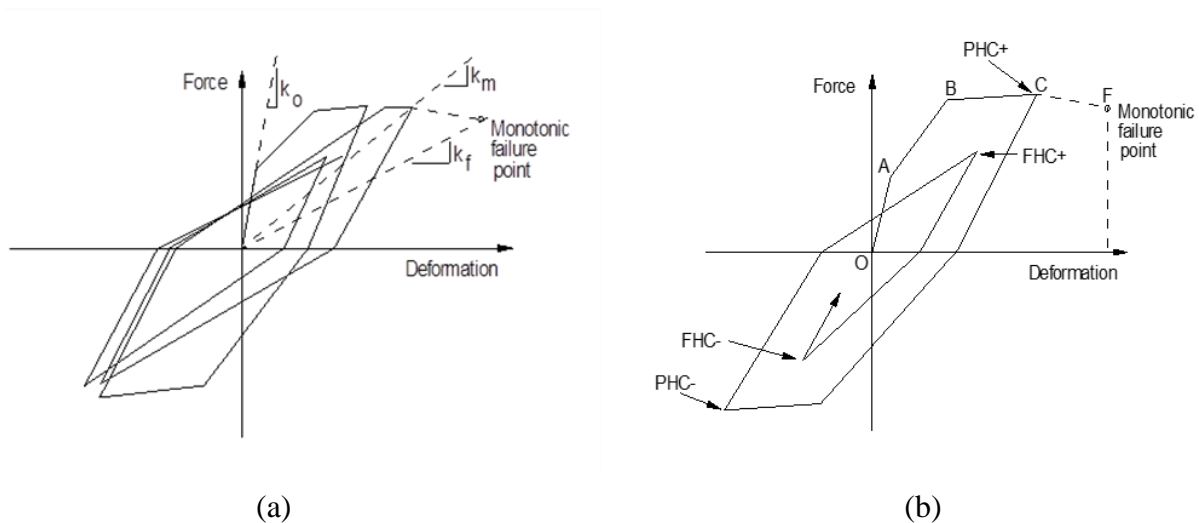
Figure 4.1 Damage models based on (a) Stiffness-degradation; (b) energy-dissipation

Among the earliest cumulative damage models was the energy-based formulation developed by Kratzig and Meskouris (1987). The terminology used to define this model is illustrated in Figure 4-1 (b). A primary half cycle (PHC) is the energy contained in the half cycle at the maximum deformation point. Additional cycles with displacement amplitudes less than the peak deformation are accumulated as follower half cycles (FHC). Positive and negative deformations are treated separately. Accumulated damage for the positive portions of the response is defined as:

$$D^+ = \frac{\sum E^+_{p,i} + \sum E^+_i}{\sum E^i_f + \sum E^+_i} \qquad 4.4$$

where Epi is the energy in a PHC, E_i is the energy in an FHC and E_f is the energy absorbed in a monotonic test to failure (area enclosed by OABCF in Figure 4.1b). A similar expression is computed for negative deformations, and the two quantities are normalized as follows:

$$D_{KM} = D^+ + D^- - D^+D^- \qquad 4.5$$

The inclusion of the follower cycles in the numerator and denominator suggests that their contribution to damage is small, or significantly lower than deformations that extend the response envelope.

A hybrid model that accounts for both ductility and energy was proposed by Park and Ang (1985). It is one of the most widely used damage models in the literature and many researchers have both evaluated as well as suggested possible enhancements to the model. In its original form, damage to a component in the system is determined from:

$$D = \frac{\delta_m}{\delta_f} + \beta \frac{E_T}{F_y \delta_f} \qquad 4.6$$

where δ_m is the maximum deformation, δ_f is the ultimate deformation capacity under monotonic loading, F_y is the yield strength of the component, E_T is the dissipated hysteretic energy and β is a parameter that depends on the characteristics of the RC member and considers the effect of cyclic loading and can typically be estimated from experimental data. Though Park and Ang suggested an empirical expression to estimate β, it was generally found to be inadequate in many applications. However, an important contribution by Park and Ang was the process of classifying the computed damage index (DI) into damage limit states as follows: DI < 0.1 = no damage or localized minor cracking; $0.1 \leq$ DI < 0.25 = minor damage and visible cracking throughout; $0.25 \leq$ DI < 0.40 = moderate damage including localized spalling; $0.4 \leq$ DI < 1.00 = severe damage/concrete crushing, exposed reinforcement exposed; and DI ≥ 1.00 = collapse.

Since seismic loads induce several inelastic cycles at relatively large ductility demands, the concept of using low-cycle fatigue theories to model damage is logical. Though high-cycle fatigue of metals and concrete have been evaluated in the past, few have attempted to extend these concepts to evaluating seismically induced fatigue damage. The formulation of Chung et al. (1987) combines Miner's rule (Miner, 1945) with a failure criteria:

$$D = \sum_i \left[w_i^+ \frac{n_i^+}{n_{f,i}^+} + w_i^- \frac{n_i^-}{n_{f,i}^-} \right] \qquad 4.7$$

In the above expression, where both positive and negative cycles are treated separately, w_i is a weighting factor, n_i is the number of cycles at a given amplitude, and $n_{f,i}$ is the number of cycles to failure at the same amplitude. Other approaches to modeling fatigue failure have also been developed. However, fatigue in this context is applied at the component level. Among the earliest studies examining fatigue at the material scale is a mechanics-based derivation by

Mander and Cheng (1995). They express local section curvature at the plastic hinge region

directly in terms of strain in the rebar:

$$\varphi_p D = \frac{0.113}{1 - 2\,d/D} N_f^{-0.5}$$
4.8

This expression is derived from the plastic strain vs. fatigue life relationship obtained from actual

testing of steel reinforcing bars (Mander et al., 1994) and the relationship between curvature and

strain in a reinforced concrete circular cross-section assuming a linear strain profile.   In

Equation (6-3), φ_p is the plastic curvature, D is the overall column diameter, d is the depth from

the outermost concrete fiber to the center of reinforcement, and N_f is the number of cycles to the

appearance of the first fatigue crack in steel. It must be remembered though that using fatigue

theories presupposes a flexural fatigue failure mode.   Other potential failure modes resulting

from the combined effects of axial force, shear and confinement are not incorporated in these

models.

The material-based fatigue model discussed above is limited to damage estimation in the

reinforcing steel. In order to predict damage to a concrete component, it is also necessary to

incorporate damage progression in concrete – both in the cover and the confined core. Heo and

Kunnath (2013) developed a damage modeling technique utilizing the strains at the material

level in both concrete and steel. Reinforcement damage is based on low-cycle fatigue concepts

whereas concrete damage is established using a bilinear damage evolution process. A very

similar approach has been recently used by Su et al. (2017) to assess the seismic behavior of RC

bridge piers.

In this study, a modified and enhanced version of the methodology proposed by Heo and

Kunnath (2013) is proposed for developing capacity limit states of both single and multi-column

bents. As previously indicated, the study is limited to older pre-1971 California bridge columns with non-ductile detailing.

4.2 Concrete Damage

The estimation of damage in concrete is based primarily on the distress in the confined core because it was determined that calibrating the damage state to compression damage in the core was a better indicator of section damage than incorporating deterioration in both core and cover concrete. Other approaches to assessing concrete damage such as tensile cracking was found to be insignificant since damage from tensile effects is better reflected in the damage to reinforcing steel. Moreover, the response in compression governs the section damage in the concrete core (Heo and Kunnath, 2013). A simple bilinear damage progression model as described in Equations 4.9 – 4.11 is proposed:

$$D_{ci} = \frac{D_{cc}(f - f_{cd})}{(f_{cc} - f_{cd})} \quad for \; \varepsilon \leq \varepsilon_{cc} \qquad \qquad 4.9$$

$$D_{ci} = 1 + \frac{(1 - D_{cc})(f - f_{cu})}{(f_{cu} - f_{cc})} \quad for \; \varepsilon > \varepsilon_{cc} \qquad \qquad 4.10$$

$$D_{cc} = \max\left(0.3, \frac{\varepsilon_{cc} - \varepsilon_{cd}}{\varepsilon_{cu} - \varepsilon_{cd}}\right) \qquad \qquad 4.11$$

In the above expressions, D_{ci} is the concrete damage index at the i_{th} monitored concrete fiber, D_{cu} represents the damage index at the peak compressive strength of confined concrete, f_{cd} is the strength at damage initiation, f_{cc} is the peak concrete compressive strength in confined concrete, f_{cu} is the residual strength in confined concrete, and ε_{cc} denotes the strain at peak concrete compressive strength. Since the stress-strain response of concrete is nonlinear throughout, it is necessary to set a threshold strain at which damage is initiated. A strain value corresponding to a stress of $0.1 f_{cc}$ is used herein.

It is assumed that the rate of damage will increase once the peak compressive strength is attained. As shown in **Figure 4.2**, the damage rate changes beyond ε_{cc} based on the magnitude of D_{cc}. During the process of calibrating the damage model with experimental data, as indicated in Equation 4.11, it was necessary to assign a minimum concrete damage value of 0.3 when the confined core attained its maximum strength. The increase in the rate of damage beyond the strain at peak stress was essential to account for the deterioration in the stress-strain curve.
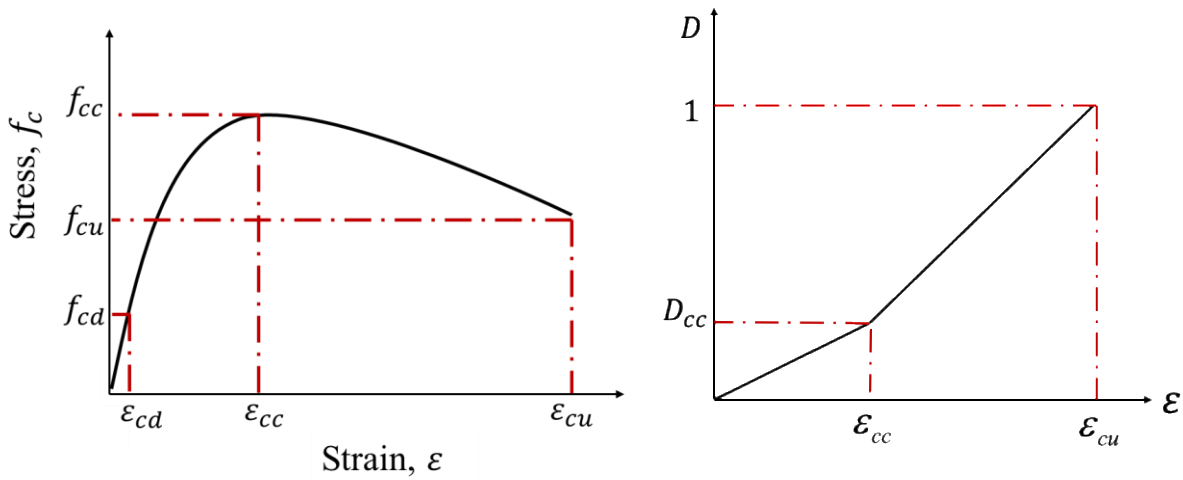
Figure 4.2 Stress-strain response of concrete and corresponding damage progression

4.3   Reinforcing Steel Damage

It is assumed that damage to the reinforcing steel is best captured through a fatigue-based model. The fatigue life of reinforcing steel bars is defined as the number of cycles at specific deformation amplitudes resulting in failure. Miner's (1945) linear damage rule shown in equation 4.12 is used to compute damage in the reinforcing steel fibers:

$$D_{si} = \frac{1}{\sum_{j=1}^{n}(2N_f)_j} \qquad\qquad 4.12$$

D_{si} denotes the damage index in the i_{th} monitored steel fiber and $(2N_f)_j$ denotes the number of half-cycles to failure at the strain amplitude corresponding cycle j as described in Coffin (1954, 1971) and Manson (1953). The fatigue model proposed by Brown and Kunnath (2004), who carried out a comprehensive series of low-cycle fatigue tests on reinforcing bars, is used for finding $(2N_f)_j$. The fatigue life expression used is:

$$\varepsilon_a = 0.112(2N_f)^{-0.433} \qquad 4.13$$

In the above equation, ε_a represents the total strain amplitude.

4.4   Component-Level Damage Index

The damage models described in Sections 4.2 and 4.3 refer to local damage at the sectional level in concrete and accumulated damage in an individual reinforcing bar. As damage progresses from the outer surface to the inner core, it is necessary to develop a procedure to aggregate the total damage to the cross-section. To facilitate the development of a damage model at the cross-sectional level, axial strains are monitored at the integration point within the plastic hinge region at several concrete layers as well as several longitudinal bars. As shown in **Figure 4.3**, three fibers within the confined core (i.e, CR1, CR2 and CR3) deep are monitored. Likewise, the strain in the reinforcing steel is recorded at different locations as shown in the same figure. The selection of these locations are based on extensive calibration (outlined in Chapters 2 and 3) of the damage states reported in experimental testing. The overall section depth in the direction of loading is denoted as **D** and **R** is the half depth of the section (for both circular and rectangular sections). The concrete fibers that are monitored are expressed as a function of the half-depth (**R**), the cover and the bar diameter **d$_b$**. The axial strains in four longitudinal bars (denoted as bars **S1** – **S4**) are also recorded during the analysis.
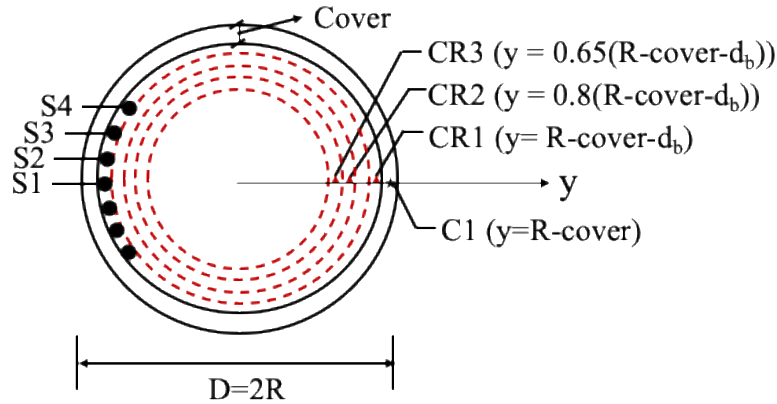
(a) Circular sections
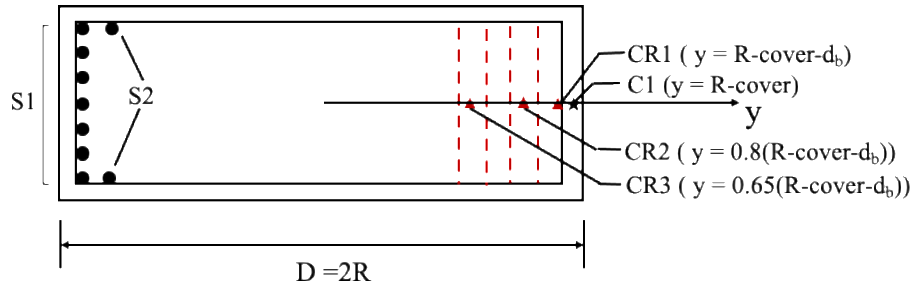
(b) Rectangular sections

Figure 4.3 Concrete fibers and reinforcing bars where strains are monitored

Three concrete fibers and four steel fibers are monitored at the critical section (integration point in plastic hinge location), and the damage index of each fibers, denoted herein as D_{ci} and D_{si} , can be calculated using the approach described in Sections 4.2 and 4.3. The computed damage to each concrete and steel fiber is then combined to compute the column damage index through the use of weighting factors, as follows:

$$w_{ci} = \frac{\alpha_i D_{ci}}{\sum_i^n \alpha_i D_{ci}} \qquad\qquad 4.14$$

$$w_{si} = \frac{\beta_i D_{si}}{\sum_i^m \beta_i D_{si}} \qquad\qquad 4.15$$

$$D_c = \sum_{i}^{n} w_{ci} D_{ci} \qquad\qquad 4.16$$

$$D_s = \sum_{i}^{m} w_{si} D_{si} \qquad\qquad 4.17$$

$$W_s = \frac{D_s}{D_s + D_c} \;, W_c = \frac{D_c}{D_s + D_c} \qquad\qquad 4.18$$

$$DI = W_c D_c + W_s D_s \qquad\qquad 4.19$$

In Equations (4.14) and (4.15), α_i and β_i represents the damage contribution factor of the core concrete steel fibers, respectively. The suggested values for α_i and β_i depend on the fiber location and are shown in **Table 4.1**.

Table 4.1 Suggested values for α_i and β_i

Column damage state	Concrete, α			Steel, β	
	C1	CR2	CR3	S1	S,i
DS-1	1	0	0	0	0
DS-2	0				
DS-3	0				
DS-4	0	1/3	2/3	1/3	2/3
DS-5	0				
DS-6	0				
DS-7	0				

The concept of using local damage indices as weighting factors is not new, however, in the present study the fiber level damage indices are further weighted based on the fiber location. The addition of the damage contribution factors highlights the fact that damage in a fiber that is

74

further from the surface is more critical than damage closer to the surface. These factors were calibrated based on comparing the computed damage with actual reported damage in the four columns considered in the validation study.

4.5 Definition of Damage-Based Capacity Limit States

In Chapter 3, capacity limit states (that classify different damage levels) were defined in terms of ductility. As demonstrated in Section 3.8, the peak ductility attained by a bridge column in an earthquake does not represent the maximum damage state. Accordingly, this research effort shifted focus towards the development of an alternative measure that defined the damaged state of a column more consistently across varying loading histories. While the early damage states up to concrete spalling are generally associated with concrete damage and the maximum sustained strain in a concrete fiber is a reasonable indicator of damage, more severe damage states are associated with damage to the reinforcing steel – this includes bar buckling and bar rupture. In this context, and in particular due to the random cyclic effects of earthquake loading, it was necessary to set up appropriate definitions of bar buckling and rupture so that damage states beyond DS-4 could be predicted with reasonable accuracy.

4.5.1 Longitudinal bar buckling and rupture

Longitudinal bar buckling leads to severe localized stresses and also cause permanent elongation in the transverse steel, which diminishes its effectiveness in confining the concrete core. Section 2.2.2 explains how the "Hysteretic" material in OpenSees is defined in this study. The trilinear envelope on the tension side defines the yield point, the post-yield strain hardening and the post-peak softening whereas on the compression side, buckling is assumed to initiate at

the yield stress and a softening slope is used to capture the effects of buckling until a point is

reached where buckling becomes visible (with possible exposure of the core concrete). The

corresponding stress and strain are denoted by $\sigma_{buckling}$ and $\varepsilon_{buckling}$, as shown in **Figure 4.4**. If

a bar is subjected to compressive loading only, the buckling point is easily established (note that

the buckling model used here is based on the work of Zong et al. discussed in Chapter 2 of this

dissertation). However, under cyclic loading, it is possible that the bar may yield in tension

before compression buckling occurs. Hence it is necessary to shift the origin to the plastic strain

at zero stress (from the origin to location **1** after the first excursion beyond the yield point in

tension and from location **2** to **3** if the yielding progresses to a new maximum tensile strain) as

shown in **Figure 4.4**. The condition to check for buckling becomes $|\varepsilon_i - \varepsilon_A| \geq |\varepsilon_{buckling}|$ and

$\sigma = \sigma_{buckling}$ where ε_i is the strain at the current step and ε_A is the strain at the shifted origin.
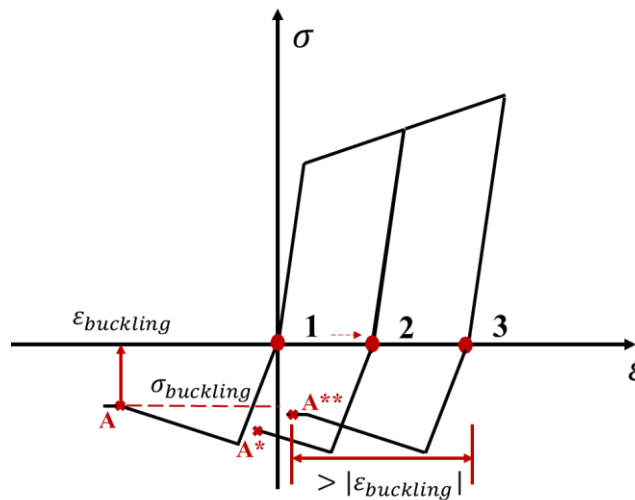
Figure 4.4 Conceptual strain-stress response to identify buckling point

The application of this approach to detecting bar buckling is demonstrated for two cases:

cyclic loading and earthquake loading. In **Figure 4.5**, the stress-strain response of bar S1 in a

circular column is shown for both loading cases. **Figure 4.5 (a)** shows the response for the

bridge column subjected to standard cyclic loading while **Figure 4.5** (b) shows the bar response

76

under seismic loading. In each case, both the complete response for the entire history (left) and the response up to the buckling point (right) is displayed. Two conditions need to be checked – one associated with the strain under compression and the limiting stress that triggers a buckling condition.
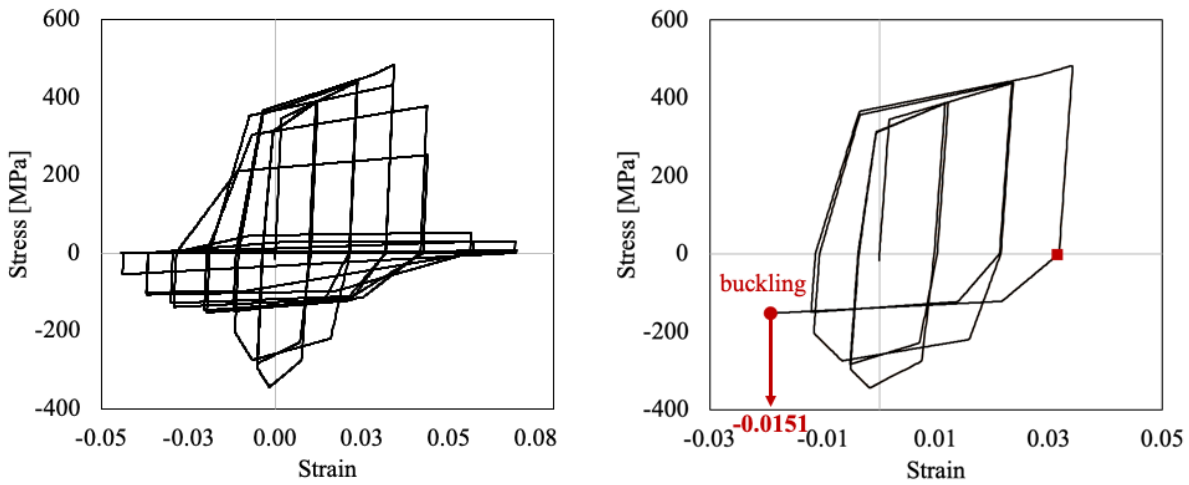
(a)
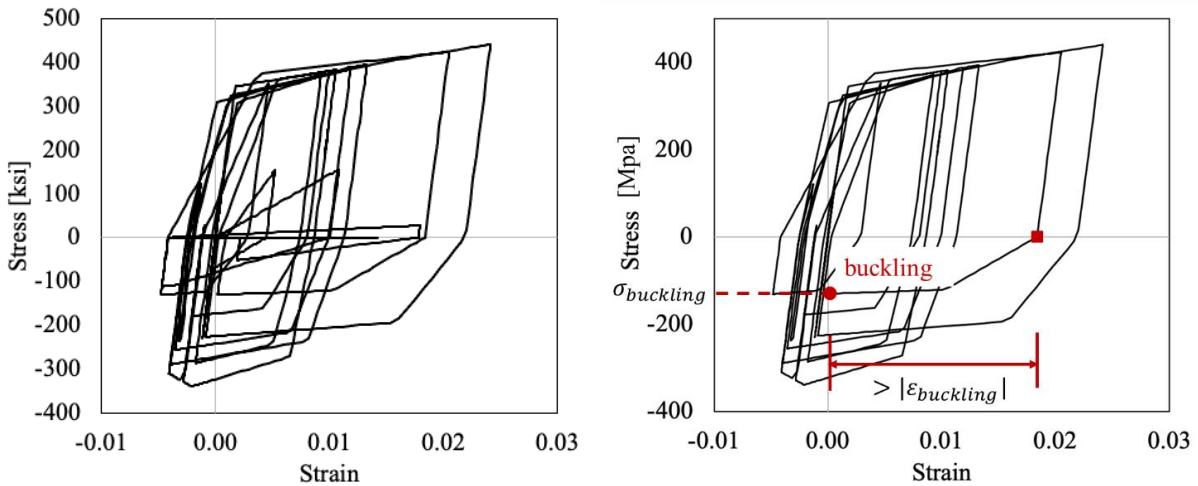
(b)

Figure 4.5 Strain-stress response of bar S1 – complete response history (left) and response up to buckling (right): (a) cyclic loading; (b) earthquake loading

The next critical limit state occurs when one or longitudinal bars rupture. The low-cycle fatigue model presented in Section 4.2. The maximum strain at the end of each half-cycle is recorded and the number of cycles to failure at this strain level is computed using Equation 4.13. Then Equation 4.12 is used to evaluate the cumulative damage after each successive half-cycle. The longitudinal bar is assumed to have ruptured when $D_{si} \geq 1$.

4.6 Damage-Based Limit State Classification

Moving from ductility to a damage-index based definition of capacity limit states, it is necessary to set up a new basis for classifying the different damage limits. As before, axial strains need to be monitored at several concrete fibers and reinforcing bars at the integration point in the plastic hinge region (this is typically the end section of the column at the maximum moment location). In the cover region, the fiber just outside the core concrete (fiber C1) is monitored, and in the core, two fibers denoted as CR1 and CR2 are monitored. Likewise, the strain in the reinforcing steel is recorded at different locations. All monitored points on a typical circular and rectangular cross-section are shown in **Figure 4.6**.
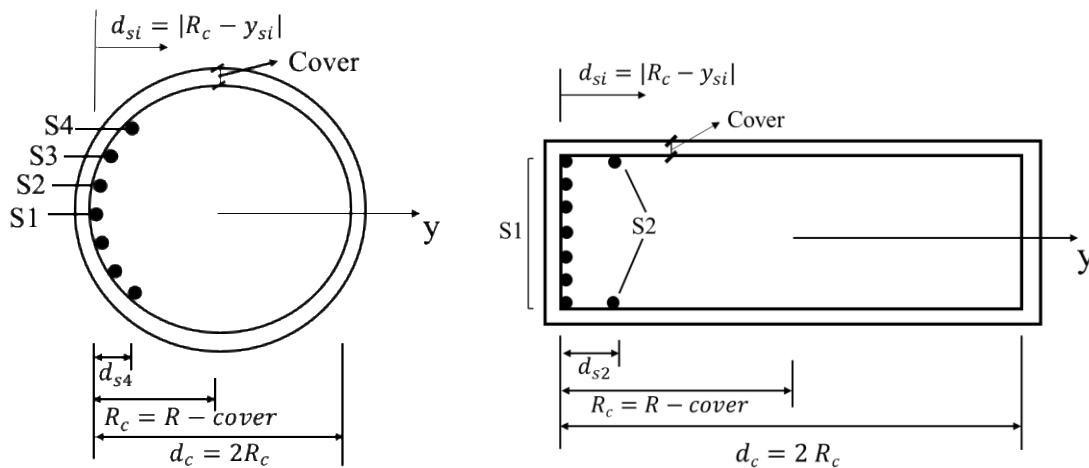
Figure 4.6 Definition of d_{si}

The definition of new limit states based on the concept of using a damage index was developed through calibration with experimental observations. Columns tested under standard cyclic loading as well as a bridge column subjected to seismic loading were utilized in the calibration process. In Schoettler et al. (2015), where the column was subjected to a series of earthquake-induced loading on a shaking table, the limit state corresponding to "exposed core" was observed after bar buckling. Previously, in the ductility-based limit states used in Chapter 3, the limit states corresponding to spalling and exposed core were based on strain states in the concrete. In the new damage index-based limit state classification, the limit state corresponding to an exposed core is constrained to the limit state following bar buckling.

Eventually, the performance of a bridge column was classified into seven damage states with notation and description as specified in **Table 4.2**. With reference to **Figure 4.6** , section C1 corresponds to the layer just outside the core and damage state DS-1 requires the crack to propagate up to but not inside the core. This damage states is relatively minor and will not require structural repairs. In damage state DS-2 and DS-3, layers within the core reach their compressive strength. While state DS-2 can be remedied with epoxy injection alone, state DS-3 may require chipping/removal of damaged sections and concrete replacement. Damage state DS-4 and DS-5 are advanced damage states where the exposed core indicates the need for seismic strengthening. Steel yielding in circular sections will have progressed to multiple bars but there should be no visual evidence of bar buckling. The buckling of longitudinal bars is usually considered an irreparable damage state; hence DS-4 should be perceived as a state where bar buckling has initiated but not distinctly visible in an exposed core. Beyond this state, excessive buckling and rupture of bars is likely and the stability of the bridge column (and the entire bridge depending on the redundancy of the system) is compromised (DS-6). Finally, a collapse state

(DS-7) is defined when the lateral strength reduces to less than 50% of the peak strength. This assumption is reasonable for the considered loading protocol. It will not be uncommon for the final two damage states DS-6 and DS-7 to occur almost simultaneously.

Table 4.2 Description of Damage Limit States

Damage state	Damage description			Damage criteria in critical fiber	
DS-1	*Cracking in cover*	Slight	C1	Tension cracking in fiber C1, $D_{c_{C1}} \geq 0.01$	
DS-2	*Minor Spalling*	Moderate	CR2	$D_{c_{CR2}} \geq D_{cu_{CR2}}$	
DS-3	*Major Spalling*		CR3	$D_{c_{CR3}} \geq D_{cu_{CR3}}$	
DS-4	*Bar buckling*	Extensive	S1	See Section 4.5.1	
DS-5	*Exposed core / first-bar rupture*		S1	$D_{s_{s1}} \geq 1$	
DS-6	*Multi-bar rupture*	Complete	S_i , $d_{si} \geq 0.2R_c$, (See Figure 4.6)	$D_{s_{si}} \geq 1$	
DS-7	*Column collapse*			50% loss in lateral strength in load-displacement response	

4.7   Validation of Proposed Damage-Based Limit States

Two circular Era-1 flexural columns (Chai et. al. 1991 and Ranf et. al, 2006) described in Chapter 2 are selected to verify the proposed damage-index based limit states for columns loaded under standard cyclic histories. The full-scale RC bridge column tested by Schoettler et al. (2015) on a shaking table is used for validation of the methodology under random loading

histories. The process of establishing the damage index for the column for the different damage states identified in **Table 4.2** is accomplished as follows:

1. Develop the simulation model of the bridge column as outlined in Chapter 2 and record the strain-stress response of monitored fibers.

2. Calculate the damage index of each concrete and steel fiber using the procedure described in Sections 4.2 and 4.3 and determine the column damage index using the expressions provided in Section 4.4.

3. Extreme damage states (DS-4 through DS-7) require additional processing to investigate bar buckling and rupture as discussed in Section 4.5.

4. Use the guidelines in **Table 4.2** to classify the different capacity limit states

The computed damage index values for the two flexural columns under cyclic loading is shown in **Table 4.3** for each capacity limit state. With the exception of longitudinal bar buck and final collapse, the damage indices are reasonably consistent for the different damage states.

Table 4.3 Computed damage indices for different limit states for selected columns

Column damage state	Definition	*Ranf et. al*	*Chai et. al*
DS-1	Cracking of cover	0.01	0.03
DS-2	Minor Spalling	0.07	0.07
DS-3	Major Spalling	0.19	0.24
DS-4	Bar buckling	0.40	0.57
DS-5	Exposed core / first-bar rupture	0.72	0.75
DS-6	Multi-bar rupture	1.26	1.03
DS-7	Column collapse	2.05	1.22

In the numerical simulation, DS-4 is closer to the initiation of buckling rather than visible buckling which is typically reported in the literature. Hence some variability in the predicted damage at this limit state is to be expected. Likewise, columns are rarely tested to complete collapse (loss of vertical load carrying capacity). Hence, a damage index greater than 1.0 wherein multiple bars have ruptured is clearly an irreparable damage state requiring replacement of the column.

Next data from the shake-table tests on the full-scale from Schoettler et al. (2015) is used to simulate expected damage under earthquake induced loading. The column was subjected to 10 ground motion records taken from the 1989 Loma Prieta and 1995 Kobe earthquakes at varying intensities as shown in **Table 4.4** to achieve different target displacement ductilities.

Table 4.4 Earthquake ground motions applied in seismic testing of column

Test	Earthquake	Station	Scale factor
EQ1	Loma Prieta	Agnew State Hospital	1.0
EQ2	Loma Prieta	Corralitos	1.0
EQ3	Loma Prieta	LGPC	1.0
EQ4	Loma Prieta	Corralitos	1.0
EQ5	Kobe	Takatori	-0.8
EQ6	Loma Prieta	LGPC	1.0
EQ7	Kobe	Takatori	1.0
EQ8	Kobe	Takatori	-1.2
EQ9	Kobe	Takatori	1.2
EQ10	Kobe	Takatori	1.2

As reported in Schoettler et al., the column remained in elastic phase during test EQ1. Minor inelastic behavior was observed in test EQ2. Test EQ3 was considered a design-level event which resulted in concrete spalling (the extent of visible damage) and the recorded peak strains in the longitudinal bars were less than 0.3%. Test EQ4 represented an aftershock, and resulted in linear response at a reduced stiffness. Test EQ5 represented a beyond-design-level scenario, followed by a repeat of the design-level event in EQ6. Structural integrity was still retained at the end of test EQ6 and the only visible damage was concrete spalling. Test EQ7 triggered bar buckling and generated the largest overturning moment of any test. Additionally, bar fracture along with the onset of concrete core crushing occurred in test EQ7.

In the present validation, tests EQ3, EQ5 and EQ7 are selected given the well-defined observed damage during these tests. The following three simulations were carried out: (1) ground motion time history corresponding to EQ3; (2) ground motion EQ5; and (3) a three-part sequence consisting of EQ3 + EQ5 + EQ7. These are denoted as GM1, GM2, and GM3. Results from the simulations are presented in **Table 4.5**.

Table 4.5 Predicted damage indices for column tested by Schoettler et al. (2015)

Column damage state	Damage description	Computed Damage Index		
		GM1	*GM2*	*GM3*
DS-1	Cracking of cover	0.01	0.01	0.01
DS-2	Minor Spalling	0.02	0.03	0.02
DS-3	Major Spalling		0.11	0.22
DS-4	Bar buckling		0.58	0.53
DS-5	Exposed core			0.97
DS-6	multi-bar rupture			1.76
DS-7	Column collapse	Did not occur		

It can be inferred from the results in **Table 4.5** that the overall simulated results are in general agreement with experimental observation with the exception of damage state DS-2. This can be attributed to the fact that in the simulation loading case GM2 consisted of only EQ5 without the effects of damage caused by EQ3. As in the case of the experiment, GM1 (or EQ3) only resulted in cover cracking and minor spalling. The simulation indicates that GM2 (or EQ5) resulted in the initiation of bar buckling. While this was not reported in the testing, the strains experienced by some of the longitudinal bars suggest that buckling is likely to have initiated but the core was still intact for buckling to be visible. Finally, with GM3 (test EQ7 along with the effects of EQ3 and EQ5), a damage state corresponding to an exposed core along with the rupture of multiple bars was captured in the simulation.

4.8   Application to Era-1 Caltrans Bridge Columns

4.8.1   Cyclic loading

The damage-based limit states will now be evaluated for the seven circular columns and five wide-section columns analyzed in Chapter 3. Recall that these column configurations were developed following an assessment of cross-section and reinforcement details of typical non-ductile columns (representing Era-1). The evaluation presented in Chapter 3 concluded that the loading protocol (a single cycle versus two or three cycles per displacement amplitude) did not have a significant influence in the early limit states and had a minor effect at higher capacity limit states. Rather than carry out simulations for all three loading protocols, it was decided to apply two cycles per displacement amplitude in this phase of the study. Additionally, only a single ductility-based damage parameter was used, i.e. $damage1 in the Hysteretic material model in OpenSees was set to 0.02 (note that three values – 0.01, 0.02 and 0.03 of this parameter

was used in the simulations presented in Chapter 3). The resulting damage indices for the

different damage limit states are summarized in **Table 4.6** and **Table 4.7** for circular and wide

rectangular sections, respectively.

The effectiveness of the damage-based limit states is clearly evident for both circular and

wide-section columns. The damage indices for each damage state, with the exception of the

collapse state, is nearly identical for all seven circular columns and all five wide rectangular

section columns indicating that the proposed damage index-based approach to defining capacity

limit states overcomes the drawbacks of a ductility-based measure.

Table 4.6 Evolution of damage index for circular columns under cyclic loading

Column damage state	Damage description	Specimen #						
		#1	#2	#3	#4	#5	#6	#7
DS-1	Cracking of cover	0.01	0.01	0.03	0.08	0.03	0.04	0.04
DS-2	Minor Spalling	0.22	0.26	0.24	0.24	0.22	0.22	0.24
DS-3	Major Spalling	0.31	0.27	0.30	0.30	0.30	0.26	0.27
DS-4	Bar buckling	0.51	0.37	0.39	0.42	0.54	0.58	0.58
DS-5	Exposed core / first-bar rupture	0.70	0.74	0.77	0.76	0.74	0.72	0.71
DS-6	multi-bar rupture	1.05	0.99	1.08	1.08	1.15	1.32	0.98
DS-7	column collapse	1.92	1.10	1.32	1.47	1.69	1.40	1.19

Table 4.7 Evolution of damage index for wide-section columns

Column damage state	Damage description	Specimen #				
		#1	#2	#3	#4	#5
DS-1	Cracking of cover	0.05	0.05	0.04	0.03	0.07
DS-2	Minor Spalling	0.18	0.25	0.21	0.29	0.25
DS-3	Major Spalling	0.32	0.31	0.40	0.32	0.30
DS-4	Bar buckling	0.33	0.43	0.58	0.57	0.71
DS-5	Exposed core / first-bar rupture	0.82	0.65	0.66	0.67	0.83
DS-6	multi-bar rupture	1.18	1.15	1.12	1.00	1.15
DS-7	column collapse	1.30	1.33	1.38	1.29	1.27

4.8.2　Earthquake loading

Finally, the proposed damage-based measure is applied to the same set of columns (circular and wide rectangular sections) subjected to a series of earthquake loads. The goal here is to consider random loading histories. Ten ground motions were extracted from the PEER Strong Motion database (https://ngawest2.berkeley.edu/). Pertinent details of the selected ground motions are shown in **Table 4.8**. Only a typical circular and a typical wide-section rectangular column is used in this phase of the study since it has already been demonstrated that the predicted damage indices are reasonably consistent across all columns (both circular and rectangular) evaluated in

the previous section. Column #3 from the circular sections and column #1 from the rectangular

sections was selected for the seismic simulations.

Table 4.8 Ground motion details

RSN	Earthquake	Year	Station Name	Mag.	R_{jb} (km)	Vs_{30} (m/sec)
334	Coalinga-01	1983	Parkfield - Fault Zone 1	6.36	41.0	178
337	Coalinga-01	1983	Parkfield - Fault Zone 12	6.36	28.0	265
341	Coalinga-01	1983	Parkfield - Fault Zone 2	6.36	37.9	294
369	Coalinga-01	1983	Slack Canyon	6.36	26.0	648
727	Superstition Hills-02	1987	Superstition Mountain	6.54	5.6	362
902	Big Bear-01	1992	Desert Hot Springs	6.46	39.5	359
995	Northridge-01	1994	LA - Hollywood Storage	6.69	19.7	316
1300	Chi-Chi (Taiwan)	1999	HWA055	7.62	43.0	370
1547	Chi-Chi (Taiwan)	1999	TCU123	7.62	14.9	270
4857	Chuetsu-Oki (Japan)	2007	Kamo Kouiti Town	6.80	29.2	366

Each ground motion was scaled successively until the column attained a damage state of

DS-6 or DS-7. In the case of rectangular columns, two ground motions required unrealistic scale

factors to reach DS-6 and were discarded. Additionally, none of the columns reached a

"collapse" condition as defined in **Table 4.2**. It is worth noting that identifying a 50% loss in

lateral strength is a challenging exercise under earthquake loading since it is necessary to

establish that the peak recorded strength in each cycle should be part of an inelastic excursion

and not during unloading and reloading on a linear path. Eventually, six damage states (DS-1

through DS-6) were established for all 10 ground motions for circular columns and for 8 ground

motions for the wide-section rectangular columns. The scale factors and maximum interstory

drift ratio (MIDR) for each simulation are shown in **Table 4.9**.

Table 4.9 Scale factors and MIDR for each GM

RSN	Circular section		Wide section	
	Scale Factor	*MIDR*	*Scale Factor*	*MIDR*
334	6.2	0.046	6.8	0.045
337	8.9	0.054	9.8	0.042
341	6.5	0.060	6.5	0.040
369	11.5	0.048	12.6	0.041
727	7.5	0.046	7.5	0.040
902	16.2	0.047		
995	9.5	0.041	10.5	0.040
1300	6.6	0.045	7.5	0.050
1547	4.3	0.049	4.8	0.040
4857	24.0	0.043		

The maximum drift for circular columns varies from a low of 4.1% to a high of 6.0%

with a mean value of 4.8%. However, despite the ground motion variability, the damage index

for a particular limit state is remarkably consistent. For rectangular columns ground motion

variability is less pronounced with a computed minimum of 4%, a maximum of 5% and a mean

of 4.2%. The evolution of the damage indices as the ground motions are scaled are reported in

Table 4.10 and **Table 4.11** for circular and rectangular columns, respectively. It is evident that

the resulting damage index for each limit state is fairly consistent across all ground motion

records thereby validating the proposed damage-based methodology for establishing capacity

limit states for non-ductile bridge columns that are representative of Era-1 columns.

Table 4.10 Evolution of damage indices for circular columns under seismic loading

Column damage state	Damage description	Record Sequence Number (RSN)									
		337	*369*	*902*	*1300*	*1547*	*4857*	*334*	*341*	*995*	*727*
DS-1	Cracking of cover	0.05	0.05	0.02	0.07	0.05	0.05	0.05	0.08	0.07	0.05
DS-2	Minor Spalling	0.19	0.22	0.2	0.27	0.22	0.25	0.25	0.26	0.27	0.23
DS-3	Major Spalling	0.35	0.32	0.29	0.28	0.27	0.26	0.30	0.27	0.28	0.33
DS-4	Bar buckling	0.39	0.51	0.44	0.30	0.36	0.56	0.61	0.55	0.30	0.45
DS-5	Exposed core/first bar rupture	0.83	0.88	0.83	0.75	0.77	0.81	0.77	0.87	0.84	0.82
DS-6	Multi-bar rupture	1.04	1.05	1.12	0.99	1.10	1.13	1.11	1.13	1.13	1.10

Table 4.11 Evolution of damage indices for wide-section rectangular columns

Column damage state	Damage description	Record Sequence Number (RSN)							
		337	*369*	*1300*	*1547*	*334*	*341*	*995*	*727*
DS-1	Cracking of cover	0.08	0.06	0.04	0.05	0.06	0.05	0.04	0.04
DS-2	Minor Spalling	0.20	0.23	0.23	0.19	0.15	0.17	0.12	0.18
DS-3	Major Spalling	0.39	0.25	0.29	0.26	0.24	0.30	0.32	0.21
DS-4	Bar buckling	0.68	0.46	0.38	0.33	0.52	0.63	0.33	0.23
DS-5	Exposed core/first bar rupture	0.90	0.85	0.83	0.65	0.81	0.83	0.76	0.78
DS-6	multi-bar rupture	1.12	1.11	1.22	1.14	1.15	1.18	1.11	1.17

Table 4.12 and **Table 4.13** compares the mean damage index for the various limit states between cyclic loading and earthquake loading for circular columns and wide-section rectangular columns,

respectively. The results show that the damage index for a damage state is not dependent on the loading history, another feature of the proposed damage modeling scheme that lends itself to the research objective.

Table 4.12 Comparison of mean damage index between cyclic and earthquake loading for circular columns

Column damage state	Damage description	Mean Damage Index	
		Cyclic loading	Earthquake loading
DS-1	Cracking of cover	0.03	0.05
DS-2	Minor Spalling	0.23	0.24
DS-3	Major Spalling	0.29	0.30
DS-4	Bar buckling	0.48	0.45
DS-5	Exposed core/first bar rupture	0.73	0.82
DS-6	Multi-bar rupture	1.09	1.09

Table 4.13 Comparison of mean damage index between cyclic loading and earthquake loading for wide rectangular section columns

Column damage state	Damage description	Mean Damage Index	
		Cyclic loading	Earthquake loading
DS-1	Cracking of cover	0.05	0.05
DS-2	Minor Spalling	0.24	0.19
DS-3	Major Spalling	0.33	0.28
DS-4	Bar buckling	0.53	0.47
DS-5	Exposed core/first bar rupture	0.72	0.80
DS-6	Multi-bar rupture	1.12	1.15

4.9   Summary

In this chapter, a damage-based methodology is proposed to quantify capacity limit states for bridge columns. The motivation for the development stems from the inability of ductility-based limit states to deal with non-symmetric and random loading histories. Damage is defined at the material level based on the cross-sectional strain across the depth of the member – the monotonic stress-strain curve is used for concrete whereas yielding, buckling and low-cycle fatigue incorporating cyclic effects is considered to establish damage to the reinforcing steel. The proposed approach was validated for both cyclic and seismic loading histories by comparing computed damage indices and their corresponding damage states with experimental observations. Finally, a series of simulations comprising both cyclic and earthquake loading histories of Era-1 circular and rectangular columns, previously evaluated in Chapter 3 using ductility-based measures, was carried out to establish median damage indices for each of the six damage states (DS-1 through DS-6).

It was shown that the predicted damage indices for the different damage states were consistent and largely independent of both cross-section shape and loading history. This is further demonstrated in the fragility plots shown in **Figure 4.7**. With the exception of DS-4, very little dispersion is observed in the predicted indices. Using the median estimates and the observed dispersions, a damage index range is proposed for each capacity limit state as displayed in **Table 4.14**. The distinction between minor and major spalling is not always well defined in the literature on experimental testing. This explains the larger dispersion for DS-4. Likewise, tests report bar buckling when it is visible, and the core is likely exposed. DS-5 in the present study was assigned to the onset of buckling. However, the damage index range for this state was increased to account for visible bar buckling.
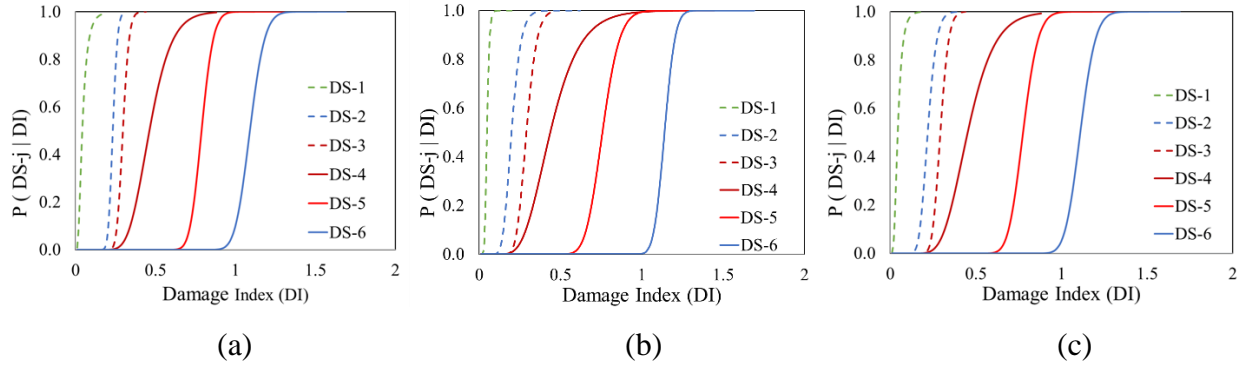
Figure 4.7 Distribution and dispersion of damage limit states: (a) Circular columns; (b) Wide section rectangular columns; (c) Both circular and wide-section columns

Table 4.14 Proposed damage index range for each limit state

Damage state	Damage description		Damage Index
DS-1	Cracking of cover	Slight	< 0.1
DS-2	Minor Spalling	Moderate	0.10 – 0.20
DS-3	Major Spalling		0.20 – 0.35
DS-4	Bar buckling	Extensive	0.35 – 0.65
DS-5	Exposed core / first-bar rupture		0.65 – 0.80
DS-6	Multi-bar rupture	Complete	0.80 – 1.00
DS-7	Column collapse		> 1.0

In summary, the proposed damage index provided reasonably consistent values for each limit state irrespective of the loading history. The methodology was successful in predicting the different damage states, including cracking of the cover concrete, spalling of concrete, bar buckling, crushing of the core concrete and multi-bar rupture. It offers a non-dimensional approach to classifying limit states and has the potential to enhance post-earthquake damage assessment.

CHAPTER 5.0   DAMAGE-BASED SEISMIC ASSESSMENT OF MULTI-COLUMN BENTS

In this chapter, the damage-based assessment is applied to multi-column bents. As indicated in the introduction, the purpose of including analyses of multi-column bents is to assess the benefits of redundancy in limiting the damage experienced by non-ductile bridge systems. Since the prediction of damage states themselves will not highlight this difference, a different approach is used in this chapter to assess the performance of multi-column bents relative to single-column bents. The damage limit states of an individual column in a multi-column bent will be similar to those for single column bents presented in Chapter 4. Weighting factors need to be introduced to assess overall damage in a bridge with multi-column bents.

In order to compare the performance of multi-column versus single-column bents, the seismic intensity required to cause different damage limit states in single and multi-column bents will be investigated. More specifically, fragility functions, typically expressed as a function of a selected ground motion intensity measure (IM) will be used as a tool to quantify the likelihood of each damage state during an earthquake. The process of developing the comparative fragility functions will be accomplished as follows:

1) Validation of the modeling methodology – Earlier, the modeling approach discussed in Chapter 2 was validated for single columns. It was considered prudent to validate the overall modeling approach using test data for a multi-column bent.

2) Nonlinear evaluation method – An appropriate methodology is needed to enable comparison of the seismic performance of different bridge bents. One of methods used in the literature is to impose seismic loads of increasing intensity until global dynamic

instability is observed. Incremental Dynamic Analysis (IDA), a concept introduced originally by Bertero (1980), who suggested scaling the seismic intensity to determine system capacity, but was enhanced and formalized by Vamvatsikos and Cornell (2002) was selected as an appropriate means to accomplish the objective of this phase of the study. The proxy for each performance state will be the proposed damage index.

3) Ground motion selection – Suites of existing earthquake records need to be selected from the database based on specific criteria. The records are selected from PEER Next Generation Attenuation (NGA) Project Ground motion library.

4) Fragility function fitting – A mathematical post-processing procedure is utilized for fitting the response data into a CDF function or fragility curve.

Fragility functions are typically predicated on a ground motion IM, such as peak ground acceleration (PGA) or spectral acceleration at a given period. As discussed in Luco and Cornell (2007), the selection of an appropriate IM is driven by its "efficiency" and "sufficiency," both of which are characteristics tied to the accuracy of probabilistic seismic demand prediction. An efficient IM should result in a relatively small variability of the structural demand measure given IM, and a sufficient IM should render the selected demand measure to be conditionally independent of earthquake magnitude and source-to-site distance. Of the many possible choices for IM, $S_a(T_1)$ has been shown to meet the criteria of efficiency and sufficiency for first-mode dominated buildings (Shome et al. 1998). Enhanced intensity measures would be needed for long-span bridges where higher modes contribute significantly to the system response.

The conceptual IDA curve using damage index is shown in **Figure 5.1**. The highlighted points in conceptual curve contains damage represent different damage states.
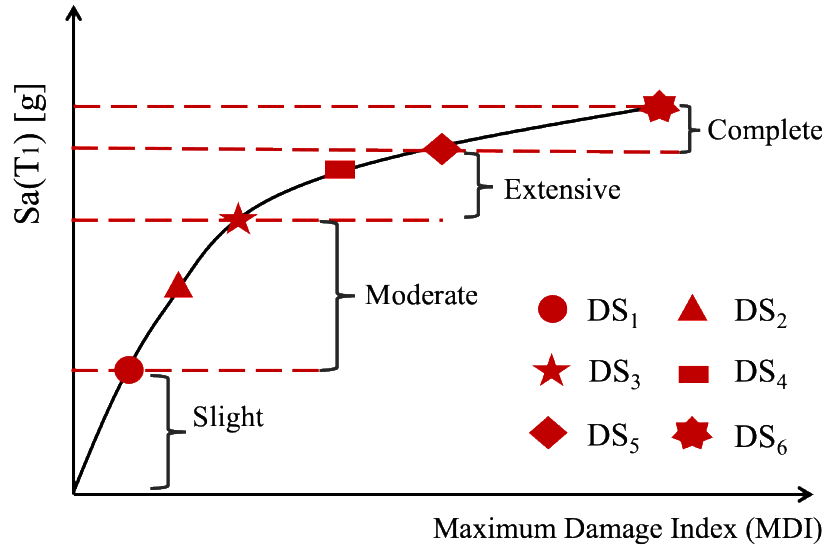
Figure 5.1 Conceptual IDA curve using damage-based indices

5.1 Validation of multi-column bent model

Prior to conducting numerical simulations of multi-column bents, it was decided that the modeling scheme outlined in Chapter 2 should be further validated using experimental data for a multi-column bent. A review of the literature resulted in the selection of specimen RH-NS-T tested by Kim et al. (2021) that best conformed to the reinforcement details of a Caltrans Era-1 bridge. The primary sectional data for specimen RH-NS-T is listed in Table 5.1. An elevation and typical column cross-section is shown in Figure 5.2. Complete details of the specimen configuration and material properties can be found in Kim et al. (2021).

Table 5.1 Specimen details (Kim et al., 2021)

Dia. (m)	Height (m)	Trans. reinforcement	Trans. steel ratio	Long. reinforcement	Long. steel ratio
0.5	3	Ø 4 mm @ 37.5 mm	0.0027	30 Ø 10 mm	0.012%
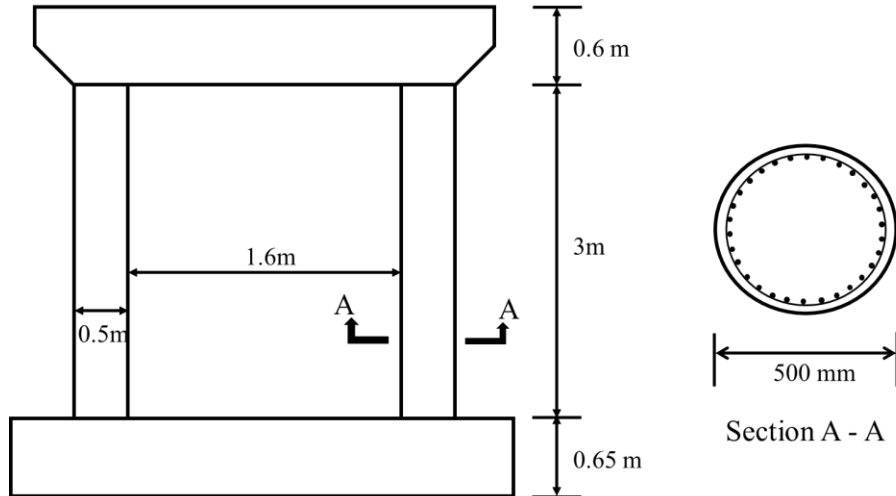
Figure 5.2 Elevation and column cross-section of specimen RH-NS-T (Kim et al. 2021)

As outlined in Chapter 2, each bridge column was modeled as a nonlinear beam-column element in OpenSees with 4 integration points. The cap beam, which is designed to remain undamaged in a seismic event, was modeled using an elastic element (elasticBeamColumn object in OpenSees). The cyclic loading pattern applied on the specimen was also imposed on the OpenSees model and the numerically simulated response is compared to the experimental results in **Figure 5.3**.
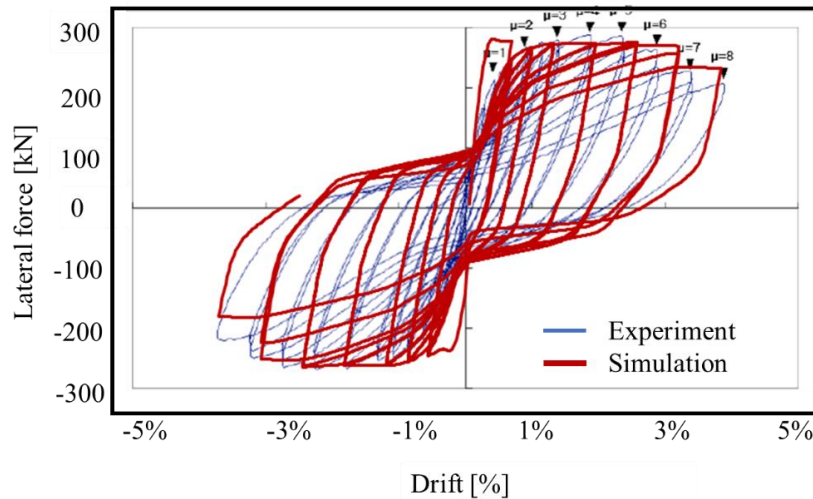
Figure 5.3 Comparison of experimental and simulated response

Kim et al. (2021) report minor damage, such as cracking and the onset of spalling, up to a ductility of 4.0. The numerical simulation estimates a damage index of 0.2 at a ductility of 4.0. At a ductility of 5.0, excessive spalling was observed in the experiment as well as the initiation of bar buckling. The first bar rupture was reported at a ductility of 6.0 followed by multi-bar rupture at a ductility of 8.0. The computed damage indices during the simulation for the different limit states are shown in **Table 5.2** – major concrete spalling was predicted when the ductility reached 5.0, bar buckling and the first bar rupture occurred between $6.0\Delta_y$ to $7.0\Delta_y$ and the next bar rupture and the attainment of damage state DS-6 was recorded at $8.0\Delta_y$. In general, the predicted damage is in good agreement with test observations.

Table 5.2 Damage evolution in specimen RH-NS-T

Column damage state	DS-1	DS-2	DS-3	DS-4	DS-5	DS-6
Damage state	*Cracking of cover*	*Minor Spalling*	*Major Spalling*	*Bar buckling*	*Exposed core /first bar rupture*	*Multi-bar rupture*
Damage Index	0.04	0.20	0.35	0.48	0.67	1.07
Ductility	2.0	4.0	5.0	6.0	6.0 – 7.0	8.0

5.2   Bent Selection

In order to establish a basis for comparing the performance of single and multi-column bents, it was necessary to carefully select the different configurations that would represent bridge systems that were typical of Era-1 construction. The inventory of pre-1971 Caltrans bridges were

reviewed and a target bridge system was identified. Salient features of the target multi-column bent is shown in Figure 5.4.
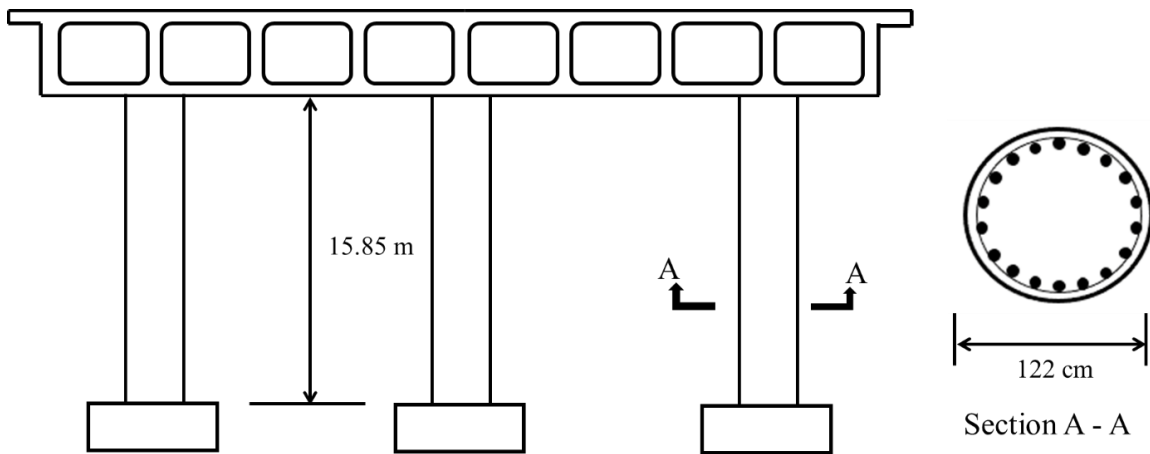
Figure 5.4 Typical pre-1971 overcrossing with three-column bent

Each column has a height to depth ratio of approximately 13.0 (or a shear-span ratio of 6.5) suggesting a primarily flexural response. The column section is reinforced with 18 – 35 mm bars (#11 bars) resulting in a longitudinal reinforcement ratio of 1.9% and consists of 16 mm (#5 bars) diameter hoops spaced at 140 mm for a total transverse reinforcement ratio of 0.5%. The representative 3-column bent was subjected to a monotonically increasing lateral load at the deck level to generate a pushover curve of the system. The pushover response, shown in Figure 5.5, can be regarded as the base model from which the other bents need to be constructed. Initially, models of a 2-column and a 3-column bent was developed in OpenSees assuming the same column cross-section for all cases. Pushover analyses of these bents, shown in Figure 5.6 (a), indicates that the lateral strength varies significantly, making any comparison between their responses inconsistent. In a typical design scenario, the design of a bridge column is dictated by site conditions and proximity to causative faults. Consequently, it is reasonable to assume that for a given site, the design base shear for a bridge system will be constant resulting in identical

lateral strength for a system irrespective of whether the bridge has a single or multi-column bent. Hence, the column sections were re-designed for the single and 2-column bents such that their lateral load capacities were similar, as shown in Figure 5.6 (b).
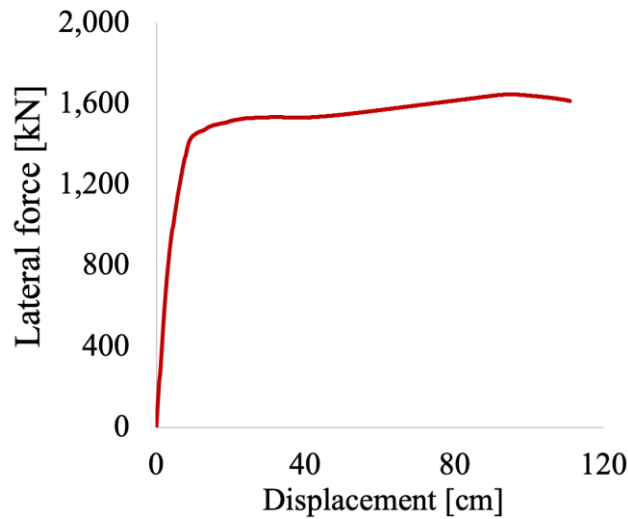
Figure 5.5 Pushover curve of the 3-column bent

(a)

(b)
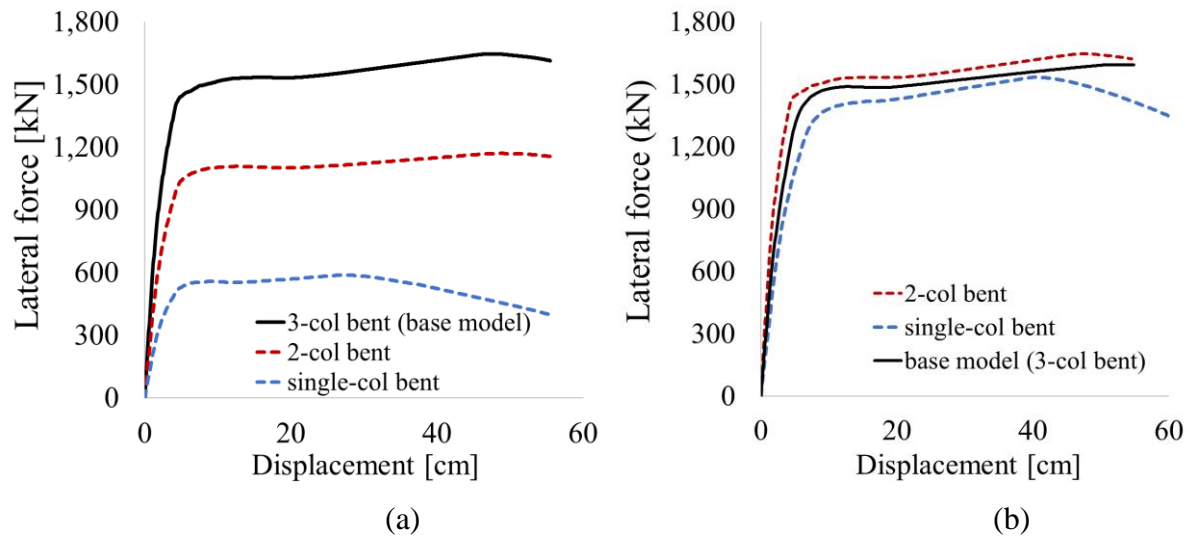
Figure 5.6 Pushover curves for all three bents:

(a) identical columns; (b) equal lateral strength

Table 5.3 lists the basic section and reinforcement details of the three different bents considered in this final phase of the study.

Table 5.3 Bent properties to achieve equal lateral strength

Bent type	1 Col	2 Col	3 Col
Diameter (in)	72	48	48
H/D	6.5	6.5	6.5
Height (ft.)	39	52	52
Trans. reinf.	#6	#5	#5
Spacing (in)	5	5.5	5.5
Trans. steel ratio	0.53%	0.51%	0.51%
Long. Reinf.	46 # 11	28 # 11	18 # 11
Long. steel ratio	2.0%	3.0%	1.9%

5.3 Ground motion selection

Ground motions for this phase of the study are taken from FEMA P-695 (FEMA 2009). These records were generated from large-magnitude (M > 6.5) events. Record sets include ground motions from earthquakes with either strike-slip or reverse (thrust) sources and on either soft rock (Site Class C) or stiff soil (Site Class D) sites. As noted in FEMA P-695, these sources are typical of shallow crustal earthquakes in California. In all, twenty-eight records are taken from 14 events that occurred between 1976 and 2002. Event magnitudes range from magnitude 6.5 to 7.9 with an average magnitude of 7.0. Pertinent details on the FEMA P-695 ground motions are listed in Table 5.4. Two components in horizontal direction have been included in this set, in total, 28 pulse-like and 28 non pulse-like ground motions are considered in this set. **Figure 5.7** shows the spectra of the individual records and the mean spectrum of the selected records are also superimposed in the same figure.

Table 5.4 Basic information on FEMA P-695 recommended ground motions

ID #	Earthquake			Recording Station	
	M	Year	Name	Name	Source
Pulse Records					
1	6.5	1979	Imperial Valley-06	El Centro Array #6	CDMG
2	6.5	1979	Imperial Valley-06	El Centro Array #7	USGS
3	6.9	1980	Irpinia, Italy-01	Sturno	ENEL
4	6.5	1987	Superstition Hills-02	Parachute Test Site	USGS
5	6.9	1989	Loma Prieta	Saratoga - Aloha	CDMG
6	6.7	1992	Erzican, Turkey	Erzincan	--
7	7	1992	Cape Mendocino	Petrolia	CDMG
8	7.3	1992	Landers	Lucerne	SCE
9	6.7	1994	Northridge-01	Rinaldi Receiving Sta	DWP
10	6.7	1994	Northridge-01	Sylmar - Olive View	CDMG
11	7.5	1999	Kocaeli, Turkey	Izmit	ERD
12	7.6	1999	Chi-Chi, Taiwan	TCU065	CWB
13	7.6	1999	Chi-Chi, Taiwan	TCU102	CWB
14	7.1	1999	Duzce, Turkey	Duzce	ERD
Non-Pulse Records					
15	6.8	6.8	Gazli, USSR	Karakyr	--
16	6.5	1979	Imperial Valley-06	Bonds Corner	USGS
17	6.5	1979	Imperial Valley-06	Chihuahua	UNAMUCSD
18	6.8	1985	Nahanni, Canada	Site 1	--
19	6.8	1985	Nahanni, Canada	Site 2	--
20	6.9	1989	Loma Prieta	BRAN	UCSC
21	6.9	1989	Loma Prieta	Corralitos	CDMG
22	7	1992	Cape Mendocino	Cape Mendocino	CDMG
23	6.7	1994	Northridge-01	LA - Sepulveda VA	USGS/VA
24	6.7	1994	Northridge-01	Northridge - Saticoy	USC
25	7.5	1999	Kocaeli, Turkey	Yarimca	KOERI
26	7.6	1999	Chi-Chi, Taiwan	TCU067	CWB
27	7.6	1999	Chi-Chi, Taiwan	TCU084	CWB
28	7.9	2002	Denali, Alaska	TAPS Pump Sta. #10	CWB

5.4   Nonlinear seismic simulations

Nonlinear simulations using OpenSees were carried out on the single-column, two-column and three-column bent. In a typical IDA study, collapse is defined as the point of dynamic instability, where the lateral story drifts of the building increase without bounds. This typically occurs when the IDA curve becomes nearly flat.

(a)   (b)
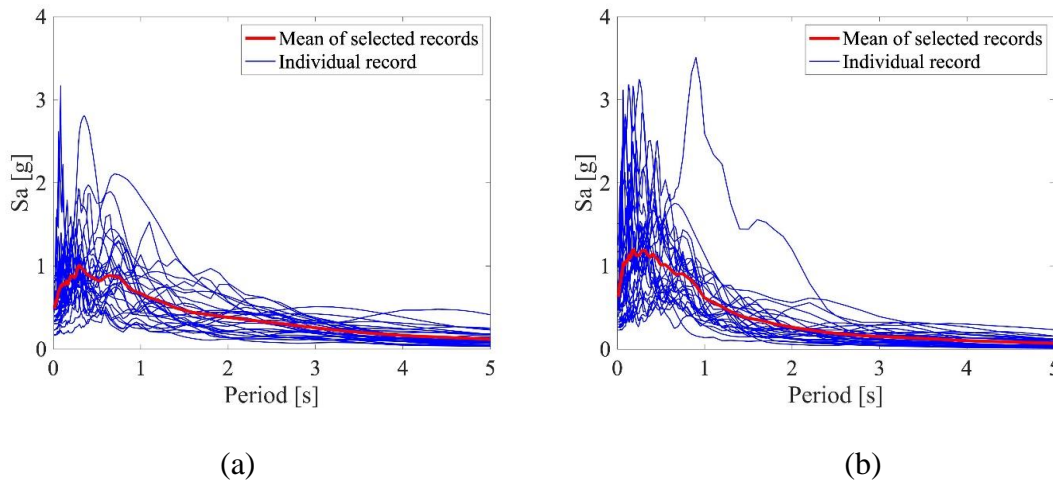
Figure 5.7 Response spectra of selected ground motions:
(a) pulse-like records; (b) non-pulse records

However, in the present study, the collapse condition is defined when the maximum damage index (MDI) reaches or exceeds 1.0. Seismic simulations are carried out at increasing intensities until the MDI exceeds 1.0, and not the so-called flat-lining that is the norm in an IDA-based assessment. Simulations were performed using the suite of 28 earthquake data sets – each comprising 2 components. Hence there were 28 simulations each for the pulse-like and non-pulse records. The resulting IDA curves for each of bents (single-column, 2-column and 3-column) are plotted in Figures 5.8 – 5.10. While some IDA curves terminated at higher damage indices, the plots are truncated at a maximum damage index (MDI) of 1.0. It is important to note that the damage index for multi-column bents required the combination of damage to the individual

columns – this was accomplished using the damage index of the column as the weighting factor, similar to the process of combining concrete and reinforcement damage described in Chapter 4.

(a)   (b)
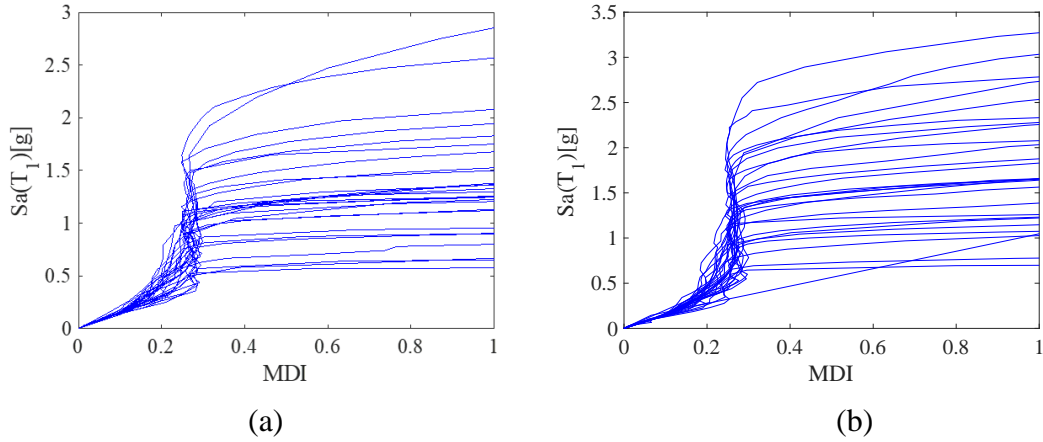
Figure 5.8 IDA curves for single-column bents: (a) pulse-like & (b) non-pulse motions

(a)   (b)
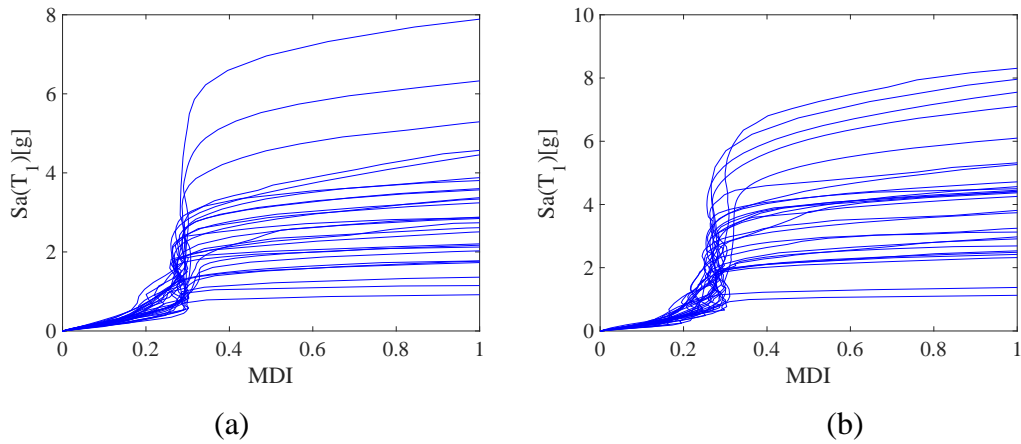
Figure 5.9 IDA curves for two-column bents: (a) pulse-like & (b) non-pulse motions

(a)   (b)
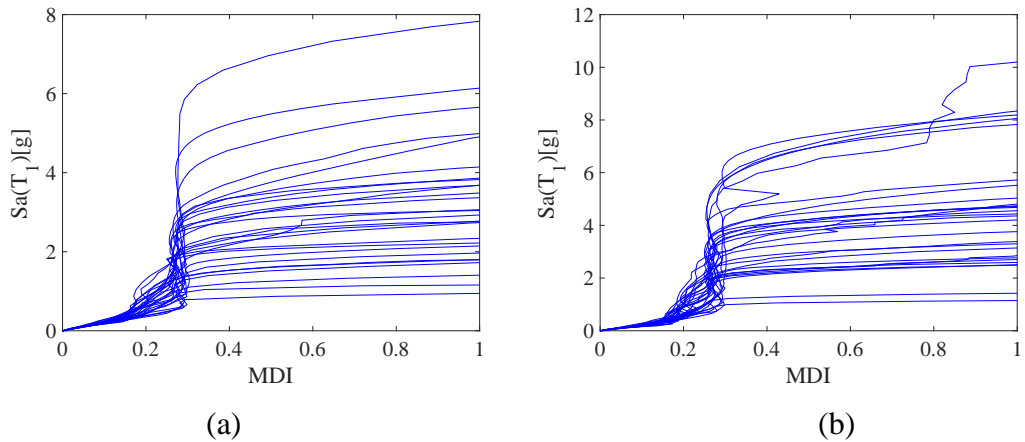
Figure 5.10 IDA curves for three-column bents: (a) pulse-like & (b) non-pulse motions

5.5 Damage-Based Fragility Curves

To compare the performance of multi-column bents to single-column bents, fragility functions were developed from the seismic simulations of the bents subjected to 28 pulse-like and 28 non-pulse motions. To develop the fragility curves, a lognormal distribution function was used since it is well-acknowledged that a log-normal distribution, which is characterized by the median and standard deviation of the natural logarithm of the intensity measures (IMs), yields the best representation of the distribution of seismic demands in the framework of performance-based seismic assessment of structures (Shome and Cornell 1999, Ibarra and Krawinkler 2011, among others). It should also be noted that in general, seismic demands are highly record dependent. This record-to-record (RTR) variability is usually accounted for if the fragility function is developed from a reasonably large set of records. Previous studies that have been cited in this dissertation suggest that approximately 30 ground motions to be adequate to incorporate RTR variability. Matching the mean of the spectral shapes of the selected records to the design spectrum also aids in minimizing the effects of RTR variability (Iervolino et al. 2008). The selected ground motions from the FEMA P-695 project do account for spectral shape and hence the dispersion of the IM of the selected records is implicitly incorporated into the statistical fitting of the observed data.

Seismic demands, in the present study, are expressed in terms of a damage index, which in turn is correlated to a specific damage state (see Chapter 4). The lognormal cumulative distribution function used to develop the fragility functions presented in this research can be expressed as:

$$P(DS_i|IM = x) = \Phi\left(\frac{ln(^x/_\theta)}{\beta}\right) \qquad 5.1$$

where $P(DS_i|IM = x)$ is the probability of each damage state of the structure under the ground motion with $IM = x$, $\Phi(x)$ is the standard normal cumulative distribution function, θ is the

median of the fragility function (i.e. the IM magnitude that corresponds to 50% probability of attaining that damage state) and β is the standard deviation of $\ln(IM)$.

Figure 5.11 represents the log-normal fitted fragility function from damage states DS-1 to DS-6. These functions were developed from the entire data set – comprising both pulse-like and non-pulse motions. Later, the distinction between pulse and non-pulse motions are highlighted. At the first damage state which corresponds to cracking in the cover, it is obvious that multi-column bents will experience this limit state at higher seismic intensities. The median intensity for the 3-column bent is higher than both the 2-column and single-column bents, however, when approaching higher exceedance probabilities, there is not much difference between two and three-column bents. For minor spalling (damage state DS-2), the probability of exceedance is always lowest for the 3-column bent, followed by the 2-column bent, across the entire range of seismic intensity levels. When examining higher damage limit states (DS-3 through DS-6), multi-column bents clearly exhibit a lower exceedance probability for the full range of seismic intensities though both two and three column bents have nearly identical performance. Hence it can be concluded that though redundancy can assist in limiting damage for a particular seismic intensity level, the gain in performance of a 3-column bent over a 2-column bent is negligible for moderate to severe damage states.

Next, the effect of pulse-like motions is investigated by comparing the performance of the three bent types for an extreme damage limit state (DS-6). As seen in **Figure 5.12**, pulse-like motions are significantly more damaging that non-pulse motions for all three bent types highlighting the need to consider the potential for pulse-like motions from the nearest causative fault from the bridge site.
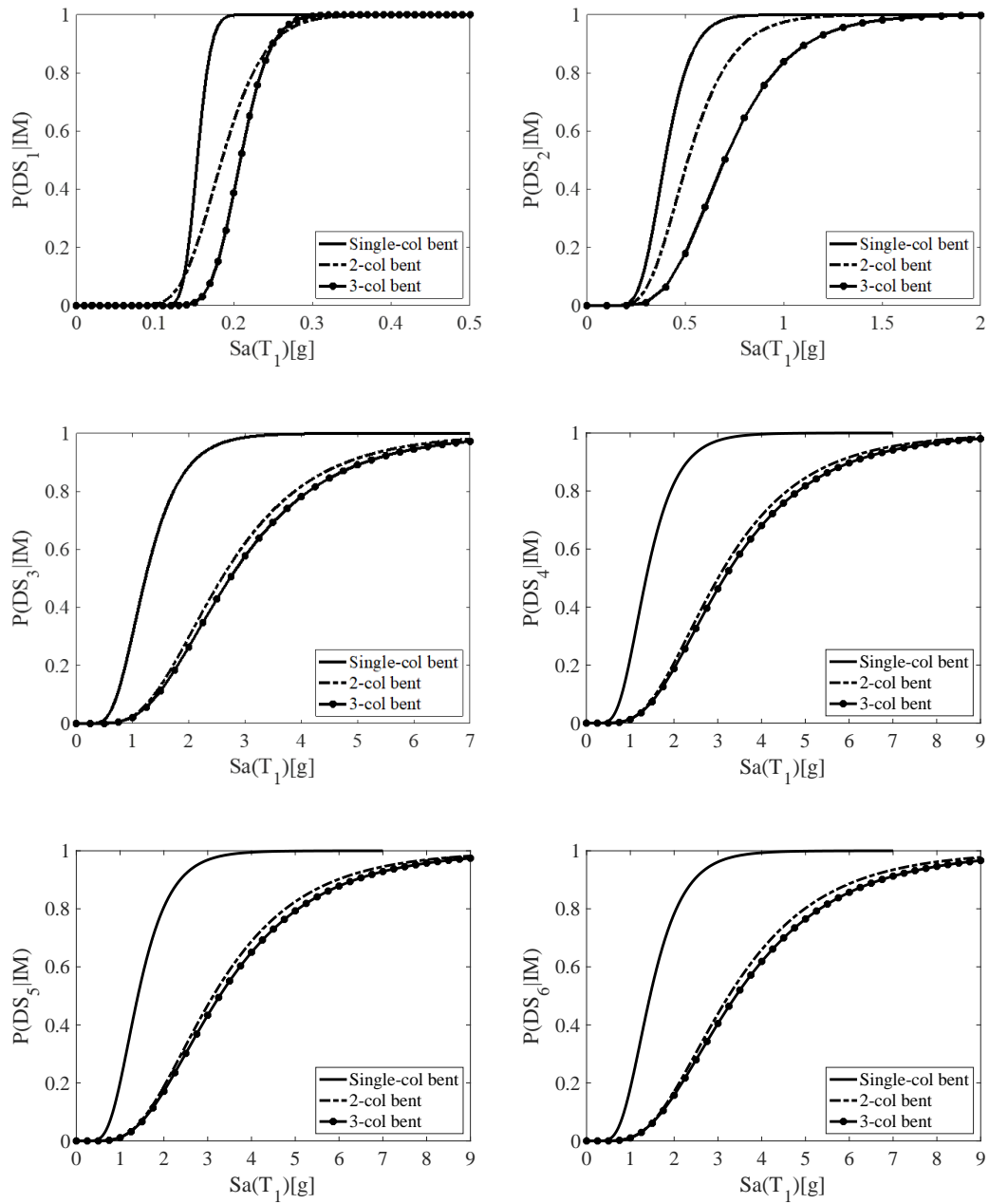
Figure 5.11 Log-normally fitted fragility function for damage states DS-1 to DS-6
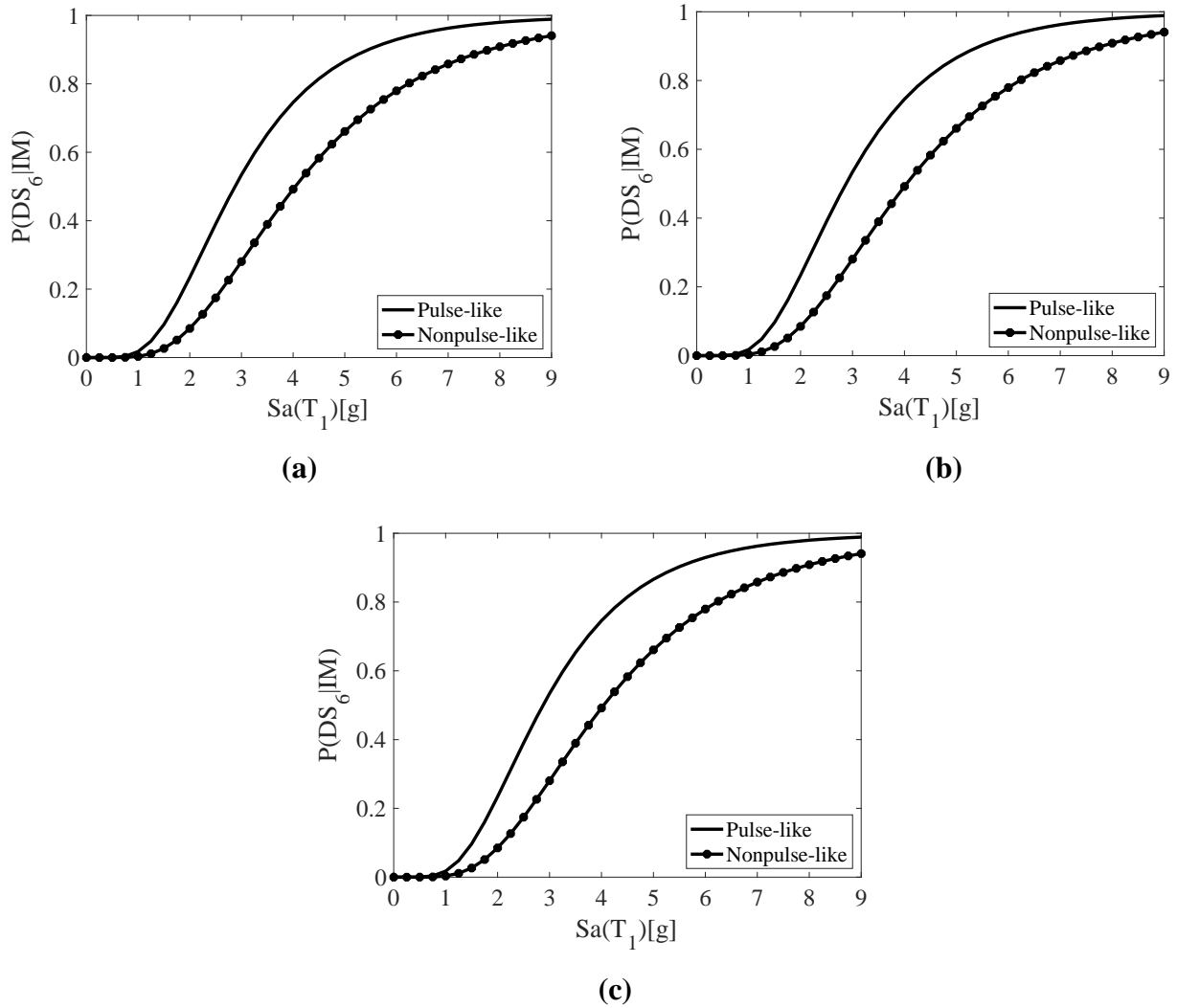
Figure 5.12 Fragility functions for damage state DS-6:
(a) single-column bent (b) 2-column bent (c) 3-column bent

The effect of pulse-like motions is also viewed from a different perspective as shown in Figure 5.13. Fragilities are examined as a function of bent type. Only a single damage state (DS-6) is presented but similar findings are valid for the remaining damage states as well. Once again, it is evident that the median intensity for the selected damage is similar for both 2-column and 3-column bents but significantly lower for single-column bents – a conclusion that was confirmed earlier when examining the entire suite of ground motions.
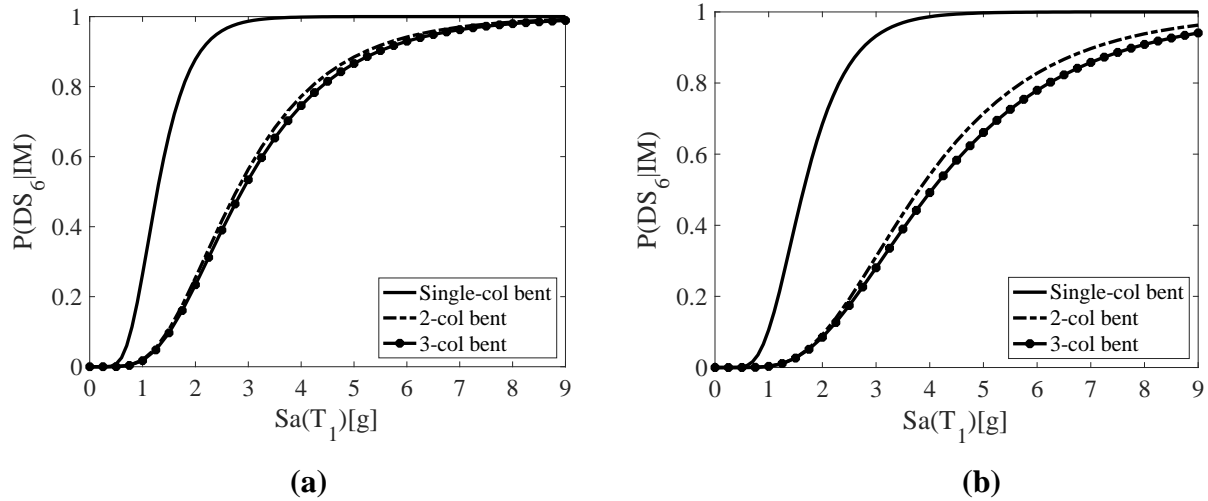
Figure 5.13 Fragility functions for damage state DS-6:
(a) pulse-like motions; (b) non-pulse motions

5.6 Non-Flexural Failure Modes

Finally, the performance of Era-1 columns that exhibit mixed failure modes are examined. Recall that in Chapter 2, a shear spring element was incorporated in the column model to represent shear deformations as well as simulate potential shear-failure of the RC bridge pier. The spring element can model both pure shear failure and mixed flexure-shear failure. If the shear capacity of the column is lower than its flexural capacity, the presence of the spring alone is adequate to capture shear failure. In the present study, the deterioration of the force-deformation response when shear failure occurs following flexural yielding is based on an empirical drift capacity model wherein the command "limitCurve Shear" in OpenSees is used to construct a shear limit curve object. As part of the validation exercises, the response of a non-ductile column that experienced shear deterioration following flexural yielding was simulated and compared with the response recorded during an experiment. Shear deterioration was initiated at a ductility of 2.0. In this final phase of the study, the response of such non-ductile columns

with mixed failure modes is examined. Shear deterioration, based on the model discussed in Section 2.3, was incorporated and the numerical simulations repeated using the FEMA P-695 ground motions. The resulting fragility functions are presented in Figure 5.14 for two damage states (DS-3 and Ds-6). As expected, the seismic intensity required to impose a given damage state is much lower for columns that exhibit mixed failure modes. The purpose here is to demonstrate the effectiveness of the proposed damage-based definition of limit states to be applied to bridge columns irrespective of failure mode.
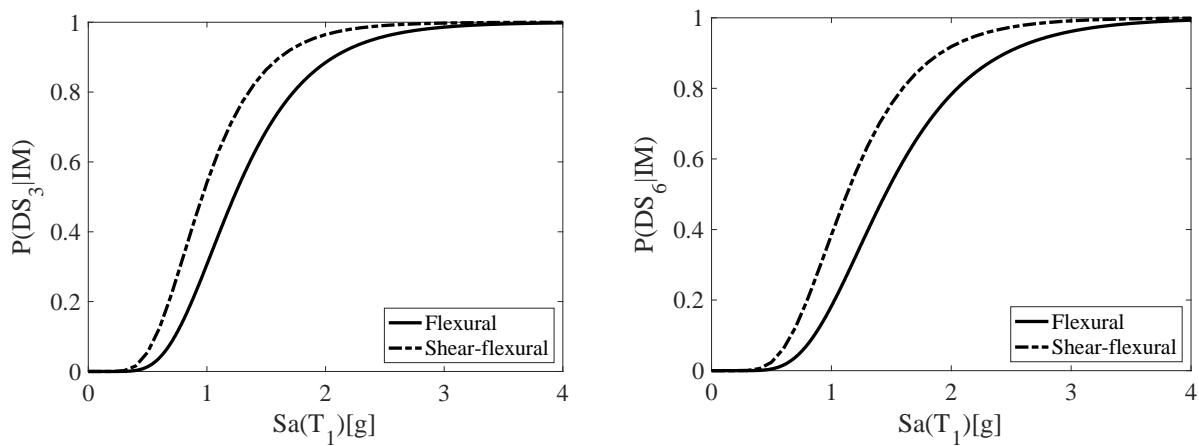
Figure 5.14 Comparing fragility functions for different failure modes

5.7   Summary

The simulations presented in this chapter should be viewed as an application of the damage-based limit states to performance assessment of bridge columns following an earthquake event. The development of fragility functions that express the probability of attaining a specific capacity limit state (or damage state) as a function of some ground motion intensity measure is an effective tool to assess seismic vulnerability of structures. The seismic assessment process is applied to bridge bents with a single column, 2 columns and 3 columns. All bridge bents had

similar lateral strengths to facilitate the performance comparison. The ground motions used in the simulations were taken from recommended records in FEMA P-695 for use in sites in California. Primary findings can be summarized as follows:

- The generated IDA curves indicate that there is a significant transition in the damage index following bar buckling. This implies that damage states beyond spalling can occur within a limited range of increase in seismic demand. A large amplitude in the response can cause a column to experience multiple damage states in the same half-cycle. The maximum damage corresponding to the peak amplitude is usually captured adequately in a ductility-base definition of limit states.

- The accumulation of damage beyond the peak displacement amplitude, resulting from low-cycle fatigue and deterioration in lateral load resisting capacity, is better estimated using a damage-based formulation as demonstrated in Chapter 4 and further validated in this chapter.

- The redundancy offered by two-column bents compared to single-column bents provides significant benefits in terms of the higher seismic intensity required to induce the same damage state. However, the benefits of redundancy did not increase with the change from a 2-column bent to a 3-column bent.

- A limited study on bridge columns experiencing a combined flexural-shear failure confirms the ability of the damage-based methodology to be used in post-earthquake seismic assessment of bridges that exhibit mixed failure modes.

CHAPTER 6.0   CONCLUSION

The main focus of the research presented in this dissertation was to develop a methodology to predict the state of damage to highway bridges in the vicinity of a seismic event. In particular, the study also addressed a gap in the current ability of Shakecast, a software platform used by the California Department of Transportation (Caltrans), to predict such damage to non-ductile bridge columns. The ability to estimate with reasonable accuracy the likelihood and extent of damage to bridges following an earthquake is crucial to post-earthquake activities such as the mobilization of emergency response. Whereas modern bridges designed after 1990 are expected to perform well, older bridges, particularly those built before 1971 (and referred to as Era-1 bridges in this report), are vulnerable to damage. Gaining knowledge about the likely damage state for a known seismic intensity will not only assist in post-earthquake efforts but also in prioritizing strengthening of such bridges.

As indicated in Chapter 1, a recent Caltrans effort (through a sponsored project carried out at Georgia Tech and Rice University) resulted in the development of a significant database of experimental tests on columns. The columns were categorized by eras (pre-1971, 1972 – 1990 and post-1990) and failure modes and damage limit states were extracted based on a uniform definition of ductility. However, only about half of the Era-1 columns can be classified as bridge columns when considering the applied axial loads on the columns during testing. Hence, in the present study, a hypothetical set of bridge columns comprising both circular and wide rectangular sections (with sectional details similar to Era-1 non-ductile columns) were generated to expand the database and damage limit states were examined through modeling and simulation.

Prior to carrying out the numerical simulations, the effectiveness of the modeling scheme used to represent a typical non-ductile column was validated through comparison of the

111

generated force-deformation responses with available experimental observations. The validation also included consideration of failure modes (flexure and mixed flexure-shear), the ability to predict bar buckling and the identification of significant spalling following crushing in the core. In the first phase of the study, ductility was used as the demand measure and a strain-based approach was used to correlate damage states with ductility. It was demonstrated that ductility was an ineffective demand measure when dealing with the randomness of earthquake loading. Consequently, the focus shifted towards the development of an alternate approach wherein the concept of a damage index was used to classify limit states. The proposed approach was validated with observed experimental responses and then applied to single-column bents subjected to both cyclic and earthquake loading. Finally, fragility functions were developed wherein exceedance probabilities of damage states are examined as a function of seismic intensity. The assessment is extended to multi-column bents is to investigate the benefits of redundancy in limiting the damage experienced by non-ductile bridge columns.

6.1 Summary of Findings

The primary findings from the study are highlighted below:

1. A force-based beam column element was used to model the bridge columns. Nonlinear behavior was represented using fiber-based discretizations of the cross-section. Of the three options considered in modeling a bridge column, it was established that a single force-based beam column element with four Gauss-Lobatto integration points resulted in the best match with a non-local formulation.

2. The overall modeling approach encompassing both element and material modeling was shown to be effective in capturing both flexural and mixed shear-flexure failure modes through comparison with experiments reported in the literature.

3. The strain-based calibration of damage limit states is an effective approach in the context of numerical simulations using a fiber-based discretization of the column element. In a fiber-based model, utilizing material strains in the core, cover concrete and reinforcing steel provide a more rational means to assess the state of damage in the cross-section which can then be correlated with global response measures such as drift and ductility.

4. When comparing numerically simulated ductility demands with estimates based on experimental data, it was found that the difference was larger for lower damage states than for extreme damage states. Yet, the median ductility demand even for the lower damage states generally differed by less than 10% though the dispersion in experimental observations reported in the literature was much higher given the fact that experiments involve unintended variations in the concrete properties, casting methods, positions of bars, variations associated with the measurement systems, etc.

5. Based on the results of the numerical simulations of both circular and wide rectangular sections, it was found that the ductility attained at damage states DS-1 through DS-5 is similar for all three loading protocols (1, 2 or 3 cycles per amplitude) though the dispersion increases at higher damage states. However, at damage states DS-6 and DS-7, the ductility limits drop when more cycles are applied at each displacement level. Hence a loading protocol based on 3 cycles per amplitude will impose more severe damage at higher damage states though the difference is less obvious at lower damage states.

6. A ductility-based limit-state definition become unreliable when applied to earthquake loading. As demonstrated in the example in Section 3.8, low-cycle fatigue and cyclic degradation can continue even if the peak ductility has already been attained. Material limit states such as bar buckling and fracture is influenced by load history and peak ductility becomes an inadequate measure to predict extreme limit states.

7. The previous finding suggests that a more advanced methodology is needed to capture all capacity limit states when the column is subjected to non-symmetric loading. Consequently, a damage-based approach is proposed in this dissertation to establishing capacity limit states for more reliable application in post-earthquake damage assessment.

8. The effectiveness of the damage-based limit states was demonstrated for both circular and wide-section columns irrespective of loading, i.e. cyclic or seismic. The damage indices for each damage state, with the exception of the collapse state, is nearly identical for all seven circular columns and all five wide rectangular section columns indicating that the proposed damage index-based approach to defining capacity limit states overcomes the drawbacks of a ductility-based measure.

9. In general, the new damage-based methodology was successful in predicting the different capacity limit states, including cracking of the cover concrete, spalling of concrete, bar buckling, crushing of the core concrete and multi-bar rupture.

It should be noted at the outset that the study is limited to ordinary highway bridges and long span bridges and bridges with anti-seismic devices such as isolators are not considered in the study. Special bridges need to be investigated on a case by case basis rather than be classified into groups.

114

6.2   Future Work

The current study focused on Era-1 columns composed of circular and wide rectangular cross-sections. While these two types of sections comprise a significant majority of Era-1 columns, there are numerous other cross-sections that need to be investigated. Some sample sections constructed pre-1971 are shown in Figure 6.1. While some of these cross-sections can be reduced to a variation of circular or rectangular shapes, it is important to carry out simulations of additional cross-sections that may exhibit increased vulnerability to seismic events.
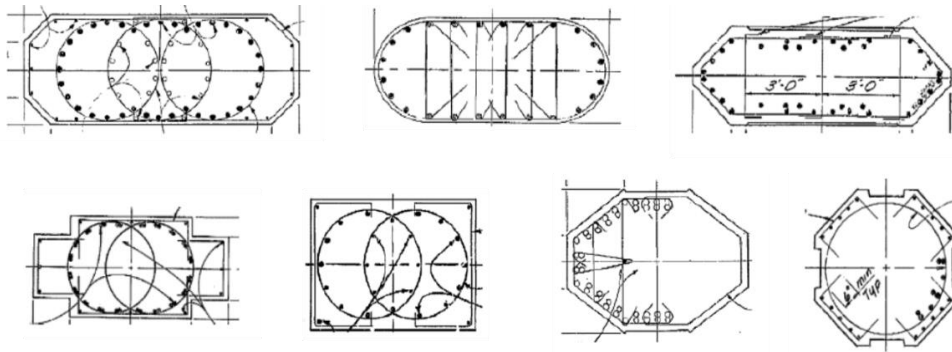
Figure 6.1. Other cross-sections used in Era-1 bridge columns

The failure modes considered in this study was mostly flexural. A limited study of shear-flexure failure modes was also investigated. It is vital to extend the study to a larger range of cross-sections experiencing either pure shear or mixed failure modes. The base component model used in the present study can accommodate these failure modes but were not fully explored.

Another aspect of the study that was somewhat lacking was the development of the damage model for early damage states such as cover cracking and initial spalling. While these damage states are less important than higher limit states, additional effort should be devoted to considerations of tensile cracking in the cover and core as well as conditions that precipitate spalling of the cover concrete.

One of the assumptions in the present study is that damage is typically limited to the bridge piers and does not extend to other components. While modern seismic design requires the deck and foundation to remain undamaged, it is not certain if pre-1971 design meets this criterion. Hence examining damage to other components of the bridge system also needs to be investigated.

REFERENCES

1. AASHTO (2017). Bridge Design Specifications. American Association of State Highway and Transportation Officials, Washington D.C.

2. Bertero, V. V. (1980). "Strength and deformation capacities of buildings under extreme environments." *Structural engineering and structural mechanics*, A Volume Honoring Edgar P. Popov, K. Pister, ed., Prentice-Hall, Englewood Cliffs, N.J., 188–237

3. Brown, J., & Kunnath, S. K. (2004). "Low-cycle fatigue behavior of reinforcing steel bars." *ACI Materials Journal*, 101(6), 457–466.

4. Chai, Y. H., M. N. Priestley and F. Seible (1991). "Seismic retrofit of circular bridge columns for enhanced flexural performance." *ACI Structural Journal* 88(5).

5. Chung, Y.S., Meyer, C. and Shinozuka, M., (1987), "Seismic Damage Assessment of RC concrete bridge columns." *J Earthquake Eng*, 18(5), 714–34.

6. Coffin, L. F. Jr. (1971). "A note on low cycle fatigue laws", *Journal of Materials*, 6, 388–402.

7. Coffin, L. F. Jr., (1954), "A Study of the Effects of Cyclic Thermal Stresses on a Ductile Metal", Transactions of the American Society of Mechanical Engineers, New York, N. Y., 76, 931-950.

8. CSA (2013). CAN/CSA-S6-14, Canadian Highway Bridge Design Code. CSA International, Ontario, Canada.

9. DiPasquale, E., and A. S. Cakmak (1988). Detection and assessment of seismic structural damage. NCEER Report 87-0015, Multidisciplinary Center for Earthquake Engineering Research, State Univ. of New York at Buffalo, NY.

10. Elwood KJ, Moehle JP (2003). Shake table tests and analytical studies on the gravity load collapse of reinforced concrete frames. Pacific Earthquake Engineering Research Center. University of California, Berkeley, California, PEER Report 2003/01.

11. FEMA. (2009). Recommended methodology for quantification of building system performance and response parameters. FEMA P695A, Prepared by the Applied Technology Council, Redwood, CA.

12. Feng Y, Kowalsky MJ, Nau JM. (2014). "Fiber-based modeling of circular reinforced Structures", NCEER Report 87-0022, State University of New York at Buffalo, New York.

13. Goodnight, J. C., Kowalsky, M. J., and Nau, J. M., (2013). "Effect of load history on performance limit states of circular bridge columns." *J. Bridge Eng*. 18, 1383–1396.

14. Goodnight, J. C., Kowalsky, M. J., Nau, J. M. (2016). "Strain Limit States for Circular RC Bridge Columns." *Earthquake Spectra*.32(3), 1627–1652.

15. Gulkan, P., and Sozen, M. (1974). "Inelastic response of reinforced concrete structures to earthquake motions." *ACI J.,* 71(12), 604 – 610.

16. Heo, Y., & Kunnath, S. K. (2013). "Damage-based seismic performance evaluation of reinforced concrete frames." *International Journal of Concrete Structures and Materials*, 7(3), 175-182

17. Ibarra L, Krawinkler H (2011)." Variance of collapse capacity of SDOF systems under earthquake excitations." *Earthquake Engineering and Structural Dynamics*, 40: 1299-1314

18. Iervolino I, Maddaloni, G and Cosenza E (2008). "Eurocode 8 Compliant Real Record Sets for Seismic Analysis of Structures." *J of Earthquake Engineering*, 12 (1), 54-90.

19. Jacobsen, L. S. (1930). "Steady forced vibrations as influenced by damping." *ASME Trans*., 52(1), 169–181.

20. Kashani M.M, Lowes L.N, Crewe A.J and Alexander, N.A (2016). "Nonlinear fiber element modelling of RC bridge piers considering inelastic buckling of reinforcement." *Engineering Structures*, 116, 163 – 177.

21. Kenawy, M., Kunnath, S., Kolwankar, S., and Kanvinde, A. (2018). "Fiber-Based Nonlocal Formulation for Simulating Softening in Reinforced Concrete Beam-Columns." *Journal of Structural Engineering*, 144(12), 04018217.

22. Kim, J. H., Kim, I.-H., & Lee, J. H. (2021). "Experimental Study on the Behavior of Existing Reinforced Concrete Multi-Column Piers under Earthquake Loading." *Applied Sciences*, 11(6), 2652.

23. Kowalsky MJ. (2000). "Deformation limit states for circular reinforced concrete bridge columns." *J Struct Eng*, 126(8),869–78.

24. Kratzig, W.B. and Meskouris, M., (1987), "Nonlinear Seismic Analysis of Reinforced Concrete Frames", *Earthquake Prognostics (Vogel and Brandes, editors), Verlag Friedr, Vieweg and Sohn, Braunschweig*, 453-462.

25. Kunnath, S.K., El-Bahy, A., Taylor, A. and Stone, W. (1997). Cumulative Seismic Damage of Reinforced Concrete Bridge Piers. NCEER Report 97-0006, Multidisciplinary Center for Earthquake Engineering Research, State Univ. of New York at Buffalo, NY.

26. Luco, N and Cornell, CA (2007). "Structure-Specific Scalar Intensity Measures for Near-Source and Ordinary Earthquake Ground Motions." *Earthquake Spectra*, 23 (2), 357 – 392.

27. Mackie, K., and Stojadinovic, B. (2005). Fragility Basis for California Highway Overpass Bridge Seismic Decision Making, PEER Report 2005/02, Pacific Earthquake Engineering Research Center, University of California, Berkeley, CA.

28. Mander, J. B., Panthaki, F. D., and Kasalanati, A., (1994), "Low Cycle Fatigue Behavior of Reinforcing Steel", *Journal of Materials in Civil Engineering*, ASCE, Vol. 6, No. 4.

29. Mander J, and Cheng C-T. (1995). Renewable hinge detailing for bridge columns. Proceedings of Pacific conference on earthquake engineering, Vol. 187, Melbourne, Australia; 197–206.

30. Mander, J. B., Priestley, M. J. N., & Park, R. (1984). Seismic design of bridge piers. Research Report 84-2, Department of Civil Engineering, University of Canterbury.

31. Manson, S. S. (1953). Behavior of materials under conditions of thermal stress. In Heat Transfer Symposium (pp. 9–75) Ann Arbor, MI: University of Michigan Engineering Research Institute.

32. Miner, M.A., (1945), "Cumulative Damage in Fatigue", *Journal of Applied Mechanics*, Vol.12, A-159.

33. Pang, Y., Cai, L., Ouyang, H., & Zhou, X. (2019). "Seismic performance assessment of different fibers reinforced concrete columns using incremental dynamic analysis." *Construction and Building Materials*, 203, 241–257

34. Park, Y.J. and Ang, A.H-S., (1985), "Mechanistic Seismic Damage Model for Reinforced Concrete", *Journal of Structural Engineering*, ASCE, 111, 722-739.

35. Park, R. (1989). "Evaluation of ductility of structures and structural assemblages from laboratory testing." *Bulletin of the New Zealand national society for earthquake engineering* 22 (3): 155-166.

36. Powell, G. and Allahabadi, R., (1988), "Seismic Damage Prediction by Deterministic Methods: Concepts and Procedures", *Earthquake Engineering and Structural Dynamics*, Vol.16.

37. Priestley, M. J. N., Seible, F., and Calvi, G. M. (1996). "Seismic design and retrofit of bridge structures", Wiley, New York.

38. Ranf, R. T., J. M. Nelson, Z. Price, M. O. Eberhard and J. F. Stanton (2006). Damage accumulation in lightly confined reinforced concrete bridge columns, Pacific Earthquake Engineering Research Center.

39. Saatcioglu, M., and Razvi, S. R. (1992). "Strength and ductility of con- fined concrete." *J. Struct. Diy., ASCE*, 118(6), 1590-1607.

40. Schoettler, M. J., J. I. Restrepo, G. Guerrini, D. Duck, and F. Carrea. 2015. A full-scale, single-column bridge bent tested by shake-table excitation. PEER Rep. 2015/02. Berkeley, CA: Pacific Earthquake Engineering Research Center, Univ. of California.

41. Sheikh, M. N., & Légeron, F. (2014). "Performance based seismic assessment of bridges designed according to Canadian Highway Bridge Design Code." *Canadian Journal of Civil Engineering*, 41(9), 777–787.

42. Shibata, A., and Sozen, M. (1976). "Substitute structure method for seis- mic design in R/C." *J. Struct. Div., ASCE*, 102(1), 1–18

43. Shome N and Cornell.CA. (1999). Probabilistic seismic demand analysis of nonlinear structures. RMS-35. RMS Program, Stanford, CA, 320

44. Shome, N, Cornell, CA, Bazzurro, P and Carballo, JE (1998). "Earthquakes, records, and nonlinear responses." *Earthquake Spectra* 14, 469–500.

45. Soesianawati, M.T.; Park, R; and Priestley, M.J.N. (1986). Limited Ductility Design of Reinforced Concrete Columns, Report 86-10, Department of Civil Engineering, University of Canterbury, Christchurch, New Zealand, 208 pages.

46. Su, J., Dhakal, R. P., & Junjie Wang. (2017). "Fiber-based damage analysis of reinforced concrete bridge piers." *Soil Dynamics and Earthquake Engineering*, *96*, 13–34.

47. Sun Z., Seible, F. and Priestley, M.J.N. (1993), Diagnostics and retrofit of rectangular bridge columns for seismic loads. Structural Systems Research Program, 93/07, University of California, San Diego, La Jolla, July

48. Vamvatisikos, D. and Cornell, C.A. (2002). "Incremental dynamic analysis." *Earthquake Engineering & Structural Dynamics*. **31**: 491–514.

49. Vosooghi, A. and Saiidi, M. (2012). "Experimental Fragility Curves for Seismic Response of Reinforced Concrete Bridge Columns," *ACI Structural Journal*, V. 109, No. 6, November-December, 825-834.

50. Williams, M.S., and Sexsmith, R.G. (1994), Review of Methods Assessing Seismic Damage in Concrete Structures, Technical Report 94-02, Earthquake Engineering Research Facility, University of British Columbia, Canada.

51. Yassin, M.H.M. (1994). Nonlinear analysis of prestressed concrete structures under monotonic and cycling loads, PhD dissertation, University of California, Berkeley.

52. Yoon, Y.H., Ataya, S., Mahan, M., Malek, A., Saiidi, M.S. and Zokaie, T. (2019). Probabilistic Damage Control Application: Implementation of Performance-Based Earthquake Engineering in Seismic Design of Highway Bridge Columns. *Journal of Bridge Engineering*, 24(7): 04019068.

53. Zhao, J., and S. Sritharan. (2007) "Modeling of strain penetration effects in fiber-based analysis of reinforced concrete structures." *ACI Structural Journal*, 104(2),133-141.

54. Zong, Z., Kunnath, S., and Monti, G. (2014). "Material Model Incorporating Buckling of Reinforcing Bars in RC Columns." *Journal of Structural Engineering*, 140(1), 04013032.